Modelling of the Achilles and Patella tendon forces during treadmill running

by

Cailin Maria Rice

Thesis presented in partial fulfilment of the requirements for the degree of Master of Engineering (Mechatronic) in the Faculty of Engineering at Stellenbosch University

Supervisor: Prof. G. Venter

Co-supervisor: Dr. S. J. Cockcroft

March 2021

Stellenbosch University https://scholar.sun.ac.za

Declaration

By submitting this thesis electronically, I declare that the entirety of the work contained therein is my own, original work, that I am the sole author thereof (save to the extent explicitly otherwise stated), that reproduction and publication thereof by Stellenbosch University will not infringe any third party rights and that I have not previously in its entirety or in part submitted it for obtaining any qualification.

Date: 20 November 2020

Signature: .....

Copyright © 2021 Stellenbosch University
All rights reserved.

Stellenbosch University https://scholar.sun.ac.za

Abstract

Tendons are dense connective tissue bands which attach muscle to bone, and facilitate the movement of the musculoskeletal system during locomotion. Although tendon loading during running is one of several biomechanical factors that have been linked to economical running gait and performance (Moore, 2012; Moore *et al.*, 2014; Moore, 2016), it has not been widely researched. Traditionally, *in-vivo* measurement techniques are used to quantify dynamic tendon loads; however, these experimental procedures are expensive and high-risk. *In-silico* gait analysis workflows and musculoskeletal modelling platforms allow researchers to non-invasively investigate the relationship between body motion and internal biomechanical loads during locomotion (Wilke and Galbusera, 2018). The following study is a continuation of a previous Masters project (Groeneveld, 2020), and aimed to develop and investigate an open-source, subject non-specific *in-silico* method which may be used to estimate the dynamic loading profiles of the Achilles and patella tendons during treadmill running. The robustness and reliability of the developed *in-silico* method was also examined. It is important to note that the raw experimental data sets used throughout this study were captured during the previous study (Groeneveld, 2020).

The developed *in-silico* method comprises of pre-existing (Hamner *et al.*, 2010) and modified OpenSim musculoskeletal models, as well as a fully automated gait analysis pipeline. In addition to the generic implementations of the Achilles and patella tendons (Hamner *et al.*, 2010), a modified variation of the Achilles tendon, and three modified variations of the patella tendon, were adapted from literature (Arnold *et al.*, 2010; Schmitz and Piovesan, 2016; Rajagopal *et al.*, 2016; Lai *et al.*, 2017) and investigated. Two-sample t-tests (Pataky, 2012) were used to examine the robustness of the modified models (with respect to the modifications realized within them) and found that the implemented modifications did not significantly impact model accuracy.

The processing pipeline was programmed in Python and utilized the OpenSim-Python API feed to implement a generic running gait analysis workflow. The analysis workflow comprised of five processes, namely: Scaling, Inverse Kinematics, Residual Reduction Algorithm, Computed Muscle Control, and Muscle Analysis. Additionally, the pipeline incorporated a novel pre-analysis data processing functionality and post-analysis results processing method. The study utilized the *in-silico* method to investigate 5 participants, running on 3 gradient-variant surfaces, namely: level (0°), incline (9°), and decline (-9°) surfaces. To investigate the reliability of the resulting *in-silico* tendon loads, a comparison between the normalized trends observed in the *in-silico* and corresponding *in-vivo* tendon loads (Groeneveld, 2020), was realized. Notably, the modified tendon implementations out-performed the original variations (Hamner *et al.*, 2010).

The study concluded that subject non-specific modelling and gait analysis techniques may be used to achieve reasonable estimations of the dynamic loading profiles of the

Stellenbosch University https://scholar.sun.ac.za

Achilles tendon during level, incline, and decline running conditions. Realizing reasonable approximations for the patella tendon proved to be challenging, as the developed method did not account for subject-specific quadriceps muscle activity during locomotion. Additionally, the study concluded that the resulting *in-silico* method is best suited for level running gait analyses.

Stellenbosch University https://scholar.sun.ac.za

Opsomming

Senings is digte bindweefselbande wat spiere aan die been heg en die beweging van die spier-skelet-stelsel tydens beweging fasiliteer. Alhoewel sening-kragte tydens die hardloop-aksie een van verskeie biomeganiese faktore is wat gekoppel is aan optimale gang ("gait" of manier van loop/hardloop) en prestasie vir hardloop (Moore, 2012; Moore *et al.*, 2014; Moore, 2016), is daar nog nie baie navorsing daaroor gedoen nie. Tradisioneel word *in-vivo* metingstegnieke gebruik om dinamiese tendonbelastings te kwantifiseer. Hierdie eksperimentele prosedures is egter duur en gaan met 'n hoë risiko gepaard. *In-silico* gang-analise werkstrome en spier-skelet-stelsel modelleringsplatforms stel navorsers in staat om nie-indringend die verband tussen liggaamsbeweging en interne biomeganiese kragte tydens beweging te ondersoek (Wilke and Galbusera, 2018). Dié studie is 'n voortsetting van 'n vorige meestersprojek (Groeneveld, 2020), en het ten doel gehad om 'n oop-bron, nie-spesifieke *in-silico*-metode te ontwikkel wat gebruik kan word om die dinamiese ladingsprofiele van die Achilles- en patella-senings tydens 'n hardloop-aktiwiteit op 'n trapmeul te ondersoek. Die stabiliteit en betroubaarheid van die ontwikkelde *in-silico*-metode is ook ondersoek. Dit is belangrik om daarop te let dat die rou eksperimentele datastelle wat gedurende hierdie studie gebruik is, tydens die vorige studie vasgelé is (Groeneveld, 2020).

Die ontwikkelde in-silico-metode sluit bestaande (Hamner *et al.*, 2010) en gemodifiseerde OpenSim spier-skelet-stelsel modelle in, asook 'n volledig outomatiese gang-ontledingspyplyn vir analise van gang. Bykomend tot die generiese implementering van die Achilles- en patella-senings (Hamner *et al.*, 2010), is 'n gemodifiseerde variasie van die Achilles-sening en drie gemodifiseerde variasies van die patella-sening uit die literatuur aangepas (Arnold *et al.*, 2010; Schmitz and Piovesan, 2016; Rajagopal *et al.*, 2016; Lai *et al.*, 2017) en ondersoek. Dubbel-monster t-toetse (Pataky, 2012) is gebruik om die stabiliteit van die gemodifiseerde modelle te ondersoek (m.b.t. die veranderinge wat binne hulle aangebring is) en bevind dat die geïmplementeerde veranderinge nie 'n beduidende impak op die model se akkuraatheid het nie.

Die verwerkingspyplyn is in Python geprogrammeer en gebruik die OpenSim-Python API-vloei om 'n generiese hardloop-gang analise te implementeer. Die pyplyn bestaan uit vyf prosesse, nl.: skalering, omgekeerde kinematika, residuele reduksie algoritme, berekende spierbeheer en spieranalise. Ook het die pyplyn 'n nuwe pre-analise- en post-analise resultaat-verwerkings-funksionaliteit geïnkorporeer. Die studie het die in-silico-metode gebruik om 5 deelnemers te bestudeer, wat op 3 verskillende gradiënt-oppervlaktes op die trapmeul gehardloop het, nl.: plat (0°), helling (9°) en afdraand (-9°). Om die betroubaarheid van die uitkomste van die *in-silico*-tendonbelastings te ondersoek, is 'n vergelyking tussen die genormaliseerde tendense waargeneem in die *in-silico*- en ooreenstemmende *in-vivo*-tendonbelastings (Groeneveld, 2020). Die gewysigde tendon-implementerings het veral die oorspronklike variasies oortref (Hamner *et al.*, 2010).

Stellenbosch University https://scholar.sun.ac.za

Dié studie het tot die gevolgtrekking gekom dat deelnemer-onspesifieke gangontledingstegnieke gebruik kan word om redelike beramings van die dinamiese ladingsprofiele van die Achilles-sening te kry tydens plat-, helling- en afdraand-toestande. Om redelike benaderings vir die patella-sening te laat realiseer was moeilik, aangesien die ontwikkelde metode nie rekening gehou het met deelnemer-spesifieke dyspier-aktiwiteit tydens beweging nie. Die studie het ook tot die gevolgtrekking gekom dat die uiteindelike *in-silico*-metode die beste geskik is vir plat gang-analises.

Stellenbosch University https://scholar.sun.ac.za

Acknowledgements

I would like to express my sincere gratitude and thanks to the following people for their contributions throughout the duration of this project:

- My supervisors, Prof. Gerhard Venter and Dr. John Cockcroft, for their guidance and supervision over the past two years. The insight and knowledge I have gained from you both is invaluable.
- Dr. Cobus Müller, for your valuable insight and the extra time you've spent on the project.
- Llewellyn Groeneveld, for your prior research contributions and assistance during the beginning stages of the project.
- My parents, for your support and the opportunity to pursue this degree.
- My fiancé, Matthew, for your continual support everyday, and for making each day brighter. Special thanks for proof reading the entire thesis.

Stellenbosch University https://scholar.sun.ac.za

Contents

Declaration i

Abstract ii

Opsomming iv

Acknowledgements vi

Nomenclature xviii

1 Introduction 1
- 1.1 Project Background . . . 1
- 1.2 Project Motivation . . . 2
- 1.3 Project Aim and Objectives . . . 3
- 1.4 Project Scope . . . 4

2 Literature Review 6
- 2.1 The Biomechanics of Running . . . 6
  - 2.1.1 The Running Gait Cycle . . . 6
  - 2.1.2 Running Gait Analysis . . . 7
  - 2.1.3 Treadmill Running . . . 9
  - 2.1.4 Potential and Kinetic Energy . . . 9
- 2.2 Connective Tissue: Tendons . . . 9
  - 2.2.1 Background . . . 9
  - 2.2.2 Achilles Tendon . . . 12
  - 2.2.3 Patella Tendon . . . 14
  - 2.2.4 Tendons as Springs . . . 15
- 2.3 Previous Work . . . 17
  - 2.3.1 Optic Fibre Sensor . . . 17
  - 2.3.2 Participant Selection . . . 17
  - 2.3.3 Instrumentation and Facilities . . . 18
  - 2.3.4 Experimental Protocol . . . 19
  - 2.3.5 Results . . . 19
- 2.4 OpenSim . . . 20
  - 2.4.1 Background . . . 20
  - 2.4.2 Gait Analysis Workflow . . . 20
  - 2.4.3 OpenSim API . . . 27
- 2.5 Statistical Methods . . . 28
  - 2.5.1 Statistical Parametric Mapping . . . 29
  - 2.5.2 Regression Analysis . . . 31

Stellenbosch University https://scholar.sun.ac.za

3 Model Development **33**
3.1 The OpenSim Model . . . 33
3.1.1 Joint Geometry . . . 34
3.1.2 Muscle Geometry . . . 34
3.1.3 Limitations of the Model . . . 36
3.2 Model Modifications . . . 37
3.2.1 Patella Bone . . . 37
3.2.2 Patellofemoral Joint . . . 38
3.2.3 Tibiofemoral Joint . . . 38
3.2.4 Quadriceps Muscles Wrapping Surfaces . . . 39
3.2.5 Patella Tendon . . . 40
3.2.6 Achilles Tendon . . . 44
3.3 Developed Models . . . 45

4 Python Processing Pipeline **46**
4.1 Pipeline Objectives . . . 46
4.2 Pipeline Workflow . . . 46
4.2.1 User Input Management . . . 47
4.2.2 Data Processing . . . 48
4.2.3 Model Selection . . . 52
4.2.4 OpenSim Gait Analysis . . . 52
4.2.5 Result Processing . . . 59

5 Results **61**
5.1 OpenSim Results . . . 61
5.1.1 Scaling . . . 61
5.1.2 Inverse Kinematics . . . 62
5.1.3 Residual Reduction Analysis . . . 65
5.1.4 Computed Muscle Control . . . 66
5.1.5 Kinematics Comparison . . . 68
5.2 Model Sensitivity Analysis . . . 69
5.2.1 Patella Tendon . . . 69
5.2.2 Achilles Tendon . . . 72
5.3 Independent Trend Analysis . . . 73
5.3.1 Patella Tendon . . . 74
5.3.2 Achilles Tendon . . . 76

6 Discussion **79**
6.1 Processing Pipeline . . . 79
6.1.1 OpenSim Workflow Performance . . . 79
6.1.2 Computational Performance . . . 80
6.2 Patella Tendon Modelling . . . 81
6.3 Achilles Tendon Modelling . . . 83
6.4 Problems and Pitfalls . . . 84

7 Conclusion **85**

Stellenbosch University https://scholar.sun.ac.za

A OpenSim Models: Supplementary Information **86**
A.1 Hamner *et al.* (2010) Musculoskeletal Model 86
A.2 Modified Musculoskeletal Models 90

B Processing Pipeline: Supplementary Information **93**
B.1 Folder Structure Requirements 93
B.2 Residual Analysis Signal Filtering Technique 96
B.3 Process Flowcharts 96
B.4 Sample Output Figures 98

C OpenSim Results **101**
C.1 Inverse Kinematics 101
C.2 Residual Reduction Analysis 102
C.3 Computed Muscle Control 104
C.4 Kinematics Comparison 106
C.5 Tendon Force Profiles 108

D Model Sensitivity Analysis **112**
D.1 Patella Tendon 112
D.2 Achilles Tendon 114

E Independent Trend Analysis **117**
E.1 Patella Tendon 117
E.2 Achilles Tendon 119

List of References **121**

Stellenbosch University https://scholar.sun.ac.za

List of Figures

2.1 Running Gait Cycle (Kintec, 2016*a*) 6
2.2 Foot placement techniques observed during running (Coh, 2012). 8
2.3 A typical vertical GRF profile observed during the stance phase of the running gait cycle, adapted from Coh (2012). 8
2.4 The anatomical reference planes and directions of the human body, adapted from Novo (2011) 10
2.5 The hierarchal structure of a tendon, adapted from Britannica (2019) 11
2.6 The stress-strain curve of a tendon, adapted from Robi *et al.* (2013) 11
2.7 The anatomy of the Achilles tendon, adapted from Healthwise (2018) 12
2.8 Illustration of the neutral position of the foot and ankle (flat), as well as the dorsal flexion (tilted-upwards) and plantar flexion (titled-downwards) of the foot (de Pina Filho and Dultra, 2013) 13
2.9 Anterior view of the anatomy of the patella tendon (Pope, 2018) 14
2.10 The four principle movements of the knee joint, namely: extension and flexion, as well as lateral and medial rotation (Islam, 2018) 15
2.11 Load-Elongation curve for a tendon structure during the observation of stretching and recoil of the tendon when applied to a simple tension load (Robi *et al.*, 2013). The shaded area illustrates the energy loss (hysteresis) during the process of loading and unloading 16
2.12 Modified Hill-type muscle-tendon model(Yu and Wilson, 2014) 16
2.13 Overall instrumentation and setup of the participant (Groeneveld, 2020) . . 18
2.14 Overview of the a generic OpenSim workflow utilized in this study 21
2.15 Example of a coordinate transformation in the OpenSim GUI, where the experimental motion capture data (markers illustrated in blue) undergoes a 270° rotation about the X axis, and a 180° rotation about the Z axis. The OpenSim coordinate system is given by the red (X), yellow (Y), and green (Z) orthogonal frame at the base of the musculoskeletal model. Adapted from Galloy *et al.* (2018) 22
2.16 Schematic of the Computed Muscle Control (CMC) algorithm (Thelen and Anderson, 2006) 26
2.17 OpenSim framework and architecture (Seth *et al.*, 2011; Delp *et al.*, 2007) . 27

Stellenbosch University https://scholar.sun.ac.za

2.18 An example output plot of the **spm1d** toolbox's two-sample t-test. The example analyses differences in a subject's plantar arch angle during normal (black) and fast (red) walking (Caravaggi *et al.*, 2010). The first subplot (left) illustrates the mean and standard deviation clouds of the two datasets being analysed. The second subplot (right) illustrates the results of the SPM analysis, where the grey, shaded region indicates a region (cluster) of statistical significance (i.e. where the two datasets are statistically different), and its corresponding p-value ($p = 0.029$). Additionally, the second subplot indicates the statistical significance level ($\alpha = 0.05$) and critical threshold ($t^* = 2.930$) values. Adapted from Pataky (2019) 31
2.19 Example of a regression analysis plot. The example analyses differences in a subject's plantar arch angle during normal (black) and fast (red) walking (Caravaggi *et al.*, 2010). The first subplot (left) illustrates the mean and standard deviation clouds of the two datasets being analysed. The second subplot (right) illustrates the results of the regression analysis, where the grey dashed line indicates the regression equation, y, and the black dots represent the superimposed walking conditions. For this example, R^2 is calculated as 0.99, indicating that 99 % of the variation observed in the subject's plantar arch angle during fast walking can be explained by the regression model. 32

3.1 Anterior (left) and posterior (right) views of the three-dimensional "Full Body Running" model (Hamner *et al.*, 2010) 33
3.2 Representation of the gluteus maximus in the "Full Body Running" model. Three muscle-tendon units are used to define the entire muscle 35
3.3 The Hill-type muscle-tendon model presented by Thelen (2003) 35
3.4 Illustration of the "Full Body Running" model's quadriceps muscle paths at 0° (**A**) and 120° (**B**) knee flexion angle, respectively (Hamner *et al.*, 2010) . 37
3.5 Graph illustrating the translation and rotation of the patella, expressed in the femur's coordinate system, during different angles of knee flexion. Note that the black points illustrate the location of the patella's coordinate frame origin. Y is positive in the superior direction (green), X in the anterior direction (red), and Z out of the page (blue). Full knee extension (0°) is indicated at **A**, and maximum knee flexion (120°) at **B** 38
3.6 Illustration of the use of a cylindrical wrapping surface (i.e. the aqua cylinder pictured in **B**) at the distal end of the femur in the developed models. To prevent muscle-bone penetration, unrealistic muscle paths and large muscle forces (observed in **A**), the rectus femoris, vastus lateralis, vastus medialis, and vastus intermedius muscle fibres are programmed to wrap over the cylindrical surface at all angles of knee flexion (**B**). The figure illustrates surface wrapping capabilities at 120° knee flexion 40
3.7 The single ligament fibre implementation of the patella tendon (green fibre). The quadriceps muscle fibres (red fibres), in particular the rectus femoris, vastus lateralis, vastus medialis, and vastus intermedius muscle fibres, connect the femur to the superior area of the patella 40

Stellenbosch University https://scholar.sun.ac.za

3.8 The narrow implicit implementation of the patella tendon via the wrapping of the quadriceps muscles over the patella. The quadriceps muscle fibres (red fibres) connect the hip and femur to the superior area of the patella, as in the single ligament fibre implementation. From the superior insertion points, the muscles extend and attach to the distal pole of the patella, and connect the patella to the tibial tuberosity via the a single active fibre path 42
3.9 The broad implicit implementation of the patella tendon via the wrapping of the quadriceps muscles over the patella (Rajagopal *et al.*, 2016). The quadriceps muscle fibres (red fibres) connect the hip and femur to the superior area of the patella, as in the single ligament fibre implementation. From the superior insertion points, the muscles extend and attach to the distal area of the patella, and finally connect the patella to the tibial tuberosity via three muscle fibre paths 43
3.10 Illustration of the half-cylindrical wrapping surface used for the Achilles tendon variation. The wrapping surface, indicated in aqua, is located at the head/superior end of the tibia, and the respective muscle fibres (soleus, medial and lateral gastrocnemius fibres) are indicated in red 44

4.1 High-level overview of the developed Python processing pipeline 47
4.2 High-level workflow of the implemented data processing algorithm 48
4.3 Flowchart of the implemented signal processing workflow for the processing of motion capture data in the developed pipeline 49
4.4 The implemented signal processing workflow for processing EMG signals . 51
4.5 Flowchart of the implemented signal processing workflow for processing EMG data signals in the developed Python processing pipeline 51
4.6 Flowchart of the OpenSim analysis workflow implemented in the developed Python processing pipeline 52
4.7 Flowchart of the implemented results processing workflow 60

5.1 Hamner *et al.* (2010) model IK results for level running conditions 62
5.2 Hamner *et al.* (2010) model IK results for incline running conditions 63
5.3 Hamner *et al.* (2010) model IK results for decline running conditions 63
5.4 Comparison of Participant 2's resultant hip, knee, and ankle joint kinematics from IK (black), RRA (red), and CMC (blue), for the Hamner *et al.* (2010) model during level (top), incline (middle), and decline (bottom) running conditions 68
5.5 Two-sample t-test results of the *in-silico* patella tendon profiles for Participant 2 during level running conditions 70
5.6 Two-sample t-test results of the *in-silico* patella tendon profiles for Participant 2 during incline running conditions 70
5.7 Two-sample t-test results of the *in-silico* patella tendon profiles for Participant 2 during decline running conditions 71
5.8 Two-sample t-test results of the *in-silico* Achilles tendon profiles for Participant 2 during level running conditions 72
5.9 Two-sample t-test results of the *in-silico* Achilles tendon profiles for Participant 2 during incline running conditions 72

Stellenbosch University https://scholar.sun.ac.za

5.10 Two-sample t-test results of the *in-silico* Achilles tendon profiles for Participant 2 during decline running conditions 73
5.11 Trend comparison between the *in-vivo* and estimated patella tendon loading profiles observed during level running conditions 74
5.12 Trend comparison between the *in-vivo* and estimated patella tendon loading profiles observed during incline running conditions. Notably, Participant 1 and 4 only have results for the Hamner *et al.* (2010) model 74
5.13 Trend comparison between the *in-vivo* and estimated patella tendon loading profiles observed during decline running conditions. Notably, Participant 5 only has results for the Hamner *et al.* (2010) model 75
5.14 Trend comparison between the *in-vivo* and *in-silico* Achilles tendon loading profiles observed during level, incline, and decline running conditions for Participant 2 77

A.1 Front view of marker placement (Groeneveld, 2020; Vicon, 2019) 89
A.2 Back view of marker placement (Groeneveld, 2020; Vicon, 2019) 89
A.3 Moment arm validation plot of the implemented patella tendon single ligament fibre model documented in Chapter 3. The ligament (red) fibre's moment arm is compared to the moment arm of the patella tendon fibre realized in the Arnold *et al.* (2010) model (black dashed) during different angles of knee flexion 90
A.4 Graph illustrating the derived normalized force-length curve of the patella tendon, Equation 3.8 (Thelen, 2003). The dashed grey line separates the toe region (left of the dashed line) and the linear-elastic region (right of the dashed line) of the tendon. The black dot highlights the normalized length at which one norm of the tendon force is realized - i.e. F_0^M is reached . . . 91
A.5 Investigation of the normalized ligament fibre length in relation to knee flexion angle. The left subplot illustrates the normalized ligament fibre length curve observed during the full knee flexion range realized in the modified models (0° - 120°). The right subplot illustrates the normalized ligament fibre length observed during the running gait cycle. The normalized length of the ligament fibre (red), as well as the normalized fibre length threshold (dashed yellow) are illustrated in both figures 92

B.1 Folder structure requirements for the developed processing pipeline 93
B.2 Folder format for the OpensSim musculoskeletal model folder 93
B.3 Folder structure requirements for each subject's experimental data folder . . 94
B.4 Folder structure requirements for the OpensSim workflow setup files 94
B.5 Internal folder structure for the developed processing pipeline scripts 95
B.6 Results folder structure generated by the processing pipeline 95
B.7 Illustration of the theory behind the Winter (2009) residual analysis used for filtering marker trajectories. The plot shows the residual signal between a filtered and unfiltered signal as a function of the filter cut-off frequency (f_c). The optimal cut-off frequency ($f_c^{'}$) is defined as the frequency at which the intersection of horizontal line (0 gradient line from the Y axis intersection of the line *ad*) and the residual signal occurs (Winter, 2009) 96

Stellenbosch University https://scholar.sun.ac.za

B.8 Input-output flowchart of the OpenSim Scaling process implemented in the developed Python processing pipeline . . . 97
B.9 Input-output flowchart of the OpenSim IK process implemented in the developed Python processing pipeline . . . 97
B.10 Input-output flowchart of the OpenSim RRA process implemented in the developed Python processing pipeline . . . 97
B.11 Input-output flowchart of the Muscle Analysis process implemented in the developed Python processing pipeline. Due to the fact that the MA Tool is run in conjunction with the CMC Tool, the MA setup file is fed into the CMC setup file, in Figure B.12 . . . 97
B.12 Input-output flowchart of the OpenSim CMC process implemented in the developed Python processing pipeline . . . 98
B.13 Example plot of the IK (grey) and RRA (blue) kinematics results . . . 98
B.14 Example plot of the RRA (grey) and CMC (blue) kinematics results . . . 99
B.15 Example plot of the RRA (grey) and CMC (blue) joint moment results . . . 99
B.16 Example plot of the muscle activation signal results. The experimental EMG (grey) and CMC (blue) muscle activation signals are compared in an effort to identify if the CMC process has yielded reliable results which match those experienced in reality . . . 100
B.17 Example plot of the Achilles and patella tendon force results . . . 100

D.1 Plot legend for the patella tendon mean and SD clouds illustrated in Appendix D . . . 112
D.2 Two-sample t-test results of the *in-silico* patella tendon profiles for Participant 1 during level running conditions . . . 112
D.3 Two-sample t-test results of the *in-silico* patella tendon profiles for Participant 3 during level running conditions . . . 113
D.4 Two-sample t-test results of the *in-silico* patella tendon profiles for Participant 5 during level running conditions . . . 113
D.5 Two-sample t-test results of the *in-silico* patella tendon profiles for Participant 3 during decline running conditions . . . 114
D.6 Plot legend for the Achilles tendon mean and SD clouds illustrated in Appendix D . . . 114
D.7 Two-sample t-test results of the *in-silico* Achilles tendon profiles for Participant 1 during level running conditions . . . 115
D.8 Two-sample t-test results of the *in-silico* Achilles tendon profiles for Participant 3 during level running conditions . . . 115
D.9 Two-sample t-test results of the *in-silico* Achilles tendon profiles for Participant 5 during level running conditions . . . 116
D.10 Two-sample t-test results of the *in-silico* Achilles tendon profiles for Participant 3 during decline running conditions . . . 116

E.1 Trend comparison between the *in-vivo* (black) and estimated patella tendon force observed for Models 1, 2, 4, and 5 during level running conditions . . . 117

Stellenbosch University https://scholar.sun.ac.za

E.2 Trend comparison between the *in-vivo* and estimated patella tendon force observed for Models 1, 2, 4, and 5 during incline running conditions. Notably, Participant 2 is the only participant with results for the presented modified models 117
E.3 Trend comparison between the *in-vivo* and estimated patella tendon force observed for Models 1, 2, 4, and 5 during decline running conditions. Notably, Participant 2 and 3 are the only participants with results for the presented modified models 118
E.4 Trend comparison between the *in-vivo* and estimated Achilles tendon force observed for Models 1, 2, 4, and 5 during level, incline, and decline running conditions 119

Stellenbosch University https://scholar.sun.ac.za

List of Tables

2.1 Summary of the selected participants biological data (Groeneveld, 2020) . . 17
2.2 Summary of the experimental instrumentation and tools used during testing (Groeneveld, 2020) 18

3.1 Overview of the developed musculoskeletal models and the modified variations of the patella and Achilles tendons realized in them 45

4.1 Scaling marker pairs used to scaled the musculoskeletal model's rigid body segments 54
4.2 The recommended error threshold values used to evaluate RRA results for full-body simulations of walking and running, as provided by OpenSim (Simtk-confluence.stanford.edu, 2020) 56
4.3 The recommended error threshold values used to evaluate CMC results for full-body simulations of walking and running, as provided by OpenSim (Simtk-confluence.stanford.edu, 2020) 58

5.1 Musculoskeletal model scaling errors calculated in OpenSim 61
5.2 RMS errors and mean coefficient of determination (R^2), acquired during the IK process for the Hamner *et al.* (2010) and third modified models during level, incline, and decline running conditions 64
5.3 Maximum X, Y, and Z components of the residual forces and torques observed during RRA for level running 65
5.4 The maximum X, Y, and Z component values of the residual forces and torques observed during RRA for incline running 65
5.5 The maximum X, Y, and Z component values of the residual forces and torques observed during RRA for decline running 66
5.6 The maximum X, Y, and Z component values of the residual forces and torques observed during CMC for level running 66
5.7 The maximum X, Y, and Z component values of the residual forces and torques observed during CMC for incline running 67
5.8 The maximum X, Y, and Z component values of the residual forces and torques observed during CMC for decline running 67
5.9 Coefficient of determination (R^2) observed for the estimated patella tendon forces during level, incline, and decline running 76
5.10 Coefficient of determination (R^2) observed for the estimated Achilles tendon forces during level, incline, and decline running for Participant 2 78

A.1 Inertial and mass properties of each body segment of the "Full Body Running" model (Hamner *et al.*, 2010). The tabulated data is based off of the height and weight settings of the default, unscaled version of the model . . 86

Stellenbosch University https://scholar.sun.ac.za

A.2 Musculotendon parameters of the "Full Body Running" model (Hamner *et al.*, 2010) 87
A.3 Inertial and mass properties of the patella bone geometry. The mass and inertial properties are defined according to cadaver literature (Delp, 1990; Anderson and Pandy, 1999), and are based off of the height and weight settings of the default, unscaled version of the Hamner *et al.* (2010) model . 90
A.4 Summary of the modified muscle properties of the rectus femoris, vastus lateralis, vastus medialis, and vastus intermedius muscles in the implicit patella tendon model variations, values adapted from Rajagopal *et al.* (2016) . . . 92

C.1 RMS errors and mean coefficient of determination (R^2), acquired for Models 1, 2, 4, 5, and 6 during IK for level, incline, and decline running conditions 101
C.2 Maximum X, Y, and Z components of the residual forces and torques observed for Models 1, 2, 4, 5, and 6 during RRA for level running conditions . 102
C.3 Maximum X, Y, and Z components of the residual forces and torques observed for Models 1, 2, 4, 5, and 6 during RRA for incline running conditions 103
C.4 Maximum X, Y, and Z components of the residual forces and torques observed for Models 1, 2, 4, 5, and 6 during RRA for decline running conditions 103
C.5 The maximum X, Y, and Z component values of the residual forces and torques observed for Models 1, 2, 4, 5, and 6 during CMC for level running . 104
C.6 The maximum X, Y, and Z component values of the residual forces and torques observed for Models 1, 2, 4, 5, and 6 during CMC for incline running 105
C.7 The maximum X, Y, and Z component values of the residual forces and torques observed for Models 1, 2, 4, 5, and 6 during CMC for decline running 105
C.8 Comparison of the mean coefficient of determination (R^2) for the net hip, knee, ankle joint angles, acquired during IK and RRA for level, incline, and decline running conditions 106
C.9 Comparison of the mean coefficient of determination (R^2) for the net hip, knee, ankle joint angles, acquired during RRA and CMC for level, incline, and decline running conditions 107
C.10 Normalized *in-silico* peak patella tendon forces 109
C.11 Normalized *in-silico* peak Achilles tendon forces 110

E.1 Coefficient of determination (R^2) observed for the estimated patella tendon forces of Models 1, 2, 4, and 5 during level, incline, and decline running . . 118
E.2 Coefficient of determination (R^2) observed for the estimated Achilles tendon forces of Models 1, 2, 4, and 5 during level, incline, and decline running . . 120

Stellenbosch University https://scholar.sun.ac.za

Nomenclature

Constants

$g = 9.81$	Gravitational acceleration	$[\mathrm{m/s^2}]$
$e = 2.718$	Euler's number	

Variables

α	Statistical significance level	
a	Muscle activation level	$[\%]$
b	Damping coefficient	$[\mathrm{Ns/m}]$
d	Cohen's effect size	
ϵ	Strain	$[\mathrm{mm/mm}]$
f	Knee flexion angle	$[\mathrm{degrees}]$
f_c	Cut-off frequency	$[\mathrm{Hz}]$
f_c'	Optimal cut-off frequency	$[\mathrm{Hz}]$
F	Force	$[\mathrm{N}]$
$inrot$	Internal-external knee rotation	$[\mathrm{degrees}]$
H_0	Null hypothesis	
k	Spring stiffness	$[\mathrm{N/m}]$
k_p	Position feedback control gain	
k_v	Velocity feedback control gain	
l	Length	$[\mathrm{m}]$
$\widetilde{l}$	Normalized length	$[\mathrm{m/m}]$
$\dot{l}$	Rate of change of length	$[\mathrm{m/s}]$
m	Mass	$[\mathrm{kg}]$
n	Number of body components	
N	Number of degrees of freedom	
p	Calculated probability	
$PCSA$	Physiological cross sectional area	$[\mathrm{m^2}]$
R^2	Coefficient of determination	
σ_0^M	Specific tension of mammalian tissue	$[\mathrm{N/cm^2}]$
θ_{PA}	Pennation angle	$[\mathrm{degrees}]$
t	Current time stamp	$[\mathrm{s}]$
t^*	Critical threshold value	
T	Time step/increment	$[\mathrm{s}]$
w	Marker weight	
$varus$	Varus-valgus knee rotation	$[\mathrm{degrees}]$

Stellenbosch University https://scholar.sun.ac.za

x	Anterior-posterior knee joint displacement	$[\mathrm{mm}]$
X	X axis in a Cartesian coordinate system	
y	Superior-inferior knee joint displacement	$[\mathrm{mm}]$
Y	Y axis in a Cartesian coordinate system	
z	Medial-lateral knee joint displacement	$[\mathrm{mm}]$
Z	Z axis in a Cartesian coordinate system	

Vectors and Matrices

$\boldsymbol{a}$	Body acceleration vector
$\boldsymbol{C}(\boldsymbol{q}, \dot{\boldsymbol{q}})$	Coriolis and centrifugal force vector
$\boldsymbol{F}$	Force vector
$\boldsymbol{g}$	Gravitational acceleration vector
$\boldsymbol{G}(\boldsymbol{q})$	Gravitational force vector
$\boldsymbol{M}(\boldsymbol{q})$	System mass matrix
$\boldsymbol{q}$	Generalized coordinate position vector
$\dot{\boldsymbol{q}}$	Generalized coordinate velocity vector
$\ddot{\boldsymbol{q}}$	Generalized coordinate acceleration vector
$\boldsymbol{\tau}$	Generalized force vector
$\boldsymbol{x}$	Marker position vector

Superscripts and Subscripts

0	Maximum/Optimal value
exp	Experimental value
M	Muscle
MTU	Musculotendon unit
res	Residual value
T	Tendon

Abbreviations

1D	1-dimensional
3D	3-dimensional
AJC	Ankle joint center
ASIS	Anterior iliac spine
API	Application programming interface
ANOVA	Analysis of variance
BW	Body weight
C3D	Coordinate 3D
CSV	Comma-separated file
CE	Contractile element

Stellenbosch University https://scholar.sun.ac.za

CMC	Computed Muscle Control
COD	Coefficient of determination
COM	Center of mass
COP	Center of pressure
DC	Direct current
DE	Discrete element
DOF	Degree of freedom
EMG	Electromyography
EOM	Equations of motion
FS	Foot strike
GRF	Ground reaction force
GUI	Graphical User Interface
HAT	Head and torso
HJC	Hip joint center
HREC	Health Research Ethics Committee
IK	Inverse Kinematics
ID	Inverse Dynamics
ISEK	International Society of Electrophysiology and Kinesiology
KE	Kinetic energy
KJC	Knee joint center
MA	Muscle Analysis
ML	Machine learning
MOT	Motion file
MRI	Magnetic Resonance Imaging
MTU	Musculotendon unit
NIH	National Institutes of Health
OLS	Ordinary least squares
PA	Pennation angle
PCSA	Physiological cross sectional area
PD	Proportional-derivative
PE	Potential energy
PEE	Parallel elastic element
PMD	Preserve mass distribution
PNG	Portable Network Graphics file
PSD	Power spectral density
RFT	Random Field Theory
RRA	Residual Reduction Algorithm
RMS	Root mean squared
SD	Standard deviation

Stellenbosch University https://scholar.sun.ac.za

SE	Series element
SPM	Statistical Parametric Mapping
STO	Storage file
TD	Typically developed
TRC	Trace file
TM	Target mass
TO	Toe off
TXT	Text file
WLS	Weighted least squares
XML	eXtensible Markup Language file

Stellenbosch University https://scholar.sun.ac.za

1 Introduction

1.1 Project Background

It has been argued that humans have evolved into efficient runners (Bramble and Lieberman, 2004), despite the fact the loads placed on the human musculoskeletal system during running are considerable. A study conducted by Scott and Winter (1990) indicated that peak tendon forces during running may range between 6.1 - 8.2 times body weight for the Achilles tendon and 4.7 - 6.9 times body weight for the patella tendon. This feat is even more impressive when considering that the nature of these loads changes with speed (Munro *et al.*, 1987), stride frequency (cadence) (Heiderscheit *et al.*, 2011; Lenhart *et al.*, 2014), and gradient (Gottschall and Kram, 2005; Vernillo *et al.*, 2016). As a result of the repetitive, cyclic nature of running, overuse injuries have become common amongst recreational and competitive runners (Taunton *et al.*, 2002; Malliaras *et al.*, 2015).

In recent studies, it has become evident that running economy has a strong relationship with running performance (Moore, 2016). Despite the fact that these studies have linked several biomechanical factors to economical running gait (Moore, 2012; Moore *et al.*, 2014; Moore, 2016), they have failed to identify and explain the interactions of these factors with one another. Consequently, there are many unanswered questions regarding economical running gait, particularly relating to the role of tendon loading.

Tendon loading during running is one biomechanical factor that can arguably improve one's running economy (Vernillo *et al.*, 2016), and has not been widely researched. Tendons are dense connective tissue bands that connect muscle to bone, and facilitate the movement of the musculoskeletal system during locomotion. During running, tendons are loaded predominantly through mechanical energy changes, realized from the rising and falling of the body during gait, and muscle work.

Recently, an *in-vivo* measurement technique to directly quantify the dynamic loading patterns experienced in the Achilles and patella tendons during treadmill running, was developed and investigated within the Department of Mechanical and Mechatronic Engineering at Stellenbosch University (Groeneveld, 2020). The experimental procedure involves the surgical insertion of optic fibre in the transverse direction, through the cross-section, of the desired tendon. A light intensity sensor is further used to calculate and log the dynamic tendon load experienced during locomotion (Groeneveld, 2020). Although the results of this procedure seem promising, it is a costly venture with many ethical difficulties and health risks.

In addition to *in-vivo* measurement techniques, mathematical modelling and *in-vitro* measurement techniques are commonly used to predict tendon forces in humans (Sheehan and Drace, 2000). These methods however, are susceptible to large numerical

Stellenbosch University https://scholar.sun.ac.za

errors arising from scaling and measurement errors, as well as assumptions and simplifications (Yamaguchi and Zajac, 1989; Behrmann *et al.*, 2012; Faber *et al.*, 2018). Furthermore, discrepancies between the anatomical orientation of the tendons in each individual and the alignment and attachment sites of the tendon to the respective muscles and bones, complicate tendon force modelling. As a result, *in-vivo* methods are used to validate mathematical techniques.

In-silico gait analysis workflows and musculoskeletal modelling software platforms are valuable tools in the present-day biomechanical field as they provide scientists with the ability to non-invasively investigate the relationship between body motion and internal biomechanical loads over a wide range of physiological and pathological conditions (Wilke and Galbusera, 2018). Despite the existence of numerous musculoskeletal models and gait analysis workflows that investigate and analyse human biomechanics during both high and low impact activities, to the authors knowledge an *in-silico* method dedicated to the determination of tendon loading patterns during treadmill running has not yet been developed. This is likely due to the difficulties and costs associated with performance and reliability assessments of developed workflows.

In general *in-silico* gait analysis workflows can utilize subject-specific or non-subject specific musculoskeletal modelling techniques. Unlike non-subject specific models, subject-specific models represent the subject to a high degree of accuracy and are derived using magnetic resonance imaging (MRI) scans, as well as ultra-sound scans. As a result, the *in-silico* results achieved by subject-specific models are more accurate than non-subject specific models, and provide deeper insight into the biomechanics of the subject during locomotion. Conversely, subject-specific models are resource dense, and are significantly more expensive to produce than non-subject-specific models.

Consequently, the following project is concerned with the development of a non-subject specific *in-silico* musculoskeletal modelling and gait analysis workflow, using a collection of open source software platforms, such that it may be utilized to estimate the dynamic loading profiles of the Achilles and patella tendons during treadmill running.

1.2 Project Motivation

This project is a continuation of a previous Masters project (Groeneveld, 2020). The continuation of this project is motivated by the investigation and development of a generic, open-source, *in-silico* method which may be utilized to determine the dynamic tendon loading profiles of the lower limbs during treadmill running.

The development of such an *in-silico* solution would not only significantly reduce the health/injury risks and ethical challenges faced by current *in-vivo* experimental procedures, but will also provide a cost-effective and non-invasive alternative.

Additionally, the project's resulting workflows and processes will provide a simple and easy to use framework for future related studies, where meaningful insight regarding the relationship between the tendon loading, muscle activation, running gait, performance,

Stellenbosch University https://scholar.sun.ac.za

and injury, can be investigated. This additional insight might have important implications for the improvement of current rehabilitation strategies and coaching techniques (Muller *et al.*, 2018). Furthermore, it will provide an additional tool to aid research in understanding the relationship between load magnitude and placement with running speed, cadence, and gradient.

1.3 Project Aim and Objectives

The aim of the project is to develop and investigate a non-subject specific *in-silico* modelling and gait analysis solution, using open-source software platforms, that may be utilized to predict the dynamic loading profiles of the Achilles and patella tendons during treadmill running. The *in-silico* solution will comprise of series of a pre-existing and modified musculoskeletal models, as well as a running gait analysis pipeline.

The musculoskeletal models and running analysis workflow will be designed in an open-source musculoskeletal modelling and simulation platform called OpenSim, and the processing pipeline will be established in Python. The resulting models and pipeline will provide the necessary framework in which future data can be applied and analysed, without requiring extensive user intervention.

In order to achieve the project's aim, three project objectives were identified:

1. The development of a series of modified musculoskeletal models, each derived from a generic, pre-existing musculoskeletal model.

   It is required that the models are developed in OpenSim, contain both of the desired tendons, and may be used to manually complete the project's gait analysis workflow via the OpenSim Graphical User Interface (GUI).

2. The development of a fully automated Python processing pipeline that conducts running gait analysis, for any OpenSim musculoskeletal model, and outputs the dynamic loading profiles of the desired tendons.

   The process of manually conducting gait analysis in the OpenSim GUI is both tedious and time consuming. The development of an automated processing pipeline will introduce ease of use and time efficiency.

3. Perform an analysis of the differences and similarities resulting between the generic and developed musculoskeletal model's resulting tendon load estimates and the *in-vivo* tendon load measurements.

   The analysis procedure will be conducted in two stages, namely:

   - Inter-model sensitivity evaluation:

     A statistical analysis to determine how robust the modified models are with respect to modelling assumptions and changes

Stellenbosch University https://scholar.sun.ac.za

- Independent trend analysis:
  A difference analysis to determine the reliability and validity of the *in-silico* solution, by comparing the resulting *in-silico* tendon profiles to an independent dataset, in particular the *in-vivo* tendon measurements obtained by Groeneveld (2020)

In order for the developed *in-silico* solution to be critically analysed, it is required that the datasets used throughout this study should introduce diversity and variety, and therefore represent a range of different subjects and running conditions. For this reason, the developed *in-silico* method will be utilized to conduct analyses for five different subjects, and three different running conditions: level (0°), incline (9°), and decline (-9°) running conditions.

1.4 Project Scope

The *in-silico* solution developed during this project is strictly limited to the development of a series of modified musculoskeletal models, from a selected pre-existing model, and an automated running analysis pipeline. In order for the pipeline to execute running gait analysis, it is required that the pipeline utilizes the Python-OpenSim API Interface. For this project the software versions used in the pipeline include Python 3.7 and OpenSim 4.1. Furthermore, it is important to note that the project focuses intently on treadmill running gait, and examines only the Achilles and patella tendons.

The experimental datasets captured during the preceding project have been made available for use during this project (Groeneveld, 2020). Consequently, the experimental process of capturing the necessary datasets falls outside the scope of this project. It is important to note that ethical approval for the utilization of the data captured by Groeneveld (2020) was secured for the duration of the project. The shared datasets comprise of non-invasive motion capture and electromyography (EMG) datasets, as well as invasive *in-vivo* tendon load measurements for the Achilles and patella tendons. These datasets were captured for five participants, running subject to varying intrinsic and extrinsic factors, in particular: increased (110 %) and decreased (90 %) cadence, as well as level (0°), incline (9°), and decline (-9°) running conditions.

Consequently, the developed workflow will utilize the previously captured non-invasive experimental datasets to estimate the tendon loading profiles. Furthermore, the *in-vivo* load measurements captured by Groeneveld (2020) will be utilized as an independent dataset, against which validation and performance testing of the *in-silico* solution can be realized.

Lastly, the analysis of the reliability and sensitivity of both the estimated tendon loading profiles and the developed models, lies within the scope of this project. As previously mentioned, the project will incorporate datasets that represent a range of running conditions, specifically focusing on the variation of gradient. This is necessary to investigate the versatility of the developed solution, and ultimately investigate the effects of these varying datasets on the estimated tendon loading profiles.

Stellenbosch University https://scholar.sun.ac.za

It is important to note that further research is needed to understand the relation between tendon loading to both performance and injury, and lies outside the scope of this project.

Stellenbosch University https://scholar.sun.ac.za

2 Literature Review

The following chapter documents the background information which is crucial to the execution and understanding of the project. The chapter will broadly discuss the biomechanics of running, connective tissue, the anatomy and physiology of the Achilles and patella tendons, previous work relating to the study, OpenSim, and finally, the statistical methods to be used.

2.1 The Biomechanics of Running

Biomechanics is defined as the study of the mechanical laws relating to the movement or structure of living organisms (Phillips, 2013). The following section will discuss the biomechanics of running with emphasis on the running gait cycle and analysis, treadmill running, and the role of potential and kinetic energy.

2.1.1 The Running Gait Cycle

The gait cycle is the basic unit of measurement in gait analysis (Morris, 1977). The gait cycle begins when one foot comes into contact with the ground, and ends when that same foot makes contact with the ground again.

The running gait cycle can be decomposed into three phases, namely the: stance phase, swing phase, and float phase. Traditionally, the stance phase is examined during injury and performance analysis, as during this phase, the foot and leg bear the body weight. The swing phase and float phase are classified as “passive movement” phases as their execution and outcome are the product of the work done during the stance phase (Phillips, 2013). Figure 2.1 illustrates the phases and components of the running gait cycle.

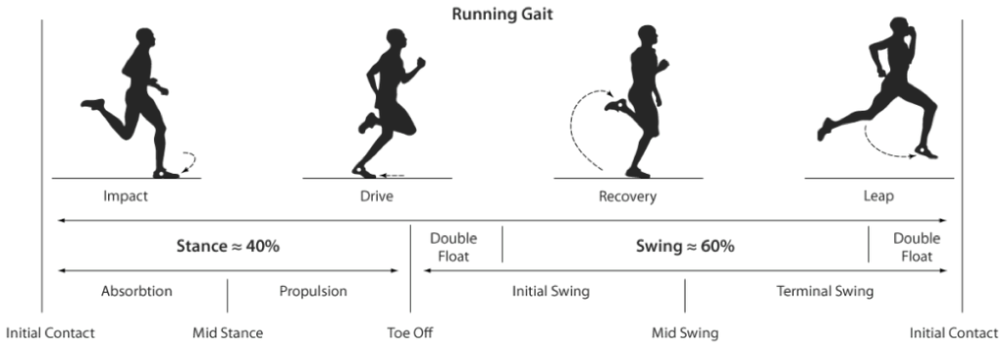

Figure 2.1: Running Gait Cycle (Kintec, 2016*a*)

Stellenbosch University https://scholar.sun.ac.za

The stance phase is defined as the period in which the foot remains in contact with the ground, and accounts for approximately 40 % of the running gait cycle. In normal gait, the stance phase can be divided into two sub-phases: initial contact to mid-stance (associated with force absorption), and mid-stance to toe-off (associated with propulsion) (Sheila *et al.*, 2005).

The swing phase is defined as the period in which the foot does not make contact with the ground, and accounts for the remaining 60 % of the running gait cycle. Similar to the stance phase, the swing phase can be divided into three sub-phases, namely: initial swing, mid-swing and terminal swing.

Initial swing, also referred to as “follow-through”, occurs immediately after toe-off (TO), and ends at the final point of posterior movement of the foot (Kintec, 2016*b*). Mid-swing occurs half way through the swing phase, and represents the period of time at which the foot undergoes anterior movement. Terminal swing takes place while the foot descends to the ground.

The float phase is defined as the period during which both feet are off the ground. The float phase occurs twice during the running gait cycle: at the beginning of initial swing, and at the end of terminal swing - this is illustrated in Figure 2.1 as “Double Float”.

2.1.2 Running Gait Analysis

Running gait analysis can be conducted in numerous ways - from being conducted along a continuum using real-time gait observations, to the use of high-level technology (i.e. high-definition motion capture systems, force plates, computer systems, and other laboratory measurement devices) (Sheila *et al.*, 2005). Traditionally, gait kinematic analysis is conducted in steady-state (i.e. analysis is conducted during continuous running - no starting and stopping included) and requires sufficient space for the subject to start, walk, run, and stop (D‘Amico, 2002).

Running economy is typically defined as the energy demand for the given velocity of sub-maximal running (Saunders *et al.*, 2004), and is an important physiological parameter as it predicts running performance (Anderson, 1996; Daniels, 1985). It is quantified by measuring the steady-state consumption of oxygen (VO_2) and the respiratory exchange rate (Saunders *et al.*, 2004).

Running kinematics is the study of body segments and joint motion independent of the forces responsible for causing the motion (Novacheck, 1998). Position, velocity, acceleration, and joint angles are considered during running kinematics. Common practice involves the assumption of body segments as rigid bodies, and joints as the connection between two body segments. The angle between two body segments, on either side of a joint, is known as the joint angle. Kinematic variables are often analysed as a function of time, relative to the running gait cycle, and in terms of the three anatomical planes (see Figure 2.4).

Stellenbosch University https://scholar.sun.ac.za

Running velocity is dependent on both the stride frequency (cadence) and stride length of an individual's gait (Groeneveld, 2020). Dugan and Bhat (2005) found that with an increasing running speed, the length of the stance phase decreases, whilst the length of the swing phase increases. Studies have shown that although an increased running velocity produces a higher forward momentum and decreased shifting of center of mass (Mann and Hagy, 1980), it exerts significantly higher strains on the lower leg's tendons and results in greater energy expenditure (Lichtwark and Wilson, 2006) - yielding decreased running efficiency and running economy.

Figure 2.2 highlights three foot placement techniques commonly observed during running. Heel strike is observed during lower velocity running, whereas mid-foot and forefoot strike are commonly observed during high velocity running.

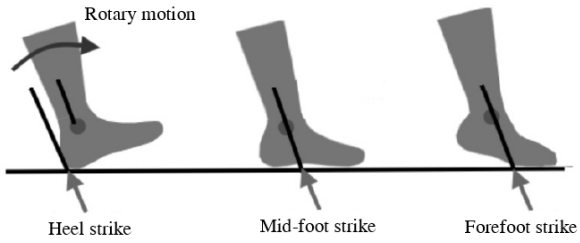

Figure 2.2: Foot placement techniques observed during running (Coh, 2012).

Running kinetics is the study of the movement and the forces responsible for producing it (Esquenazi, 2002). Ground reaction forces, muscle contraction and relaxation forces, and joint moments (calculated using ground reaction forces and kinematics, also known as inverse dynamics) are considered during running kinetics. Typically, the magnitude of the ground reaction force (GRF) experienced by an individual is approximately 2 - 3 times their body weight (Novacheck, 1998; Coh, 2012). Figure 2.3 illustrates a typical vertical GRF profile observed during the stance phase of the running gait cycle (Coh, 2012).

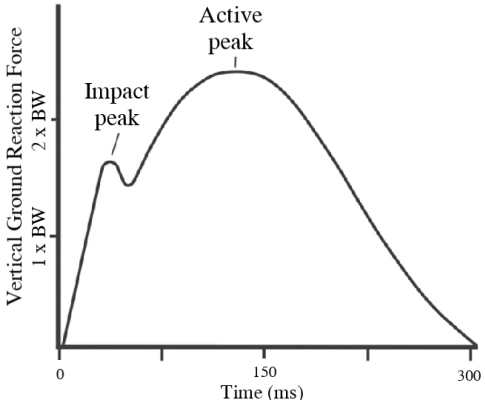

Figure 2.3: A typical vertical GRF profile observed during the stance phase of the running gait cycle, adapted from Coh (2012).

Stellenbosch University https://scholar.sun.ac.za

The first peak illustrated in Figure 2.3 is known as the impact peak, and is caused by foot strike (FS). The second peak is known as the active peak, and is the force generated by the leg as the leg's plantar-flexor muscles contract in order to propel the leg forward during the stance phase (Bigoutte *et al.*, 2016). The active peak further represents the maximum load experienced during the foot's contact period with the ground.

2.1.3 Treadmill Running

Research from Nelson *et al.* (1972), Riley *et al.* (2007), and Monte (1976) show that there is a reasonable difference between over-ground running biomechanics and treadmill running biomechanics. According to their research, treadmill running yields longer stance phases, lower ground reaction forces, higher stride frequencies, shorter stride lengths, and decreased shifting of center of mass than that experienced during over-ground running. Although these studies indicate that treadmill running biomechanics differ to that of over-ground running biomechanics, Riley *et al.* (2007) concluded that they are statistically similar.

Despite the above mentioned pit-falls of treadmill running, the use of treadmills for running gait analysis is advantageous as it provides the necessary space for the subject to start, walk, run, and stop, as well as enables continuous monitoring and observation of the running gait cycle. Furthermore, the use of a treadmill allows for fine control over running speed and surface gradient, as well as forces the subject to adapt to a more secure gait profile (Sheila *et al.*, 2005).

2.1.4 Potential and Kinetic Energy

The relationship between kinetic energy (KE) and potential energy (PE) during running differs to that during walking. During walking, KE and PE are out-of-phase, during running however, KE and PE are in-phase (Novacheck, 1998). It is suggested that during running, energy efficiency is achieved and maintained through the storage and return of elastic potential energy through the stretch of elastic structures (such as tendons), and transfer of energy from one body segment to another through joints and joint muscles (Novacheck, 1998; Vaughan, 1984).

2.2 Connective Tissue: Tendons

2.2.1 Background

The human body is a complex, highly organized structure that consists of unique cells that work together to perform specific functions necessary for sustaining life (Villa-Forte, 2019). Figure 2.4 illustrates the anatomical reference planes and directions of the human body.

Stellenbosch University https://scholar.sun.ac.za

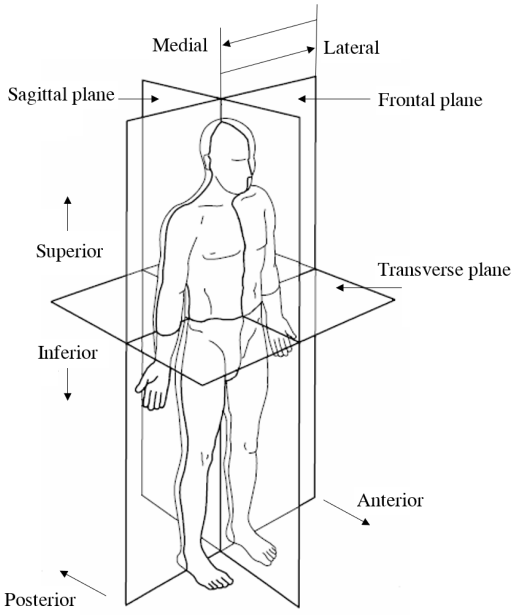

Figure 2.4: The anatomical reference planes and directions of the human body, adapted from Novo (2011)

Movement is one of the eight necessary functions of life, and involves the skeletal system, skeletal muscle, and connective tissue (Marieb and Keller, 2018). The skeletal system is composed of bones, cartilage, and joints. It performs many vital functions, such as: support, facilitating movement, protection of internal organs, storing of important fats and minerals, and the production of blood cells (OpenStax, 2013).

Skeletal muscles are voluntary muscles that consist of large muscle fibres, and are attached to the skeletal system via dense connective tissue cords, called tendons. The primary function of skeletal muscle is to contract or relax, and hence induce movement of the body. Other functions include maintaining posture and body position, as well as the stabilization of joints.

Skeletal muscle contraction is stimulated via a series of nerve impulses that innovate the skeletal muscle's fibres. The contraction force of a muscle is translated from the muscle's contracted sarcomere(s) (the basic functional unit(s) of skeletal muscle), through the tendon, and onto bone, thus resulting in movement of that bone. Together, skeletal muscle and their respective tendons make up the musculotendinous units of the body.

There are four categories of connective tissue, namely: dense connective tissue (tendons and ligaments), loose connective tissue (fats), fluid connective tissue (blood) and supporting connective tissue (bones and cartilage) (Marieb and Keller, 2018). Tendons and ligaments are classified as dense connective tissue, and are the connective tissue that exist between muscle and bone, or two bones, respectively. Research shows that tendons and ligaments are highly similar in both mechanical and structural properties (Marieb and Keller, 2018). For this reason, and the purpose of simplification, all liga-

Stellenbosch University https://scholar.sun.ac.za

ments will be referred to as tendons throughout the remainder of the document.

Tendons are made up of a matrix of collagen fibres, that are tightly packed and aligned in the same direction as that of the applied force experienced by the tendon. Figure 2.5 illustrates the hierarchal structure of a tendon.

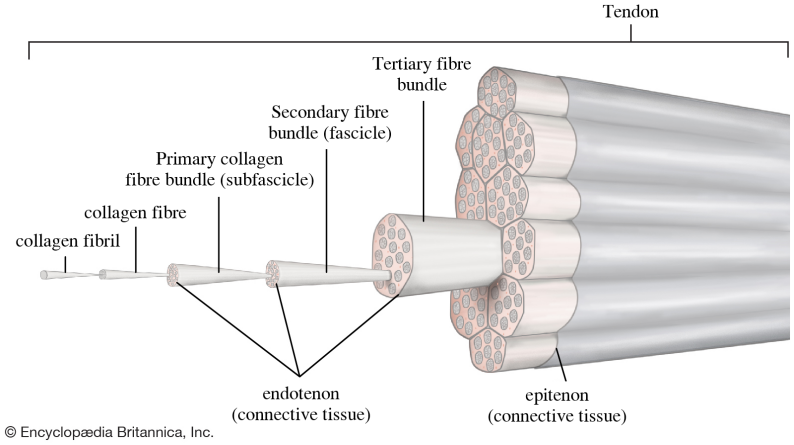

Figure 2.5: The hierarchal structure of a tendon, adapted from Britannica (2019)

Tendons are characterised by their strength and cushioning attributes, enabling them to be both stiff and flexible - allowing them to store and return energy during movement (Alexander, 1991). Figure 2.6 illustrates the stress strain curve for tendons.

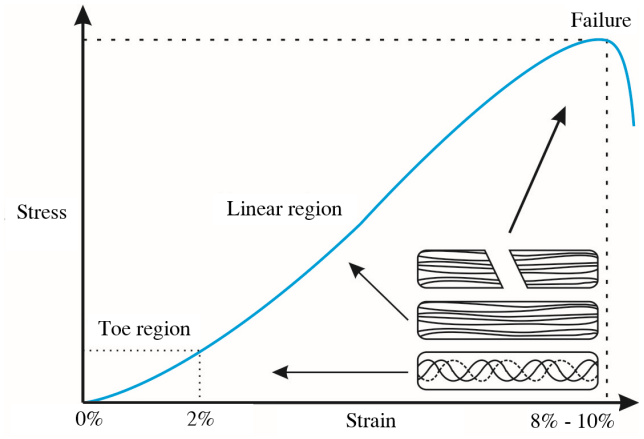

Figure 2.6: The stress-strain curve of a tendon, adapted from Robi *et al.* (2013)

With reference to Figure 2.6, at 0 % strain, a characteristic inherent to unloaded tendons, known as crimp, is present. Crimp refers to the zig-zag formation of collagen fibrils as a result of the contraction of the same collagen fibrils when at rest. As strain increases, the tendon enters the non-linear toe region (between 0 - 2 % strain) and the contracted collagen fibrils straighten. Once the strain surpasses the 2 % strain threshold, the tendon enters the linear elastic region. The yield region for a tendon is

Stellenbosch University https://scholar.sun.ac.za

approximated as 8 - 10 % strain (Robi *et al.*, 2013). Once the tendon experiences strain levels that lie within the yield region, the collagen fibrils begin to slip and fail. According to Noyes *et al.* (1984), everyday activity occurs within the non-linear toe region.

Additionally, tendons have viscoelastic properties (Wang *et al.*, 2012) - i.e. the mechanical properties of a tendon are directly affected by the strain rate applied to that tendon (Robi *et al.*, 2013). Properties associated with viscoelastic materials include: hysteresis, creep, and stress relaxation (Robi *et al.*, 2013). Wang *et al.* (2012) investigated and documented the effects of high and low strain rates on a tendon's mechanical properties. It was found that higher strain rates increased the stiffness of the tendons, resulting in an increased ability to transmit large forces, and lower strain rates increased the tendon's ability to store energy, resulting in a decreased ability of the tendon to effectively transmit forces.

2.2.2 Achilles Tendon

Anatomy

The Achilles tendon, also known as the calcaneal tendon, is the thickest and strongest tendon in the human body. Its anatomical function is to connect two muscle groups of the posterior leg, namely the gastrocnemius (calf) and soleus muscles, to bone - specifically the calcaneal tuberosity on the calcaneus (the heel bone) (Doral *et al.*, 2010). Collectively the gastrocnemius and soleus muscle groups are referred to as the triceps surae. Figure 2.7 illustrates the orientation of the Achilles tendon, in relation to the triceps surae and the calcaneus.

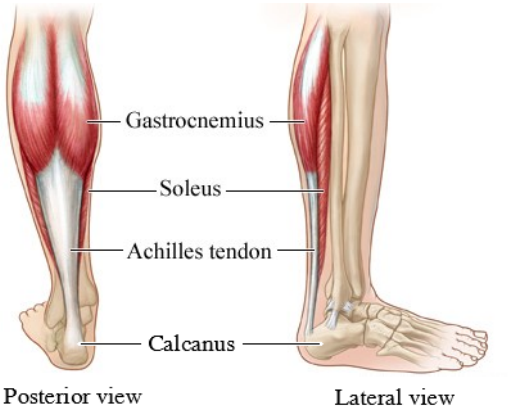

Figure 2.7: The anatomy of the Achilles tendon, adapted from Healthwise (2018)

On average, the length of the Achilles tendon is 15 cm, ranging between 11 - 26 cm. Its mean width is 6.8 cm (ranging between 4.5 - 8.6 cm) at its origin, and decreases to approximately 1.8 cm at its midsection (1.2 - 2.6 cm) (Del Buonu *et al.*, 2013). Approximately 4 cm above the calcaneus, the Achilles tendon cross-section becomes circular in shape. At the site of insertion over the posterior surface of the calcaneus, the Achilles tendon has an average width of 3.4 cm (ranging between 2.0 - 4.8 cm) (Apaydin *et al.*, 2009).

Stellenbosch University https://scholar.sun.ac.za

Physiology

Acting via the Achilles tendon, the gastrocnemius and soleus muscles act as ankle and foot flexors, while the gastrocnemius also acts as a knee flexor (Grumbine and Santoro, 1990). The gastrocnemius muscle is active during walking, running and jumping; and the soleus muscle is active during standing - it functions as a stabilizer of the foot (Del Buonu *et al.*, 2013). The activation of the triceps surae results in plantar flexion of the foot and ankle - i.e. the contraction of these muscles induces a pulling force on the Achilles tendon and results in the raising of the calcaneus and lowering of the forefoot, see Figure 2.8. It is estimated that the Achilles tendon generates approximately 93 % of the required plantar flexion force during walking and running (Moore *et al.*, 2011).

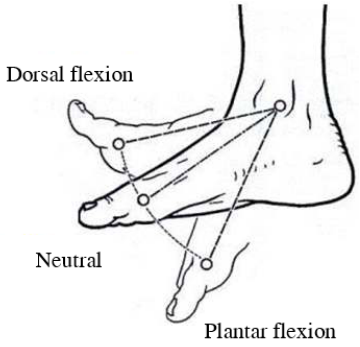

Figure 2.8: Illustration of the neutral position of the foot and ankle (flat), as well as the dorsal flexion (tilted-upwards) and plantar flexion (titled-downwards) of the foot (de Pina Filho and Dultra, 2013)

In addition to aiding the plantar flexion of the ankle and foot, the Achilles tendon is characteristically elastic. This characteristic is inherent to all tendons, and aids in shock absorption during walking, running and jumping. Furthermore, this characteristic allows for the Achilles tendon to function as an efficient storage compartment for kinetic energy during physical activities such as: walking, running and jumping.

Achilles Tendon During Running

As previously mentioned, the Achilles tendon plays an active role in the dorsal and plantar flexion of the foot and ankle, Figure 2.8. From this observation it is evident that the Achilles tendon would experience its peak load during the stance phase of the running gait cycle, and its minimum load (or no load at all, as suggested by Roberts and Belliveau (2005)) during the swing phase of the running gait cycle.

It is estimated that the peak loads experienced by the Achilles tendon during running range between 6.1 - 8.2 times the body weight of the individual (Scott and Winter, 1990). During uphill running, the gastrocnemius muscle increases in length during the stance phase, but shortens during the stance phase of level running - this is due to the increased dorsiflexion of the foot and ankle during uphill running (Lichtwark and Wilson, 2006). Simultaneously, the length of the Achilles tendon increases minimally. During

Stellenbosch University https://scholar.sun.ac.za

downhill running, the opposite holds true - the gastrocnemius muscle shortens in length, resulting in an decreased length of the Achilles tendon (Lichtwark and Wilson, 2006).

2.2.3 Patella Tendon

Anatomy

The patella is a sesamoid bone located within the quadriceps tendon. Unlike the Achilles tendon, the patella tendon connects the apex of the patella to the tibia, specifically to the tibial tuberosity (KenHub, 2019). Due to the fact that the patella tendon connects bone to bone, it is technically classified as a ligament (Barclay, 2017).

The patella tendon is a thin, flat band that, on average, has a length of 5 - 8 cm. It extends from the apex of the patella, across the anterior region of the knee, and connects to the joint capsule of the tibial tuberosity. Structurally, the patella tendon is a continuation of the quadriceps tendon, and it is for this reason that it is referred to as a tendon and not a ligament. Figure 2.9 illustrates the configuration of the patella tendon with respect to the surrounding muscles, tendons and bone structures.

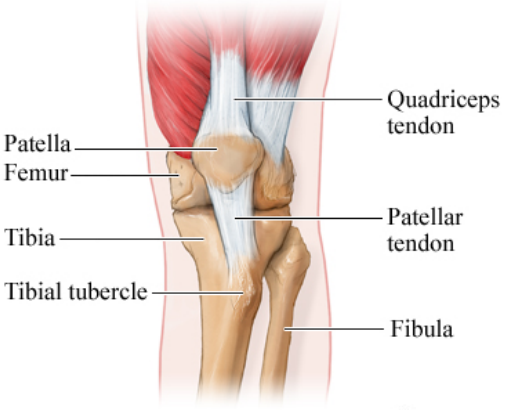

Figure 2.9: Anterior view of the anatomy of the patella tendon (Pope, 2018)

The medial and lateral components of the quadriceps tendon pass down either side of the patella tendon and attach to the upper extremities of the tibia. The posterior surface of the patella tendon is separated from the synovial membrane of the knee joint by a large cylindrical (infrapatella) pad of fat (Shaerf *et al.*, 2014).

Physiology

The patella tendon plays an integral role in the functioning of the knee joint and lower limb.

Acting via the patella tendon, the contraction of the quadriceps femoris muscle results in the extension of the leg, at the knee (KenHub, 2019) - i.e. the force is exerted on the quadriceps and the patella tendons, pull the tibia is proximally toward the thigh (Barclay, 2017). Figure 2.10 illustrates the four principle movements of the knee.

Stellenbosch University https://scholar.sun.ac.za

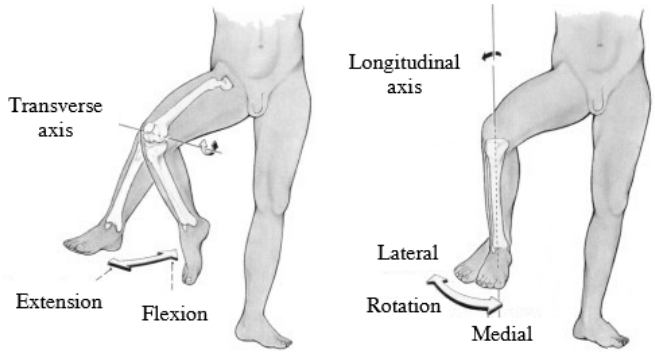

Figure 2.10: The four principle movements of the knee joint, namely: extension and flexion, as well as lateral and medial rotation (Islam, 2018)

It is important to note that during extension of the knee, the patella tendon shortens, and during flexion it is stretches.

Patella Tendon During Running

As previously mentioned, the patella tendon plays an active role in the extension and flexion of the knee, Figure 2.10. Similar to the Achilles tendon, the patella tendon experiences its peak load during the stance phase of the running gait cycle, and its minimum load during the swing phase of the running gait cycle. It is estimated that the peak loads experienced by the patella tendon during running range between 4.7 - 6.9 times the body weight of the individual (Scott and Winter, 1990).

2.2.4 Tendons as Springs

As mentioned previously, the musculotendinous units of the lower limbs absorb power by stretching (eccentric) just before shortening (concentric) to generate power. Figure 2.11 illustrates the force-length relationship of a tendon. The figure indicates that tendons can be classified as biological springs, as they recoil in a spring-like manner, returning nearly 95 % of the energy stored during stretching (Novacheck, 1998).

Previous studies have identified that there is no significant change in the length of the muscle fibres itself during running (Roberts *et al.*, 1997). Instead, however, it has been found that the stretching and recoil of the muscle's respective tendons are responsible for the majority of the length changes. From these observations, it can be concluded that muscles can be classified as the tensioners of their respective tendons (McMahon, 1990).

Stellenbosch University https://scholar.sun.ac.za

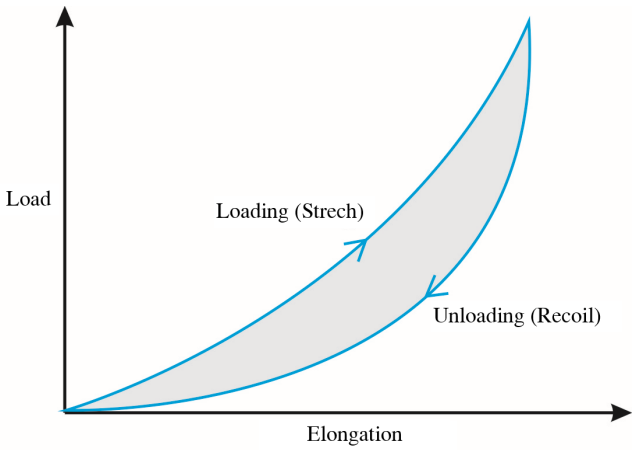

Figure 2.11: Load-Elongation curve for a tendon structure during the observation of stretching and recoil of the tendon when applied to a simple tension load (Robi *et al.*, 2013). The shaded area illustrates the energy loss (hysteresis) during the process of loading and unloading

The idea that the body's system of muscles, tendons, and ligaments, can be simplified and represented as a linear spring system, is supported and documented by researchers, including: Farley and Gonzalez (1996), Novacheck (1998), and Yu and Wilson (2014). Figure 2.12 illustrates the modified Hill-type muscle-tendon model that was investigated by Yu and Wilson (2014). The model suggests that the muscle component comprises of three elements, namely a: contractile element, damping element, and an elastic/spring element. The contractile element, denoted by CE in Figure 2.12, represents the force source when the muscle is activated. The damping element, denoted by b_m, represents the mechanical inefficiencies and energy loss in the muscle. The spring element, with a spring stiffness denoted by k_m, illustrates the minimal elastic behaviour of the muscle, and its ability to return back to its original length (Yu and Wilson, 2014). The tendon is modelled as a single spring element with a stiffness factor k_T, and the total force generated by the musculotendinous unit is denoted as F.

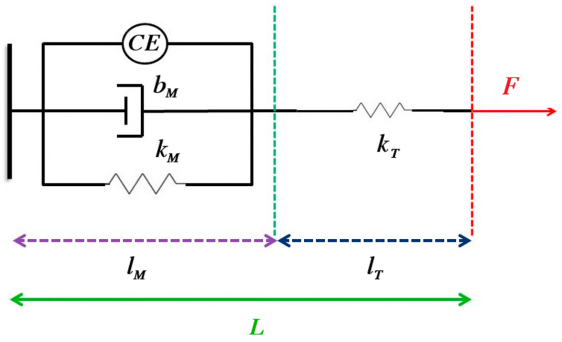

Figure 2.12: Modified Hill-type muscle-tendon model(Yu and Wilson, 2014)

Stellenbosch University https://scholar.sun.ac.za

2.3 Previous Work

As mentioned in Chapter 1, this project is a continuation of a previous Masters project (Groeneveld, 2020). The primary objective of the previous study was to investigate the feasibility of the use of an optic fibre sensor to measure the *in-vivo* dynamic loads of the Achilles and patella tendons during treadmill running. The secondary objective was to determine whether the optic fibre sensor could detect variability in the dynamic tendon loads as a function of extrinsic (gradient) and intrinsic (stride frequency) factors in running conditions (Groeneveld, 2020). Furthermore, the development of an optic fibre sensor capable of measuring the dynamic in-vivo tendon loads, and the investigation of the effect of the inserted optic fibre on running biomechanics, fell within the scope of the project.

2.3.1 Optic Fibre Sensor

The sensor operates on the principle of light intensity conveyed by the optic fibre thread during the cyclic loading and unloading of the tendons during running - as the tendon loads and unloads, the tendon compresses and deforms the suspended optic fibre thread through Poisson's mechanism (i.e. the force creates a micro-bend in the optic fibre) (Groeneveld, 2020; Muller *et al.*, 2018). This is proportional to the change in tendon force. The data acquisition module utilized was the NeXus-10 Biofeedback.

The effect of macro-bending, running, and skin movement on the sensor's ability to accurately measure the *in-vivo* loading profiles of the tendons were investigated. The tests concluded that: macro-bending with a radius larger than 10 mm would induce a maximal light intensity loss of 14.9 mV; a high impact activity such as running would alter the cyclic amplitude of the measurements, resulting in a measurement error of 5.69 % and 3.64 % for the patella and Achilles tendon respectively; skin movement would induce a peak measurement error of 9.4 % and 11.4 % for the Achilles and patella tendons, respectively.

2.3.2 Participant Selection

Five recreational runners, over 18 years of age, were recruited as participants for the previous study, Table 2.1. It was required that all of the participants were injury free, and had no history of knee, foot or ankle injury or pain.

Table 2.1: Summary of the selected participants biological data (Groeneveld, 2020)

Participant	Gender	Age (years)	Weight (kg)	Height (cm)
1	Male	37	82.0	177
2	Male	23	73.7	177
3	Male	24	98.8	197
4	Male	24	96.0	194
5	Male	19	76.3	184

Stellenbosch University https://scholar.sun.ac.za

2.3.3 Instrumentation and Facilities

The instrumentation and experimental tests were conducted at the Neuromechanics Unit Analysis Facilities of Stellenbosch University. Table 2.2 summarizes the instruments and tools utilized during experimental testing, and Figure 2.13 pictures the overall instrumentation and setup for the running trials. For further, more detailed information regarding the laboratory and acquisition setup, refer to Groeneveld (2020).

Table 2.2: Summary of the experimental instrumentation and tools used during testing (Groeneveld, 2020)

Instrument	**Description**
Bertec instrumented treadmill	A dual belt system, with an incline module and safety harness, as well as two force plates, one for each belt on the running platform (Bertec).
Vicon motion capture system	A motion capture system utilizing infrared cameras (10 x V5 infrared cameras) and reflective markers to track the motion of a subject.
Noraxon wireless electromyography (EMG) system	A surface-based EMG system, comprising of 16 active electrodes (MR3 v#.12.70, Noraxon, U.S.A.) affixed on the skin. The rectus femoris, vastus lateralis, vastus medialis, biceps femoris, semitendinosus, medial and lateral gastrocnemius, and tibialis anterior muscle groups were monitored.
Optic fibre sensor	Refer to Section 2.3.1.

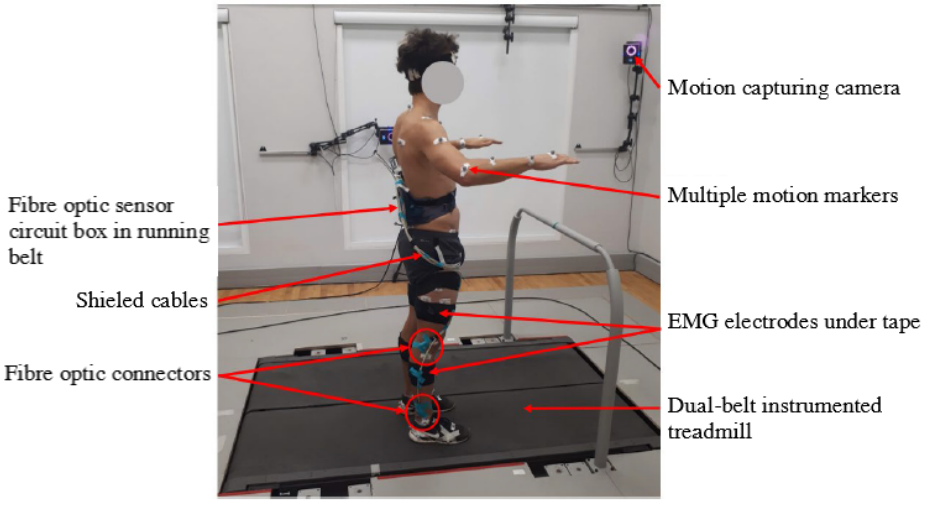

Figure 2.13: Overall instrumentation and setup of the participant (Groeneveld, 2020)

Stellenbosch University https://scholar.sun.ac.za

2.3.4 Experimental Protocol

The participants were subjected to six running trials, with each trial conducted under different running conditions. The trials conducted are listed below:

1. Level running at the participant's preferred speed
2. Level running, at the participant's preferred speed, with 110 % stride frequency of the participant's natural stride frequency
3. Level running, at the participant's preferred speed, with 90 % stride frequency of the participant's natural stride frequency
4. Level running at 2.78 m/s
5. Uphill running, 9° gradient, at 2.78 m/s
6. Downhill running, -9° gradient, at 2.78 m/s

2.3.5 Results

The study concluded that the developed optic fibre sensor is able to measure the *in-vivo* forces of the patella tendon during treadmill running - the measurement of the Achilles tendon forces proved challenging as the optic fibre threads broke during some of the running trials.

Participant 1 and 2 were the only participants that did not experience fibre threads breakage during running trials, with Participant 2 being the only participant with a full data set for both tendons. Groeneveld (2020) concluded that possible factors contributing to the fibre breakages included that Participants 3, 4, and 5 have impact peaks at the beginning of stance, where Participant 1 and 2 do not, as well as Participants 3, 4, and 5 being significantly taller than Participants 1 and 2 (see Table 2.1) - these factors would result in high cyclic loading of the tendons.

Furthermore, the optic fibre sensor was able to detect variability in the dynamic tendon loads as a function of extrinsic (gradient) and intrinsic (stride frequency) factors in running conditions. It was found that the peak force experienced by the Achilles tendon decreased during inclined and declined running conditions. Similarly, the peak force experienced by the patella tendon decreased during increased stride frequency and inclined running conditions (Groeneveld, 2020).

Groeneveld (2020) utilized Cohen's effect size (d) and p-value to quantify the effects of the inserted optic fibre on the running biomechanics of the participants. It was determined that majority of the calculated effect sizes were medium (0.2$<$ d $\leq$0.8) or large (d $>$0.8) (Groeneveld, 2020; Cohen, 1988), indicating that the surgically inserted optic fibre threads has a significant impact on the running biomechanics of the participants.

Stellenbosch University https://scholar.sun.ac.za

2.4 OpenSim

2.4.1 Background

Movement science is driven by observation, however, observation alone cannot elucidate the principles of human and animal movement (Seth *et al.*, 2011). Furthermore, biological systems are highly complex, and as a result, requires specialized software for constructing, validating and investigating them.

OpenSim is a freely available, open-source musculoskeletal modelling software that is primarily utilized for dynamic simulation and analysis of the human body. It is one of the flagship applications from *Simbios*, a National Institutes of Health (NIH) Centre for Biomedical Computation Systems at Stanford University, and was first released in 2007. Since 2007, the software has been used in hundreds of biomechanics laboratories and universities around the globe (OpenSim, 2017*a*).

OpenSim offers a wide range of advantages to its users, namely:

- Wide accessibility and cost effectiveness. OpenSim is free to download and use. OpenSim can be downloaded from the internet at: *https://simtk.org/*.
- A detailed modeling and simulation environment. OpenSim provides the necessary computational and simulation tools that complement observations and inform experimental design (Seth *et al.*, 2011).
- A wide selection of physics-based analyses for locomotion, see Section 2.4.2.
- Scripting capabilities in both Matlab and Python. OpenSim's core software architecture is accessible via an application programming interface (API) feed. The API documentation is available at: *https://simtk.org/api_docs/opensim/api_docs/*.
- Access to a large, active, online community of users. The platform connects researchers and facilities from around the globe, and as a result there exists the opportunity for collaboration between users to further improve, analyse and test developed models.

2.4.2 Gait Analysis Workflow

OpenSim offers its users a broad range of tools for the development and analysis of musculoskeletal models and dynamic simulations (OpenSim, 2017*g*). In this section the simulation and analysis tools provided by OpenSim will be discussed. Figure 2.14 illustrates the generic workflow diagram of the OpenSim software tools utilized in this study.

Stellenbosch University https://scholar.sun.ac.za

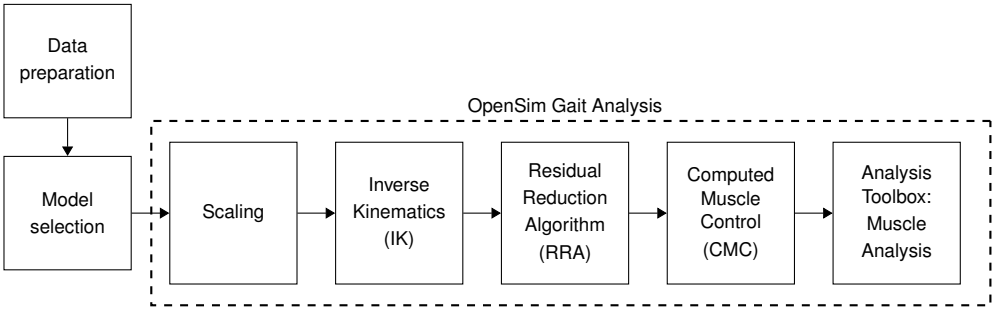

Figure 2.14: Overview of the a generic OpenSim workflow utilized in this study

Data Preparation

OpenSim is most commonly utilized for the analysis of experimentally obtained data sets. Typically, the data sets comprise of: marker trajectories or joint angles from motion capture systems, force plate data (GRFs, center of pressures (COPs), and moments), as well as muscle activation (EMG) signals.

Typically, motion data (marker trajectories and force plate data), from motion capture systems, are stored in Coordinate 3D (C3D) format, and muscle activation signals in comma-separated values (CSV) format. OpenSim does not support C3D or CSV formatted files, and requires that the relevant data set be specified and stored according to the following: marker trajectories using Trace (TRC) files, joint angles, force plate data, and EMG signals using Storage (STO) or Motion (MOT) files.

When preparing data for an *in-silico* environment, such as OpenSim, it is necessary to consider both the experimental (laboratory) and *in-silico* environment's coordinate systems. OpenSim uses the coordinate system, where: X is positive in the forward direction, Y in the upwards direction, and Z to the right. Usually, motion capture systems define their laboratory coordinate system as: X positive in the forward direction, Y to the left, and Z in the upwards direction. For this generic laboratory setup, a 90° rotation about the X axis is required before using in OpenSim - thus ensuring that the laboratory and *in-silico* reference frames are consistent with one another. Figure 2.15 illustrates an example of coordinate transformation in the OpenSim GUI, where the experimental motion capture data undergoes a 270° rotation about the X axis, and a 180° rotation about the Z axis.

Stellenbosch University https://scholar.sun.ac.za

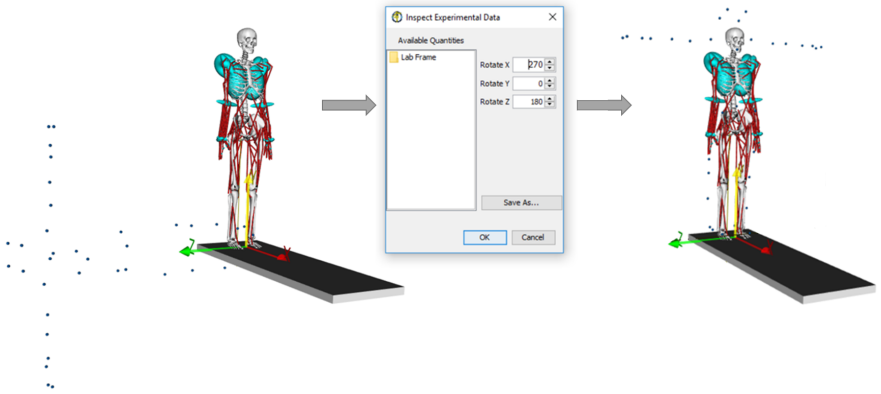

Figure 2.15: Example of a coordinate transformation in the OpenSim GUI, where the experimental motion capture data (markers illustrated in blue) undergoes a 270° rotation about the X axis, and a 180° rotation about the Z axis. The OpenSim coordinate system is given by the red (X), yellow (Y), and green (Z) orthogonal frame at the base of the musculoskeletal model. Adapted from Galloy *et al.* (2018)

Model Selection

An OpenSim model is an *in-silico* representation of the neuromuscular and musculoskeletal dynamics of a human or animal subject that is of interest to a particular study. The OpenSim model is made up of components corresponding to those of the physical system that combine to generate or describe movement. These components include: reference frames, bodies, joints, forces, constraints, controllers, and contact geometries.

In OpenSim, the skeletal system of a model is represented by a series of rigid bodies connected by joints and constraints. Muscles are modelled as specialized force elements, derived from the Hill-type muscle model discussed in Section 2.2.4, that act at specified muscle points, and are connected to rigid bodies.

A large repository of existing models, contributed by members of the SimTK and OpenSim communities, are available on the SimTK and OpenSim documentation webpages. The musculoskeletal models listed on the OpenSim documentation webpage comprise of: core models (models distributed with OpenSim and are actively supported by the OpenSim team), example models (models not distributed with OpenSim, but are actively supported by the OpenSim team), user-contributed models (models contributed by members of the OpenSim community, and are supported by their authors, not the OpenSim team), and SIMM models (models contributed by members of the SIMM community as SimTK projects).

Scaling

The first step in the OpenSim analysis workflow is model scaling, Figure 2.14. Scaling is only necessary if a generic model (from the existing library of OpenSim models) is be-

Stellenbosch University https://scholar.sun.ac.za

ing utilized. This is due to the fact that both anatomical and physiological discrepancies exist between the generic model and the captured experimental data for the subject. Hence, the purpose of scaling is to modify the anthropometry (physical dimensions), and mass properties of the generic musculoskeletal model to match those of the subject.

The scaling procedure followed by the scaling tool, can be summarized in five points:

1. Scale factors are calculated using measurement-based methods (which exploit the relationship between virtual and experimental marker placement) or manual scaling methods.
2. Body segments, joint frame locations, force application points, muscle attachment points, and mass center locations are scaled using the determined scale factors.
3. Mass and inertial properties of the generic model are altered based on the: calculated scale factors, total mass of the subject (input target mass (TM)), and preserve mass distribution (PMD) functionality.
4. Muscles and other length-dependent components, such as ligaments and actuators, are modified and scaled using a length ratio (ratio of the component's length before and after scaling).
5. The locations of the scaled model's virtual markers are updated and moved to match the locations of the experimental markers according to the weighted least squares (WLS) method.

Inverse Kinematics

Inverse Kinematics (IK) can be defined as the mathematical process of recovering the movement of a rigid body, based on the calculation of joint angles (referred to as coordinates in OpenSim documentation), which move the end-effector to the desired end location (Mathworks.com, 2019).

The IK tool operates by incrementally stepping through the dynamic motion, and computes the generalized coordinate values which position the model in a pose that "best matches" the experimental marker positions and coordinate values for that particular time step. To achieve this "best match" solution, the WLS method is utilized, Equation 2.1. The solution aims to minimize errors between the observed and calculated for both marker locations and coordinate values.

$$\min_{\boldsymbol{q}}\Big(\sum_{i\in Markers} w_i \left\|\boldsymbol{x}_i^{exp} - \boldsymbol{x}_i(\boldsymbol{q})\right\| + \sum_{j\in Coordinates} \omega_j(\boldsymbol{q}_j^{exp} - \boldsymbol{q}_j)^2\Big) \tag{2.1}$$

Where $\boldsymbol{q}$ represents the vector of generalized coordinates being solved for, $\boldsymbol{x}_i^{exp}$ represents the experimental position vector of marker i, $\boldsymbol{x}_i$ represents the position vector of the corresponding model marker, $\boldsymbol{q}_j^{exp}$ represents the experimental position vector for coordinate j, and $\boldsymbol{q}_j = \boldsymbol{q}_j^{exp}$ for all prescribed coordinates j. Furthermore, w_i and w_j represent the specified weights of markers i and j respectively (OpenSim, 2017*e*).

Stellenbosch University https://scholar.sun.ac.za

Inverse Dynamics

Dynamics is defined as the study of motion and its causes. Inverse Dynamics (ID), however, is defined as the determination of a rigid body's generalized forces (net forces and torques) based on the given kinematics of a body, and that body's inertial properties (OpenSim, 2017*b*).

From kinematic (model states or motion) and corresponding kinetic (external applied loads, such as GRFs) data sets, the ID tool calculates the generalized forces at experienced each joint responsible for a particular motion of the model. The equations of motion (EOM), outlined in Equation 2.2, and the given kinematic and kinetic data sets are used to solve for the internal forces and moments at each joint (OpenSim, 2017*b*,*d*).

$$\boldsymbol{M}(\boldsymbol{q})\ddot{\boldsymbol{q}} + \boldsymbol{C}(\boldsymbol{q}, \dot{\boldsymbol{q}}) + \boldsymbol{G}(\boldsymbol{q}) = \boldsymbol{\tau} \tag{2.2}$$

Where: $\boldsymbol{q}, \dot{\boldsymbol{q}}, \ddot{\boldsymbol{q}} \in R^N$ are the vectors of generalized positions, velocities, and accelerations, respectively; $\boldsymbol{M}(\boldsymbol{q}) \in R^{NxN}$ represents the system mass matrix; $\boldsymbol{C}(\boldsymbol{q}, \dot{\boldsymbol{q}})$ represents the vector of containing the Coriolis and centrifugal forces; $\boldsymbol{G}(\boldsymbol{q}) \in R^N$ is the vector of gravitational forces; and $\boldsymbol{\tau} \in R^N$ is a vector containing the generalized forces of the model (OpenSim, 2017*d*). Note that N represents the total number of degrees of freedom (DOF) in the model.

Residual Reduction Algorithm

A residual is defined as the difference, or error, between observed and computed results. The aim of conducting a residual reduction process is to minimize the cumulative effects of modelling and data processing errors on the final simulation results. In OpenSim, residuals are identified as the large, non-physical, compensatory forces, that arise from aggregated modelling and marker processing errors.

The objective of the Residual Reduction Algorithm (RRA) is to minimize the effects of residuals on the simulation by creating an adjusted, subject-specific, musculoskeletal model that is more dynamically consistent with the captured experimental kinematic and kinetic data sets. As a result, the adjusted model, when used in simulation, substantially reduces the effects of residuals and counters their non-real effects on the musculoskeletal model (Atkinson, 2018).

Modelling assumptions, noise, and other errors from experimentally obtained motion data lead to dynamic inconsistency and unstable simulation (OpenSim, 2017*f*). Dynamic inconsistency is indicated by the inability of the estimated ground reaction forces and acceleration of the model to satisfy Newton's Second Law, Equation 2.3.

$$\boldsymbol{F} = \sum_{i=1}^{n} m_i \boldsymbol{a}_i \tag{2.3}$$

In order to compensate for the dynamic inconsistency of the original model, the adjusted RRA model includes an additional residual force term in Equation 2.3, resulting in Equation 2.4. These force residuals are computed over the entire duration of the simulated movement.

Stellenbosch University https://scholar.sun.ac.za

$$\boldsymbol{F} + \boldsymbol{F}_{res} = \sum_{i=1}^{n} m_i(\boldsymbol{a}_i - \boldsymbol{g}) \tag{2.4}$$

Where $\boldsymbol{F}$ represents the experimental force vector; $\boldsymbol{F}_{res}$ represents the correction, residual force vector added by RRA, m_i and $\boldsymbol{a}_i$ represent the mass and acceleration vectors of the i^{th} body component, of n body components; $\boldsymbol{g}$ represents the gravitational force constant, g = 9.81 m/s^2 acting in the vertical direction.

The RRA tool executes four main processes (OpenSim, 2017*f*), namely:

1. Tracking simulation:
   RRA configures the model in its starting orientation, as calculated by the IK tool, and incrementally steps the simulation/motion. At each increment, the algorithm calculates the minimum required force and toque values of the each of the model's actuators, in order to achieve the desired end configuration whilst minimising a pre-defined objective function.

2. Mass centre adjustment:
   The model's torso centre of mass (COM) is adjusted such that any inaccuracies of mass distribution and geometry of the model's torso are corrected.

3. Mass adjustment recommendation:
   The algorithm calculates a recommended mass change for the model, and distributes the recommended mass changes proportionally among the model's body segments. It is important to note that these recommendations are not applied to the resulting RRA model, but if proven desirable, must be implemented manually by the user.

4. Adjusted kinematics:
   The tracking simulation implemented in Step 1 is repeated, with the following differences:

   - The model with the adjusted torso COM is used.
   - The residuals are weighted according to the minimisation of the pre-defined objective function.
   - Minimum and maximum bounds are placed on the calculated residual values.

Computed Muscle Control

The primary objective of the Computed Muscle Control (CMC) tool is to compute the muscle activation levels of a patient-specific dynamic model, which drive the model to track a set of desired kinematics in the presence of externally applied forces (OpenSim, 2017*c*).

The built-in tool achieves this objective with the utilisation of both feed-forward and feedback control loops, Figure 2.16. The tool utilises a combination of proportional-derivative (PD) controller and static optimisation (Thelen and Anderson, 2006).

Stellenbosch University https://scholar.sun.ac.za

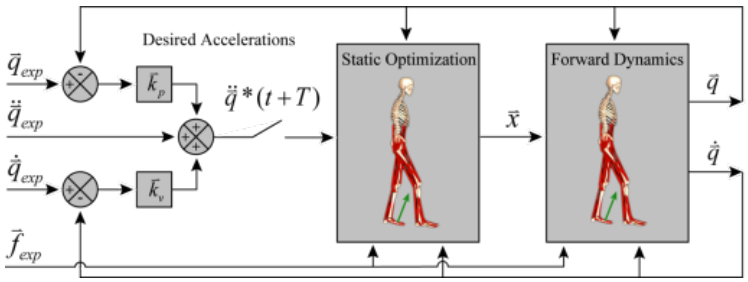

Figure 2.16: Schematic of the Computed Muscle Control (CMC) algorithm (Thelen and Anderson, 2006)

The CMC algorithm is executed in a continuous loop fashion, within which three processes (listed below) are conducted, until the desired simulation end-time is reached (OpenSim, 2017*c*). However, before the CMC algorithm is executed, the initial states of the model's generalized coordinates, speeds, and muscle states, are computed.

1. A set of desired accelerations, $\ddot{\boldsymbol{q}}^*$, that will produce the desired dynamic trajectory of the model, are calculated using PD control law, Equation 2.5.

$$\ddot{\boldsymbol{q}}^*(t+T) = \ddot{\boldsymbol{q}}_{\boldsymbol{exp}}(t+T) + k_v[\dot{\boldsymbol{q}}_{\boldsymbol{exp}}(t) - \dot{\boldsymbol{q}}(t)] + k_p[\boldsymbol{q}_{exp}(t) - \boldsymbol{q}(t)] \tag{2.5}$$

$$k_v = 2\sqrt{k_p} \tag{2.6}$$

   Where $\boldsymbol{q}$ and $\boldsymbol{q}_{exp}$ represent model and experimental coordinate vectors, respectively, k_v and k_p represent the critically damped, Equation 2.6, feedback control gains for the velocity and position errors, respectively, and finally, t and T represent the current time stamp and the minor step increment at which the accelerations are computed, respectively.

2. The required actuator controls that will achieve the desired accelerations obtained in Step 1, are calculated by solving the static optimization problem (aim: to minimize and distribute loads across actuators).

3. Standard forward dynamic simulation of the model is conducted, advancing forward in time by a set time interval, T, using the calculated actuator controls.

Analysis Toolbox: Muscle Analysis

In order to properly understand the results of a simulation, OpenSim offers a built-in simulation analysis tool. The primary aim of the toolbox is to provide the user with the means to properly analyse the performance and results of a model or simulation based on the model's number of inputs (e.g. time histories of model states, controls, and external loads) (OpenSim, 2017*g*). Analysis options provided by the toolbox include: body kinematics, point kinematics, joint reaction, induced acceleration, force reporter, and muscle analyses.

Stellenbosch University https://scholar.sun.ac.za

The muscle analysis functionality of the analysis toolbox reports the attributes of selected muscles that are involved in the dynamic simulation. Examples of the reported muscle attributes include: normalized and un-normalized fibre lengths and velocities, pennation angle (PA), and active-fibre lengths. Furthermore, OpenSim offers the ability to run any specific analysis from the analysis toolbox, in parallel with other tasks such as RRA and CMC.

2.4.3 OpenSim API

OpenSim's core software architecture is accessible in both Matlab and Python programming platforms via an API feed. This attribute provides OpenSim users with the unique ability to extend the inherent capabilities of OpenSim's software architecture and develop customizable workflows (Seth *et al.*, 2011). The following section will discuss the OpenSim framework, its capabilities, limitations, and compatibility requirements.

Framework and Architecture

The OpenSim framework is organized into several computational and functional layers, namely: SimTK/Simbody, Model, Analysis, and Application, Figure 2.17.

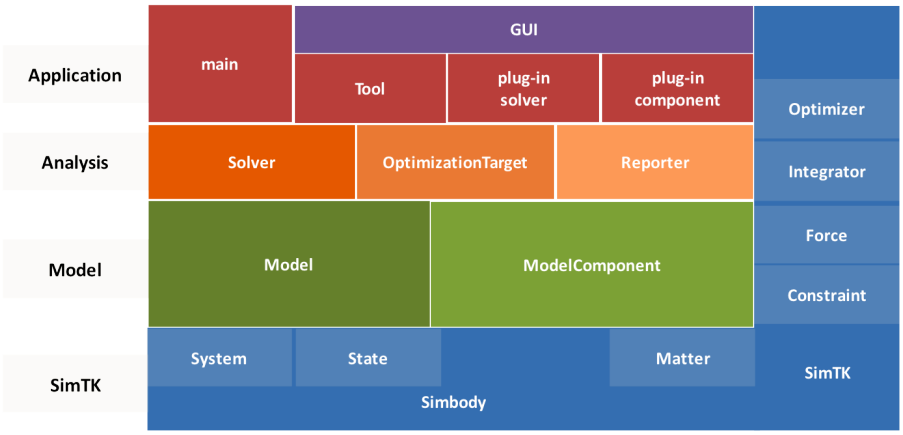

Figure 2.17: OpenSim framework and architecture (Seth *et al.*, 2011; Delp *et al.*, 2007)

With reference to Figure 2.17, the SimTK/Simbody (blue), Model (green), and Analysis (orange) layers make up the OpenSim API. The API forms the computational and functional foundation upon which the OpenSim Application (red) relies in order to operate.

The first layer of the OpenSim framework, also referred to as OpenSim's base layer, represents the computational infrastructure provided by SimTK (a free project hosting platform for computational focused-projects within the biomedical community) and Simbody (a free, open source, multi-body physics API). OpenSim utilizes SimTK and Simbody components, numerical methods, and other computational resources throughout its architecture as a base for constructing and solving multi-body dynamics systems (Seth *et al.*, 2011; Delp *et al.*, 2007).

Stellenbosch University https://scholar.sun.ac.za

The second layer of the OpenSim framework is the modelling layer and comprises of two main classes, namely: Model, and Model Component. This layer of the framework is responsible for the representation and assembly of the physical components of a model (such as bodies, joints, constraints, forces, actuators, and controllers), to form a coherent and consistent whole (Seth *et al.*, 2011; Delp *et al.*, 2007). Once a model has been constructed, a corresponding computational representation is realized as a Simbody System-State object. These two Simbody objects are used to manage the model's variables and parameters in the third and fourth layers of the framework structure.

The third layer of the OpenSim framework is the Analysis layer. It comprises of three different types of analysis sets, namely: modeller, solver, and reporter (Seth *et al.*, 2011; Delp *et al.*, 2007). A modeller analysis generates or modifies a model according to some specific criteria; a solver solves a set of equations presented by a model, for example solving inverse dynamics equations to determine joint moments; and finally, a reporter displays or records values of interest from a simulation.

The final layer of the OpenSim framework is the Application layer. This functional layer of the OpenSim framework contains a growing variety of applications, of which the focal/primary application is the OpenSim GUI - tool which provides OpenSim users with a visual interface to the OpenSim tools and analyses. Unlike the previous three layers, this functionality is not accessible to users via the API feed. The Application layer is a consumer of the API feed, and relies on it to generate applications, dynamic libraries, and analyses which may be loaded and executed by the GUI (Seth *et al.*, 2011; Delp *et al.*, 2007).

Capabilities and Limitations

The OpenSim API offers its users the ability to: perform batch processing of common workflows; run tools programmatically; access the API feed without the overhead of learning to program in C++; write "main" scripts similar to those written by C++ developers, and simultaneously take advantage of the many open-source Matlab/Python packages available for data processing, machine learning, statistics, etc.

The limitations placed on the OpenSim API users, include: users cannot create new components (such as custom muscles) or plug-in applications/tools for use through the GUI or command line; users cannot access certain OpenSim GUI plug-in tools (specifically the plotter or visualizer); and finally, many SimTK and Simbody classes which belong to the SimTK namespace and Simbody internals, are not available for use.

2.5 Statistical Methods

As highlighted in Chapter 1, two types of analyses will be conducted on the project's resulting *in-silico* models and workflows.

The first type of analysis to be conducted is that of a model sensitivity analysis. The purpose of this analysis is to quantify the degree to which the model's performance (specif-

Stellenbosch University https://scholar.sun.ac.za

ically the tendon loading patterns) is influenced, based on the modifications made to patella and Achilles tendon implementations in each of the modified models. Consequently, this analysis will focus on comparing the force magnitudes and trends (shape and timing) of the estimated tendon loading profiles of the Achilles and patella tendons of the modified models with respect to both the baseline model and the other modified models. Due to the fact that small permutations in model design may result in significant differences in the obtained tendon loading profiles, a statistical method which identifies differences between two continua is to be utilized. For this reason Statistical Parametric Mapping (SPM) techniques will be used. Refer to Section 2.5.1.

The second type of analysis to be conducted in this project is that of an independent trend analysis of the *in-silico* method's estimated tendon loading patterns. The purpose of this analysis is to determine whether or not the developed models and running analysis pipeline yield results that are good approximations of what (trends) is observed in reality. Consequently, this analysis will focus on the comparison between the estimated tendon loading patterns from the *in-silico* method to those of the *in-vivo* measurements obtained by Groeneveld (2020). One classical method for trend analysis in the biomechanics field is that of a regression analysis. In this project a simple, qualitative, linear regression analysis will be utilized to analyse the overall performance of the *in-silico* method as the reference data does not provide accurate amplitude values (Groeneveld, 2020). Refer to Section 2.5.2.

2.5.1 Statistical Parametric Mapping

Pataky (2012) defines Statistical Parametric Mapping as "a topological methodology for detecting field changes in smooth n-dimensional continua" (Pataky, 2012), and was originally developed for statistical inference analyses on neuroimaging datasets (Baeyens *et al.*, 2019).The **spm1d** toolbox, developed by Pataky (2012), is a freely available and open-source software platform developed for conducting SPM analyses on 1-dimensional (1D) datasets. The toolbox is compatible with both Matlab and Python, and like OpenSim, has an active online community.

The toolbox utilizes Random field theory (RFT) (Adler and Taylor, 2007) expectations to compute statistical inferences between continua (Pataky, 2019, 2010). Specifically, the RFT methodology employed by the **spm1d** toolbox for statistical inference calculations is that of the classical height-threshold cluster-breadth method (Pataky, 2010; Evans *et al.*, 1994). In short, this methodology states that the height and width of clusters, which arise from smooth random fields, are inversely proportional to the probability of their occurrence - i.e. clusters that are very broad and/or very high, are expected to occur with low probability (Pataky, 2010; Evans *et al.*, 1994).

Moreover, the **spm1d** toolbox computes a p-value for clusters of statistics (e.g. t) that cross a calculated critical threshold (t^*), instead of computing a p-value for each data point. Consequently, the likelihood of the inflation of a Type I statistical error (the rejection of a true null hypothesis, otherwise known as a "false positive" conclusion), during the statistical analysis process, is mitigated (Baeyens *et al.*, 2019).

Stellenbosch University https://scholar.sun.ac.za

The **spm1d** toolbox calculated the critical thresholds (t^*) are in accordance with the Type I error rate: $\alpha = 0.05$, where α is the statistical significance level (typically $0 < \alpha < 1$). This condition implies that when an observed t-statistic crosses the critical threshold value, the cluster will have a p-value less than the defined statistical significance level (i.e. $p < \alpha$), consequently allowing the researcher to reject the null hypothesis (H_0) of no difference between the two analysed continua.

A wide range of statistical analysis tools are incorporated in the **spm1d** toolbox, including: one- and two-sample t-tests, analysis of variance (ANOVA) tests, multivariate tests, as well as summary statistic tools (such as mean and standard deviation clouds). In this project, the **spm1d** toolbox, and more specifically, the two-sample t-test functionality, will be utilized to analyse model sensitivity.

In statistics, a two-sample t-test is used to determine the difference between two population means. A common application for this is in clinical research, where the results of two independent datasets are compared to one another (Feng *et al.*, 2017). As previously mentioned, the two-sample t-test will be used to determine differences between the tendon loading profiles observed for the investigated models, with reference to both the generic and the other modified models.

The two-sample t-tests conducted in this project will utilize a two-tailed approach, where the critical area and threshold value of the resulting distribution is considered in both scenarios where the sample is greater or less than the determined threshold, and assume that the datasets have an unequal variance (in general, different groups of observations can have different variances, hence this needs to be considered). Figure 2.18 illustrates an example output of the toolbox's two-sample t-test functionality.

Stellenbosch University https://scholar.sun.ac.za

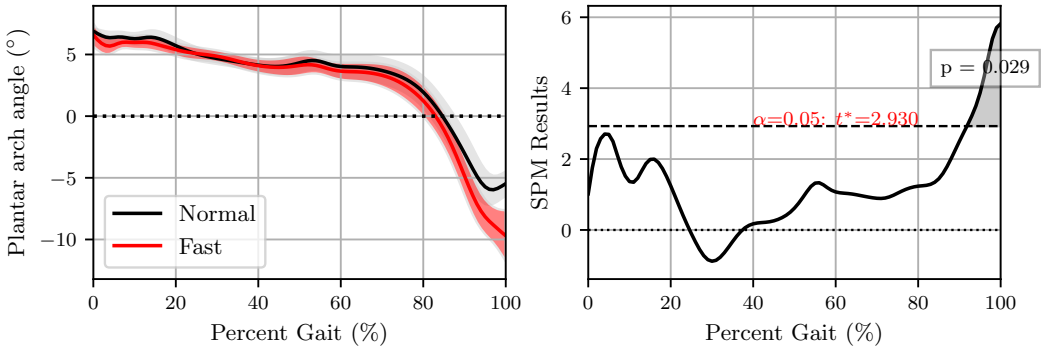

Figure 2.18: An example output plot of the **spm1d** toolbox's two-sample t-test. The example analyses differences in a subject's plantar arch angle during normal (black) and fast (red) walking (Caravaggi *et al.*, 2010). The first subplot (left) illustrates the mean and standard deviation clouds of the two datasets being analysed. The second subplot (right) illustrates the results of the SPM analysis, where the grey, shaded region indicates a region (cluster) of statistical significance (i.e. where the two datasets are statistically different), and its corresponding p-value ($p = 0.029$). Additionally, the second subplot indicates the statistical significance level ($\alpha = 0.05$) and critical threshold ($t^* = 2.930$) values. Adapted from Pataky (2019)

2.5.2 Regression Analysis

Regression analysis is a powerful statistical method which allows researchers to estimate and examine the relationship between two or more variables of interest (Blettner *et al.*, 2010). An added advantage of regression analysis tools is their prediction and forecasting capabilities through the determined regression model. The most common form of regression analysis is that of linear regression, where the linear relationship that most closely fits the data according to a specific mathematical criterion, such as the ordinary least squares criterion (OLS), is determined. In this project linear regression analysis, augmented by the OLS criterion, will be used.

A common way to observe the relationship between an independent and dependent variable of a regression analysis is through the use of a regression analysis plot. On this plot the datum (independent) variable is plotted on the X axis, and the comparative (dependent) variable on the Y axis. Using this plot the linear regression model (equation), as well as the coefficient of determination (R^2) for the analysed data, may be calculated. Equation 2.7 shows the mathematical format of a linear regression model.

$$y = mx + c \tag{2.7}$$

Where y is the model's dependent/response variable, x is the model's independent variable, m is the gradient of the regression model, and c is model's the Y axis intercept value. Due to the fact that the OLS criterion is used to determine the linear regression model, the gradient and intercept parameters of the regression model (m and c) are determined by minimizing the sum of the squares of the differences between the observed

Stellenbosch University https://scholar.sun.ac.za

dependent variable values in the given dataset and those predicted by the model.

The coefficient of determination (R^2) may be interpreted as a percentage of how well variation in one variable explains variation in the other, more specifically it acts as a measure of analysing the "fit" of the regression equation to the analysed data. R^2 can range between 0 and 1 (Blettner *et al.*, 2010), where a R^2 value of 0 represents a model that has a poor "fit" to examined datasets and further illustrates that the model does not explain or account for any variation in the dependent variable around its mean. Conversely, a R^2 value of 1 illustrates a perfect model-data "fit", where the model explains all of the variation observed in the dependent variable. An example of a regression plot is shown in Figure 2.19.

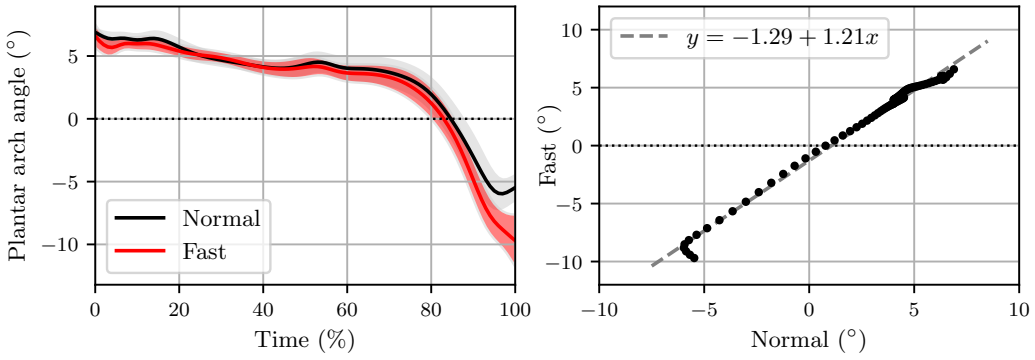

Figure 2.19: Example of a regression analysis plot. The example analyses differences in a subject's plantar arch angle during normal (black) and fast (red) walking (Caravaggi *et al.*, 2010). The first subplot (left) illustrates the mean and standard deviation clouds of the two datasets being analysed. The second subplot (right) illustrates the results of the regression analysis, where the grey dashed line indicates the regression equation, y, and the black dots represent the superimposed walking conditions. For this example, R^2 is calculated as 0.99, indicating that 99 % of the variation observed in the subject's plantar arch angle during fast walking can be explained by the regression model.

Stellenbosch University https://scholar.sun.ac.za

3 Model Development

The following chapter documents the generic model selection and modification processes conducted in this study. Additionally, an overview of the resulting modified models is presented in the final section of this chapter. All supplementary information for this chapter may be found in Appendix A.

3.1 The OpenSim Model

The "Full Body Running" model is a three-dimensional, 29 DOF OpenSim model of the human musculoskeletal system (Hamner *et al.*, 2010). The model comprises of 12 body segments, and 92 musculotendon actuators of the lower extremities and torso. It is based on the "gait2392" OpenSim core model (Delp, 1990; Delp *et al.*, 1999), and was originally developed to investigate how muscle activity in the lower limbs contributes to the propulsion (forward acceleration) and support (upward acceleration) of the body's center of mass during running (Hamner *et al.*, 2010). Figure 3.1 illustrates the anterior and posterior views of the three-dimensional "Full Body Running" model.

Figure 3.1: Anterior (left) and posterior (right) views of the three-dimensional "Full Body Running" model (Hamner *et al.*, 2010)

The default, unscaled version of the model represents a male subject that is approximately 1.7 m tall, and has a mass of 75.16 kg. Furthermore, the model is equipped with 41 generic virtual markers (not shown in Figure 3.1). This model was selected as the baseline model for this study as it is not only commonly used for the development of other musculoskeletal models, such as the "Full Body" model (Rajagopal *et al.*, 2016) and "Full Upper and Lower Body" model (Lai *et al.*, 2017) (both of which are suitable

Stellenbosch University https://scholar.sun.ac.za

for investigating the role of the lower extremities during running), but it is also a user-contributed OpenSim model that is well maintained and has an active online support forum. Additionally, the model presents opportunity for modification and expansion, suitable for the scope of this study.

3.1.1 Joint Geometry

The lower and upper extremities of the model each comprise of 6 body segments. The lower extremities comprise of the pelvis and a left and right lower limb (each consisting of a femur, tibia/fibula, talus (ankle), calcaneus (heel), and toes). The upper extremities comprise of a torso and head (HAT) complex, and a left and right arm (each consisting of a humerus, ulna, radius, and hand).

Each lower and upper limb of the model has 5 DOF. The lumbar spine, hip, and shoulder joints are modelled as 3 DOF ball-and-socket joints (Anderson and Pandy, 1999; Seth *et al.*, 2010; Holzbaur *et al.*, 2005). The knee joints are modelled as custom 1 DOF revolute joints (Seth *et al.*, 2010), whereas, the ankles, elbows, and forearms are modelled as 1 DOF revolute joints (Delp *et al.*, 1999; Holzbaur *et al.*, 2005). The pelvis is modelled as a 6 DOF free joint (Hamner *et al.*, 2010).

It is important to note that the origin of the pelvic frame is defined as the midpoint between the left and right anterior superior iliac spine (ASIS) (Hamner *et al.*, 2010; Atkinson, 2018). Furthermore, the model assumes that the neutral position of the pelvic frame is aligned to that of the ground frame (Hamner *et al.*, 2010). This assumption differs from findings in clinical trials, which suggest that neutral pelvic tilt is subject specific and is typically between 7° and 10° (Lembeck *et al.*, 2005), and may cause differences between simulated and literature results for pelvic tilt.

3.1.2 Muscle Geometry

The model's 92 musculotendon actuators can be physiologically summed to 76 muscles (Delp *et al.*, 1999; Anderson and Pandy, 1999). This is due to the fact that some of the larger, more diversified muscles, which act in more than one direction, are modelled using a series of independent muscle elements, Figure 3.2.

Anatomical landmarks on the bone geometry of the model are used to define the lines of action of the musculotendon actuators (Anderson and Pandy, 1999; Delp, 1990; Au and Dunne, 2012). Typically, it is sufficient to define a muscle's line of action using a single origin and insertion point, however for muscles that span over more than one joint, or wrap over bone (e.g. the quadriceps muscles), it is necessary to define additional, intermediate points along the musculotendon's line of action. These intermediate points are called "via points" and are necessary to avoid a wrong muscle path - a path where muscle pass though bones and/or deeper muscles at specific joint angles (Delp *et al.*, 1999; Trinler, 2016).

Stellenbosch University https://scholar.sun.ac.za

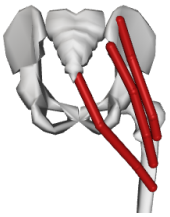

Figure 3.2: Representation of the gluteus maximus in the “Full Body Running” model. Three muscle-tendon units are used to define the entire muscle

The musculotendon units (MTUs) in the Hamner *et al.* (2010) model are modelled according to an adapted Hill-type model proposed by Thelen (2003), Figure 3.3 - implemented in OpenSim as the “Thelen 2003 Muscle Model”.

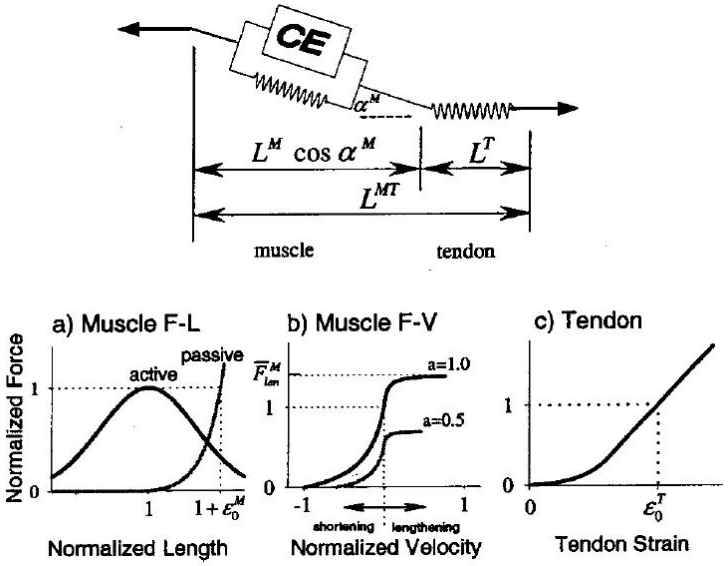

Figure 3.3: The Hill-type muscle-tendon model presented by Thelen (2003)

The MTUs are modelled using three components: a contractile element (CE), a parallel elastic element (PEE), and a series elastic element (SE). Furthermore, the muscle force generated by the modelled MTU is a function of muscle-fibre activation, normalized length, and normalized velocity of the MTU.

In OpenSim, muscle-tendon actuators are characterized by four parameters, namely: maximum isometric force, optimal muscle-fibre length (length of the muscle fibre at which it can generates the greatest force during isometric contraction), pennation angle (angle between a muscle’s longitudinal axis and its fibres), and tendon slack length (length below which the tendon, and muscle, generates zero force).

The maximum isometric forces of the modelled muscles in the Hamner *et al.* (2010) model, are adapted from the “gait2392” model (Delp *et al.*, 1999; Anderson and Pandy, 1999). Similarly, optimal fibre length and pennation angle values were taken directly

Stellenbosch University https://scholar.sun.ac.za

from Wickiewicz *et al.* (1983) and Friederich and Brand (1990). The tendon slack length values were derived from Delp (1990), where the tendon slack length was estimated by accounting for the optimal muscle fibre length and the joint angle at which the MTU can generate the largest force during isometric contraction (Trinler, 2016; Delp, 1990).

The maximum isometric force generated by a muscle can be estimated using the specific tension of mammalian tissue (reported estimates vary widely, from 15 N/cm^2 to over 100 N/cm^2 (Maganaris *et al.*, 2001; Buchanan, 1995), typically 60 N/cm^2 is used (Rajagopal *et al.*, 2016)) and the muscle's physiological cross sectional area (PCSA) (Rajagopal *et al.*, 2016; Delp *et al.*, 1999). Equation 3.1 has been used by musculoskeletal model developers to estimate maximum isometric muscle force.

$$F_0^M = \sigma_0^M \frac{PCSA^M}{l_0^M} \tag{3.1}$$

Where M identifies a variable as a muscle parameter, F_0^M is the maximum isometric muscle force (N), σ_0^M is the specific tension of mammalian tissue (N/cm^2), $PCSA^M$ is the PCSA of the muscle, and l_0^M is the optimal muscle fibre length.

Unlike the model's lower extremities, its upper extremities are driven by idealized torque actuators. The inertial properties of the arms were estimated from de Leva (1996) (Hamner *et al.*, 2010). The inertial properties of the model are tabulated in Table A.1.

3.1.3 Limitations of the Model

Although the Hamner *et al.* (2010) model is one of the most commonly used models for model development and running gait analysis in literature, two crucial limitations exist.

The first limitation presented by the Hamner *et al.* (2010) model is the over-simplified joint model adopted for the knee. As previously mentioned, the knee joint is modelled as a single DOF, custom joint, originally described by Yamaguchi and Zajac (1989), which was further adapted by Delp *et al.* (1999). Although the joint model technically accounts for both the patellofemoral and tibiofemoral joint kinematics in the sagittal plane (Atkinson, 2018), the joint lacks the incorporation of the patella bone, a component which will be incorporated in the modified models. The sesamoid bone was omitted by Delp *et al.* (1999) in the "Full Body Running" model's preceding model, the "gait2392" model, as it was assumed that it would impose constraints on joint kinematics. Recent studies, however, have indicated that through the utilization of compatible tibiofemoral and patellofemoral kinematic joint descriptions, it is possible to incorporate the patella bone in musculoskeletal models (Rajagopal *et al.*, 2016; Lai *et al.*, 2017; Schmitz and Piovesan, 2016).

Although the patella tendon is not independently modelled, it is incorporated in the "Full Body Running" model as the cumulative tendon of the quadriceps muscles, in particular the rectus femoris, vastus lateralis, intermedius, and medialis muscles. Furthermore, modelling implementation techniques used for the quadriceps muscles during high degrees of knee flexion are unrealistic because the quadriceps muscles wrap around the base of the femur, Figure 3.4.

Stellenbosch University https://scholar.sun.ac.za

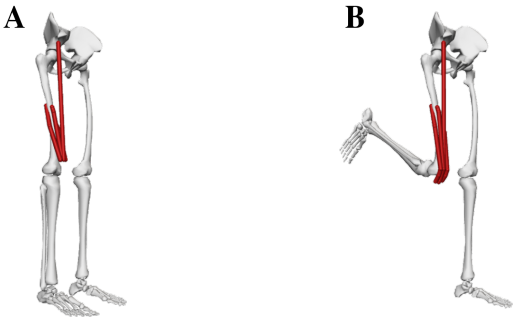

Figure 3.4: Illustration of the "Full Body Running" model's quadriceps muscle paths at 0° (**A**) and 120° (**B**) knee flexion angle, respectively (Hamner *et al.*, 2010)

The second limitation present is the presence of unrealistic, simplified musculotendon paths. As previously mentioned, the definition of a MTU's active path is crucial in order to obtain realistic and reliable muscle activation signals and forces during a simulation. The active muscle path of the gastrocnemius muscle in particular is of concern, as it directly influences the Achilles tendon. Like the patella tendon, the Achilles tendon is modelled as the cumulative tendon of the soleus, medial, and lateral gastrocnemius muscles. In the Hamner *et al.* (2010) model, the muscle paths for the calf muscles is modelled as a straight line. In reality, the calf muscles act along a curved path (i.e. the bulkiness of the calf muscle at the superior area of the tibia, Figure 2.7). It is desirable that an alternative, realistic active path of the two gastrocnemius muscles are realized in the modified models.

3.2 Model Modifications

The following section documents the modifications made to the Hamner *et al.* (2010) model, in order to rectify the limitations highlighted in Section 3.1.3. The section focuses on the incorporation of the patella bone geometry, independent patellofemoral joint (and its compatible tibiofemoral joint), as well as the modifications made to the musculotendon paths in the developed models. Furthermore, the different model implementations of the Achilles and patella tendons are presented and discussed.

3.2.1 Patella Bone

The patella bone is a key component of the knee joint. It functions primarily as an anatomic pulley for the quadriceps muscles, and increases the angle at which the quadriceps and patella tendon pulls on the shaft of the tibia during knee extension (Shahib and Zehra, 2020).

In the modified models, the incorporation and visualization of the patella bone is realized. It is located and attached to the distal end of the femur by means of the patellofemoral joint, described in Section 3.2.2. Additionally, the muscle-tendon paths of the quadriceps muscles have been modified such that their inferior ends attach to the superior area of the patella, and no longer wrap around the base of the femur during knee flexion. The fixed body coordinate system of the patella is located at the bone's

Stellenbosch University https://scholar.sun.ac.za

distal pole, with the axes defined in the same manner as the generic OpenSim coordinate frame (Y positive in the vertical direction, X in the anterior direction, and Z to the right). The mass and inertial properties of the patella bone geometry are defined according to cadaver literature (Delp, 1990; Anderson and Pandy, 1999), and is summarized in Table A.3.

3.2.2 Patellofemoral Joint

The patellofemoral joint "connects" and describes the path along which the patella may translate and rotate, with respect to the distal end of the femur, Figure 3.5.

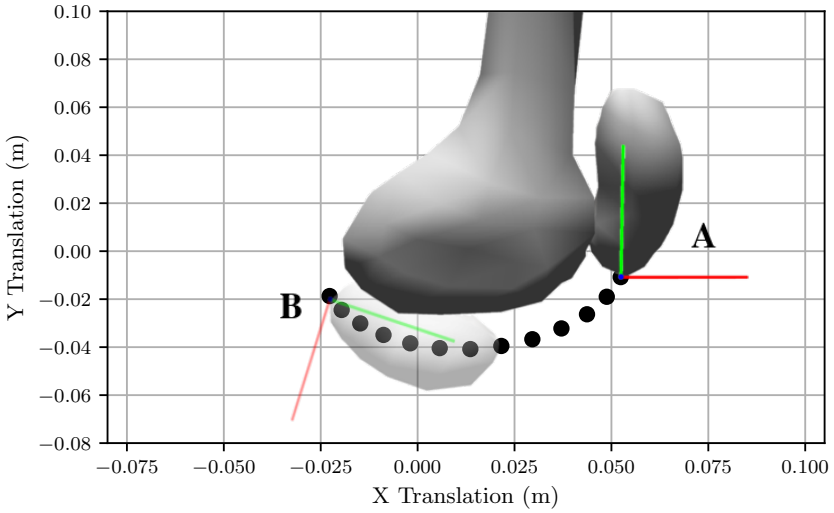

Figure 3.5: Graph illustrating the translation and rotation of the patella, expressed in the femur's coordinate system, during different angles of knee flexion. Note that the black points illustrate the location of the patella's coordinate frame origin. Y is positive in the superior direction (green), X in the anterior direction (red), and Z out of the page (blue). Full knee extension (0°) is indicated at **A**, and maximum knee flexion (120°) at **B**

Similar to models in literature, the patellofemoral joint implemented in this study's modified models resembles that of a single DOF, custom joint (Arnold *et al.*, 2010) whose resulting DOF is linearly related to knee flexion angle. This linear relationship between the two DOF is achieved using a coordinate coupling constraint.

3.2.3 Tibiofemoral Joint

The Hamner *et al.* (2010) model's knee joint is modelled as a modified 1 DOF joint (Yamaguchi and Zajac, 1989; Delp, 1990). Due to the existing limitations of the Hamner *et al.* (2010) model, and the dependency of the previously discussed patellofemoral joint on the tibiofemoral joint mechanics, it was necessary to redefine the joint's translation and rotation mechanics. The tibiofemoral joint mechanics presented by Walker *et al.* (1988) are compatible to the Arnold *et al.* (2010) patellofemoral joint implemented in the modified models, and have been used concurrently in numerous models (Rajagopal

Stellenbosch University https://scholar.sun.ac.za

et al., 2016; Arnold *et al.*, 2010; Schmitz and Piovesan, 2016; Lai *et al.*, 2017).

The 3-dimensional tibiofemoral joint mechanics defined by Walker *et al.* (1988) are based on experimental data captured from 23 cadaveric knees. Five DOF of the knee were investigated by Walker *et al.* (1988), namely varus-valgus and internal-external rotation, as well as superior-inferior, lateral-medial, and anterior-posterior translation. Walker *et al.* (1988) fitted these DOF to equations as a function of knee flexion angle (where knee flexion was defined as positive), and are shown in Equations 3.2 to 3.6.

$$varus = (0.0791 \times f) - (5.733e^{-4} \times f^2) - (7.682e^{-6} \times f^3) + (5.759e^{-8} \times f^4) \quad (3.2)$$

$$introt = (0.3695 \times f) - (2.958e^{-4} \times f^2) + (7.666e^{-6} \times f^3) \quad (3.3)$$

$$x = 0.00 \quad (3.4)$$

$$y = (0.0983 \times f) - (8.804e^{-4} \times f^2) - (3.750^{-6} \times f^3) \quad (3.5)$$

$$z = -(0.1283 \times f) + (4.796e^{-4} \times f^2) \quad (3.6)$$

Where f is the knee flexion angle in degrees. The resulting units for rotation and translation are in degrees and mm, respectively.

Walker *et al.* (1988) defined the tibiofemoral joint coordinate frame as: Y positive in the superior direction, X in the medial direction, and Z in the anterior direction. It is important to note that a knee angle range of 0° (full extension) to 120° (maximum flexion) is realized in the models developed during this study. Where, at full knee extension, the coordinate frames of both the femur and tibia are aligned, with the patella resting in the trochlear grove. As a result of modelling the tibiofemoral and patellofemoral joints using Walker *et al.* (1988) and Arnold *et al.* (2010) relations, bone-bone penetration (between the femur and patella), as well as fibre-bone penetration (between the patella tendon and tibia), are avoided at large knee flexion angles in the modified models.

3.2.4 Quadriceps Muscles Wrapping Surfaces

Wrapping surfaces are geometric shapes which may be utilized in musculoskeletal models to constrain and mould the active paths of muscle fibres. In OpenSim ellipsoidal and cylindrical wrapping surfaces are most common. Studies show that cylindrical surfaces provide a more computationally efficient solution than ellipsoidal surfaces (Rajagopal *et al.*, 2016). Typically, model developers utilize wrapping surfaces to improve the physiological accuracy of fibre paths and moment arms throughout a model's range of motion. Additionally, wrapping surfaces are used to prevent fibre-bone penetration.

A cylindrical wrapping surface with a diameter of 60 mm has been fixed at the distal end of both femurs in each of the modified models (Rajagopal *et al.*, 2016; Arnold *et al.*, 2010; Lai *et al.*, 2017). The quadriceps muscles which attach to the superior area of the

Stellenbosch University https://scholar.sun.ac.za

patella bone, namely the rectus femoris, vastus lateralis, vastus medialis, and vastus intermedius muscles, are constrained to wrap over this cylinder such that no muscle-bone penetration occurs throughout the model's knee angle range, Figure 3.6. By doing this large, unrealistic muscle forces are avoided during muscle simulations.

Figure 3.6: Illustration of the use of a cylindrical wrapping surface (i.e. the aqua cylinder pictured in **B**) at the distal end of the femur in the developed models. To prevent muscle-bone penetration, unrealistic muscle paths and large muscle forces (observed in **A**), the rectus femoris, vastus lateralis, vastus medialis, and vastus intermedius muscle fibres are programmed to wrap over the cylindrical surface at all angles of knee flexion (**B**). The figure illustrates surface wrapping capabilities at 120° knee flexion

3.2.5 Patella Tendon

The following section documents three different variations of the patella tendon, which are incorporated in the modified models.

Variation 1: Single Ligament Fibre

In the first variation, the patella tendon is modelled as an independent, single ligament fibre that spans from the distal pole of the patella to the tibial tuberosity on the tibia, Figure 3.7. This variation of the patella tendon is adapted from the Arnold *et al.* (2010) "Lower Limb" model's single muscle-fibre implementation of the tendon as well as the discrete element (DE) model of the knee developed by Schmitz and Piovesan (2016).

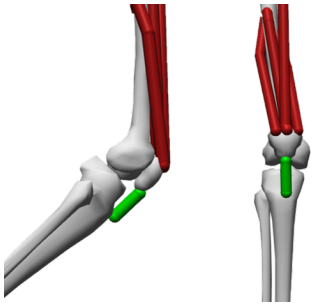

Figure 3.7: The single ligament fibre implementation of the patella tendon (green fibre). The quadriceps muscle fibres (red fibres), in particular the rectus femoris, vastus lateralis, vastus medialis, and vastus intermedius muscle fibres, connect the femur to the superior area of the patella

Stellenbosch University https://scholar.sun.ac.za

Unlike the patella tendon in the Arnold *et al.* (2010) model, the single fibre implementation of the patella tendon is modelled as an inextensible ligament (using the OpenSim ligament class). In order to model a ligament in OpenSim, three parameters need to be defined: PCSA force, resting length, and the normalized force-length relationship curve.

OpenSim defines the PCSA force as the force magnitude used to scale the normalized force-length curve, and is equal to the maximum isometric force which may be experienced by the implemented ligament (Delp *et al.*, 2007). It is important to note that in reality the force experienced by a tendon is a function of both muscle force and muscle-tendon pennation angle - hence, the resultant tendon and muscle forces are not necessarily equivalent. According to literature, peak patella loads experienced during high impact activities such as running, range between 4.7 - 6.9 times body weight (Scott and Winter, 1990). This roughly equates to the 5000 N - 6000 N range documented in numerous *in-vivo* studies (Schmitz and Piovesan, 2016; Svensson *et al.*, 2012; Heinemeier and Kjaer, 2011; Kapandji, 1985). Using this information, the PCSA force for the modelled tendon is set as 6000 N.

The resting length of a ligament is the same as tendon slack length, it is the length below which the ligament experiences no force. According to research, the patella tendon's resting length typically lies within the range of 40 - 50 mm (Schmitz and Piovesan, 2016; Svensson *et al.*, 2012; Sheehan and Drace, 2000; van Eijden *et al.*, 1986; Alegre *et al.*, 2016). Consequently, the resting length for the modelled tendon is set as 45 mm.

The normalized force-length curve describes the normalized force exerted by a ligament fibre as a function of its normalized length. For consistency, this parameter was adapted from the tendon force-strain relationship reported by Thelen (2003), as the Hamner *et al.* (2010) model's muscles are modelled according to the Hill-type model reported by Thelen (2003), refer to Section 3.1.2.

The tendon force-strain relationship reported by Thelen (2003) is defined as a piecewise, exponential-linear function. Where the exponential function describes the tendon's compliant mechanics in the toe-region (0 % - 1.5 % strain), and the linear function describes the tendons mechanics in the linear-elastic region (1.5 % - 10 % strain). To obtain a normalized force-length relationship, the force-strain equation (Thelen, 2003) was modified by writing strain (ϵ^T) as a function of normalized tendon length, Equation 3.7. The resulting normalized force-length relationship is shown in Equation 3.8, and is further illustrated in Figure A.4.

$$\epsilon^T(\widetilde{l^T}) = \widetilde{l^T} - 1 \quad \text{where: } \widetilde{l^T} = \frac{l^T}{l_0^T} \tag{3.7}$$

$$\frac{F(\widetilde{l^T})}{F_0^M} = \begin{cases} 0.10377(e^{91(\widetilde{l^T}-1)} - 1) & 1 \leq \widetilde{l^T} < 1.01516 \\ 37.526(\widetilde{l^T} - 1) - 0.26029 & 1.01516 \leq \widetilde{l^T} < 1.1 \end{cases} \tag{3.8}$$

Where l^T and l_0^T are the actual and resting lengths of the tendon, respectively. $\widetilde{l^T}$ is the normalized tendon length, $\epsilon^T(\widetilde{l^T})$ is the tendon strain as a function of normalized length, $F(\widetilde{l^T})$ is the force as a function of normalized length, and F_0^M is the maximum

Stellenbosch University https://scholar.sun.ac.za

force exerted by the tendon.

Notably, there are identifiable shortcomings of this implementation, which will likely result in poor performance of this patella tendon variation. A primary concern is the fact that OpenSim does not incorporate a functionality which allows muscle activity to influence the translation and rotation mechanics of the patella bone during locomotion - whose translation and rotation during locomotion is determined based on knee flexion kinematics (see Figure A.5) (Arnold *et al.*, 2010). Consequently, the relative movement of the patella with respect to the tibia, and by extension tendon elongation, is constrained. Furthermore, the fact that OpenSim approximates ligament force purely as a function of the defined normalized force-length curve and instantaneous fibre length during locomotion, increases the likelihood of poor simulation results. Given that Arnold *et al.* (2010) and Schmitz and Piovesan (2016) have incorporated similar independent patella tendon variations in their respective models, and no evidence of poor performance was documented, this tendon variation will be investigated in this project.

Variation 2: Narrow Implicit Variation

As highlighted in Chapter 2, anatomically, the patella tendon is a continuation of the quadriceps tendon, with no definitive separation point. As a result, the second variation of the patella tendon models the tendon implicitly, through the continuation and wrapping of the quadriceps muscles (namely the rectus femoris, vastus lateralis, vastus medialis, and vastus intermedius muscles) over the patella and insertion into the tibia. Notably, the active paths of each of the involved quadriceps muscles are modelled along the same line of action between the patella and tibia, Figure 3.8. This variation of the patella tendon was adapted from the Rajagopal *et al.* (2016) "Full Body" model's implicit implementation of the tendon, where Rajagopal *et al.* (2016) modelled the quadriceps muscle paths between the patella and tibia along three separate lines of action instead of one.

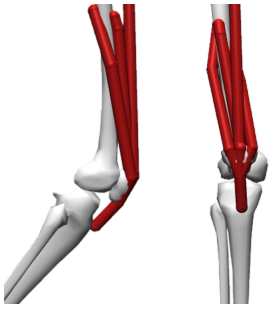

Figure 3.8: The narrow implicit implementation of the patella tendon via the wrapping of the quadriceps muscles over the patella. The quadriceps muscle fibres (red fibres) connect the hip and femur to the superior area of the patella, as in the single ligament fibre implementation. From the superior insertion points, the muscles extend and attach to the distal pole of the patella, and connect the patella to the tibial tuberosity via the a single active fibre path

Stellenbosch University https://scholar.sun.ac.za

Due to the extensive elongation and restriction of the four quadriceps muscle paths along the patella and tibia, the maximum isometric force, optimal fibre length, tendon slack length, and pennation angle of the muscles were adjusted to those used by Rajagopal *et al.* (2016), see Table A.4. Rajagopal *et al.* (2016) took the optimal fibre length and pennation angle properties directly from Ward *et al.* (2009), and computed the maximum isometric forces using Equation 3.1 and PCSA values from Handsfield *et al.* (2014). Furthermore, Rajagopal *et al.* (2016) determined the tendon slack lengths using a Monte-Carlo simulation with the same objective as Delp (1990) in Section 3.1.2.

Variation 3: Broad Implicit Variation

Oikawa *et al.* (2018) evaluated the morphology and insertion sites of the patella tendon in 32 cadavers (19 male and 13 female) using 3-dimensional (3D) computed tomography. Oikawa *et al.* (2018) found that the insertion sites of the patella tendon on the patella and tibia were V-shaped and crescent-shaped, with widths of 29.9 $\pm$ 2.7 mm and 25.0 $\pm$ 2.4 mm, respectively (Oikawa *et al.*, 2018).

The “Full Body” model developed by Rajagopal *et al.* (2016) exhibits similar patella tendon characteristics. As previously highlighted, Rajagopal *et al.* (2016) modelled the patella tendon implicitly through the continuation and wrapping of the quadriceps muscles over the patella and insertion into the tibia. Further, Rajagopal *et al.* (2016) utilized three separate active muscle fibre paths to connect the distal pole of the patella to the tibial tuberosity on the tibia. Consequently, the third patella tendon variation is adapted from the patella tendon implemented in the Rajagopal *et al.* (2016) model, Figure 3.9.

Due to the fact that this tendon variation incorporates the extensive elongation and restriction of the four quadriceps muscle paths along the patella and tibia as observed in the narrow implicit tendon model, the maximum isometric force, optimal fibre length, tendon slack length, and pennation angle of the quadriceps muscles were adjusted to those used by Rajagopal *et al.* (2016), see Table A.4.

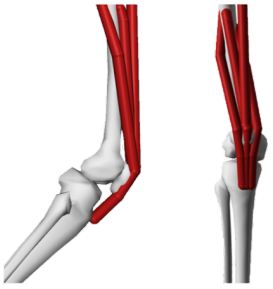

Figure 3.9: The broad implicit implementation of the patella tendon via the wrapping of the quadriceps muscles over the patella (Rajagopal *et al.*, 2016). The quadriceps muscle fibres (red fibres) connect the hip and femur to the superior area of the patella, as in the single ligament fibre implementation. From the superior insertion points, the muscles extend and attach to the distal area of the patella, and finally connect the patella to the tibial tuberosity via three muscle fibre paths

Stellenbosch University https://scholar.sun.ac.za

3.2.6 Achilles Tendon

The following section presents an alternative variation of the Achilles tendon implemented in the Hamner *et al.* (2010) model.

Variation 1: Curved Gastrocnemius Fibres

As in the Hamner *et al.* (2010) model, this variation of the Achilles tendon models the tendon as the cumulative tendon of the soleus and gastrocnemius muscles. However, unlike the generic model, the path of the gastrocnemius muscles are modified to wrap over a cylindrical wrapping surface located at the superior end of the tibia, Figure 3.10.

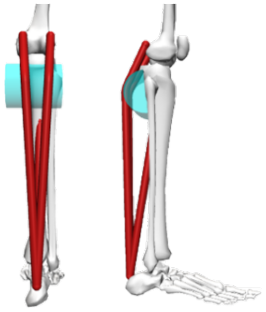

Figure 3.10: Illustration of the half-cylindrical wrapping surface used for the Achilles tendon variation. The wrapping surface, indicated in aqua, is located at the head/superior end of the tibia, and the respective muscle fibres (soleus, medial and lateral gastrocnemius fibres) are indicated in red

Similar wrapping surfaces have been implemented in other musculoskeletal models (Rajagopal *et al.*, 2016; Arnold *et al.*, 2010; Lai *et al.*, 2017) in order to incorporate the curvature of the calf muscles and hence improve the accuracy of the programmed fibre path. This variation of the Achilles tendon was adapted and implemented as a hybrid of the Rajagopal *et al.* (2016), Arnold *et al.* (2010), and Lai *et al.* (2017) model implementations. In each of the Rajagopal *et al.* (2016), Arnold *et al.* (2010), and Lai *et al.* (2017) model implementations, two wrapping surfaces were used: one at the posterior end of femoral condyles (preventing muscle-bone penetration), and the other at the head of the tibia (improving the accuracy of the gastrocnemius muscle paths). Arnold *et al.* (2010) utilized ellipsoidal shaped wrapping surfaces, where as Rajagopal *et al.* (2016) and Lai *et al.* (2017) utilized cylindrical wrapping surfaces.

For simplicity, and the fact that the bone geometry files and muscle insertion points utilized in the Hamner *et al.* (2010) model differ to those defined in the other models, the insertion points and muscle modelling parameters of the lateral and medial gastrocnemius muscle fibres were not altered from those in the generic model. Furthermore, a single cylindrical wrapping surface is used instead of two. A 40 mm radius cylindrical wrapping surface was utilized (Rajagopal *et al.*, 2016; Arnold *et al.*, 2010), and its placement was dependent on the location of the insertion points of the gastrocnemius muscles on the femoral condyles. Consequently, the wrapping surface was positioned

Stellenbosch University https://scholar.sun.ac.za

such that, at high angles of knee flexion, the muscle paths remain wrapped over the cylinder.

3.3 Developed Models

The above documented modifications resulted in the development of 6 modified musculoskeletal models, each with a unique combination of the patella and Achilles tendon variations. As previously mentioned, each of the modified models use the Hamner *et al.* (2010) model as its base, with only the above discussed modifications deviating from the base model's inherent traits.

The first modified model, Model 1, contains the single fibre implementation of the patella tendon, and the original Hamner *et al.* (2010) Achilles tendon implementation. Similarly, Model 2 and Model 3 contain the same Achilles tendon implementation as in Model 1, but contain the narrow and broad implicit implementations of the patella tendon, respectively. Models 4, 5, and 6 contain the same patella tendon implementations as Models 1, 2, and 3, respectively, but contain the modified Achilles tendon implementation instead of the original Hamner *et al.* (2010) Achilles tendon implementation. For the purpose of simplicity, Models 1, 2, and 3 are referred to as first tier models and Models 4, 5, and 6 as second tier models. Table 3.1 summarizes the combination of the patella and Achilles tendon variations realized in each of the developed models.

Table 3.1: Overview of the developed musculoskeletal models and the modified variations of the patella and Achilles tendons realized in them

	Patella Tendon Variations			
Achilles Tendon Variations	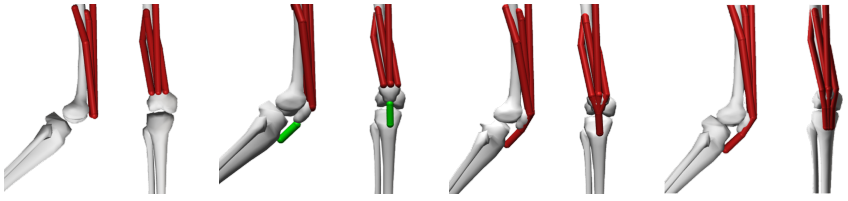			
	Hamner *et al.* (2010) model	Model 1	Model 2	Model 3
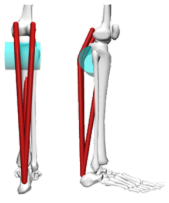		Model 4	Model 5	Model 6

Stellenbosch University https://scholar.sun.ac.za

4 Python Processing Pipeline

Traditionally, OpenSim gait analysis workflows are run through the OpenSim GUI. This style of use requires the user to manually input all of the required parameters to execute a particular tool in the OpenSim gait analysis workflow. Processing pipelines utilize non-traditional techniques, in particular API feeds, to run applications and execute a desired workflow. They offer users an automated, less tedious, and time efficient alternative to traditional use styles.

The following chapter documents and discusses the developed Python processing pipeline and the implemented workflow. All supplementary information for this chapter may be found in Appendix B.

4.1 Pipeline Objectives

In order to satisfy the second project objective, highlighted in Section 1.3, it is required that the pipeline addresses and satisfies the following points:

- Developed and automated using an open-source programming platform, in particular Python
- Incorporates OpenSim's gait analysis tools through the utilization of the OpenSim - Python API interface
- Performs batch processing of each of the user-selected participant(s) for the desired running trial(s)
- Issue warnings or error messages to the user when applicable - for example, when the resulting performance errors of an OpenSim tool falls outside the recommended error limits
- Processes and prints the gait analysis results once the analysis workflow has completed

4.2 Pipeline Workflow

Figure 4.1 illustrates an overview of the workflow implemented in the developed pipeline.

Stellenbosch University https://scholar.sun.ac.za

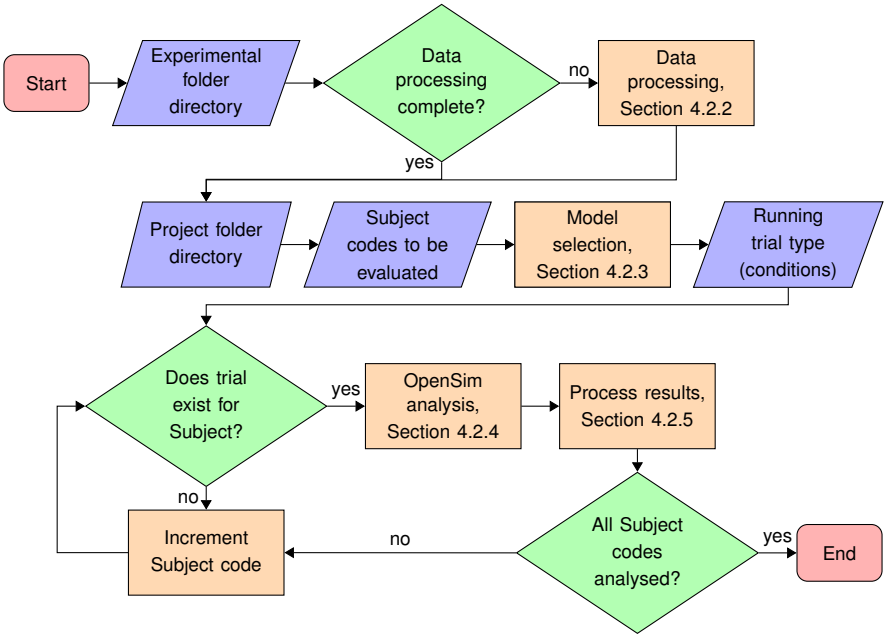

Figure 4.1: High-level overview of the developed Python processing pipeline

4.2.1 User Input Management

In order for this pipeline to function as a generalized solution, it is important that the input directory paths and files are modifiable according to the needs of the user. All user inputs are prompted via the main Python command console through which the pipeline is run. The pipeline incorporates a pop-up file dialog interface for the selection and specification of files and folder directories. The file dialog interface is generated using “tkinker”, a Python interface package. The folder structure requirements for the pipeline are outlined in Section B.1. Once the input parameters have been defined by the user, each of the inputs are checked to see if they are valid and are then stored as global variables. Consequently, the input parameters are accessible for use by all of the pipeline’s methods. As demonstrated in Figure 4.1, the pipeline requires the user to input five parameters, namely the:

1. Folder directory which contains the experimental data files
2. Project folder directory - the folder which contains the generic setup files, desired musculoskeletal model file(s), and pipeline results folder, refer to Figure B.1
3. Desired musculoskeletal model to be used, refer to Section 4.2.3
4. Participant/Subject codes to be evaluated during the analysis
5. Type of running conditions (level, incline, or decline) to be evaluated - the pipeline uses this information to organize and extract the respective STO, MOT, and TRC files from the experimental folder directory for the selected subject codes

Stellenbosch University https://scholar.sun.ac.za

Due to the fact that the first three inputs are either a file or folder input, these inputs are obtained via the “tkinker” file dialog interface, and the last two inputs via the command console. It is important to note that the progress of the processes conducted within the pipeline are also communicated to the pipeline’s user via the command console.

4.2.2 Data Processing

The first core process implemented in the pipeline is that of data processing. In this process, aspects involving the experimental environment, signal filtering, event detection, and the conversion of file types to those supported by OpenSim, are considered and addressed. The implemented data processing algorithm (Figure 4.2) utilizes the user defined folder directory containing the raw experimental data files, and comprises of two data processing stages: motion capture data processing, and EMG signal processing.

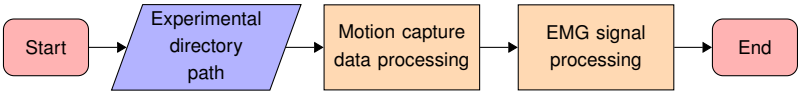

Figure 4.2: High-level workflow of the implemented data processing algorithm

Within the two implemented data processing stages, a generic three step approach to organizing and processing the data exists:

1. The relevant data and information from the experimental data files are extracted and read into a data structure within the Python environment.

   Marker trajectory and force plate data points are extracted from the C3D motion capture files and converted into time-series tables using the OpenSim API “C3DFileAdapter” functionality. A time-series table is an OpenSim data table where the independent data column represents time and the dependent data columns contain the X, Y, and Z vector components of marker trajectories or force plate data, respectively. Similarly, the muscle activation signals are extracted from a CSV file and read into a data frame using Python’s “pandas” library.

2. The extracted data from Step 1 undergoes signal processing.

   Signal processing plays an integral role in data processing, and can have a significant impact on the results from gait analysis tools (Atkinson, 2018). Section 4.2.2 and 4.2.2 document the specific signal processing techniques implemented for motion capture data and EMG signals, respectively.

3. The processed data structures from Step 2 are formatted and written to data files that are compatible with OpenSim.

   The output data files comprise of TRC and STO files containing marker trajectories, MOT and STO files containing force plate data, picture (PNG) files illustrating the filtered vertical GRF profiles, STO files containing processed EMG signals, and finally, two text (TXT) files containing optimal cut-off frequencies for noise filtering.

Stellenbosch University https://scholar.sun.ac.za

It is important to note that the author developed a unique data processing algorithm instead of utilizing existing biomechanics data processing systems, such as MOtoNMS (Mantoan *et al.*, 2015), as the existing systems are Matlab based. Furthermore, the author wished to incorporate the algorithm into the Python processing pipeline, with an option for use by the pipeline user.

Motion Capture Signal Processing

The signal processing techniques used for marker trajectories and force plate data incorporate numerous functionalities which address data rotation, noise filtering, and event detection. Figure 4.3 illustrates the implemented workflow for processing motion capture data.

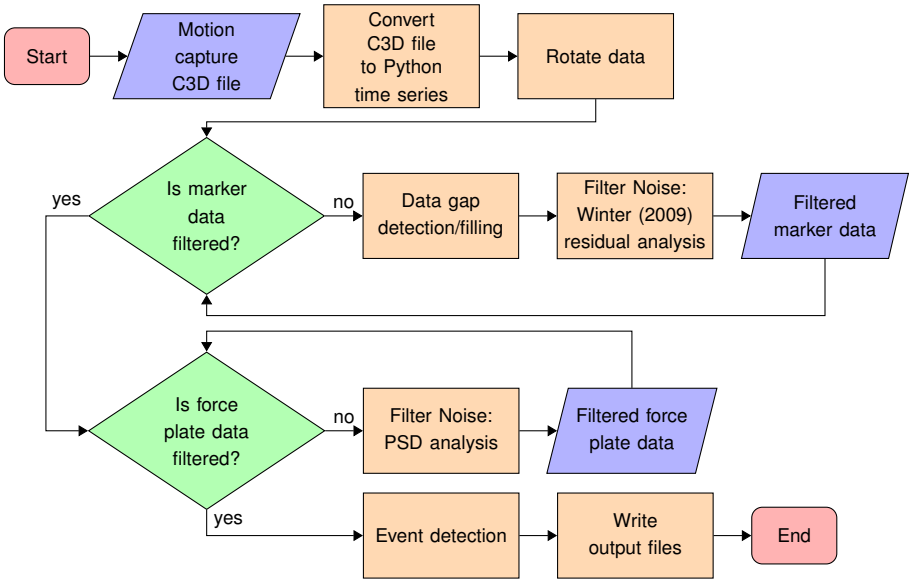

Figure 4.3: Flowchart of the implemented signal processing workflow for the processing of motion capture data in the developed pipeline

With reference to Figure 4.3, the first process of the signal processing functionality is that of data rotation. As discussed in Section 2.4.2, it is necessary to consider the relative orientation of the experimental laboratory's coordinate system to OpenSim's *in-silico* coordinate system. An Euler rotation transformation of the marker and force plate data sets is realized in the pipeline. It is required that both the axis and desired rotation angle should be defined. Due to the orientation of the laboratory's coordinate system in this particular project (X positive to the right, Y in the anterior direction, and Z in the inferior direction), a -90° rotation about the laboratory X and Y axes was required, and is set as the default rotation setting.

The second process implemented in the signal processing functionality is that of noise filtering. In this process marker trajectories and force plate data sets are filtered independently from one another. Research conducted by Roewer *et al.* (2014), Bisseling and Hof (2006), and Bezodis *et al.* (2013) have shown that during high impact activities,

Stellenbosch University https://scholar.sun.ac.za

such as sprinting and jumping, the filtering of marker trajectories and force plate data has a significant effect on simulated gait analysis results. It is for this reason that both the marker trajectories and force plate data profiles (GRFs, COPs, and moments) are filtered using fourth-order, zero-lag, low-pass, Butterworth filters.

The default cut-off frequency for marker trajectories is set as 20 Hz. This cut-off frequency was selected as the average optimal cut-off frequency, rounded to the nearest whole number, that was determined by the residual analysis method (Winter, 2009) for each marker trajectory. Figure B.7 illustrates the principle upon which the residual analysis method is based.

However, before the marker trajectories are filtered, the pipeline identifies if any marker trajectories have missing data values. Using Python's built-in "SciPy" library, a cubic interpolation is run on the marker trajectories to fill the detected data gaps. It is important to note that interpolation only takes place if the detected data gap is smaller than a defined threshold - a maximum allowed percentage of missing data per second. The default threshold is set as 20 % for a 200 Hz frame rate (Mantoan *et al.*, 2015).

The default cut-off frequency for force plate data filtering is set as 15 Hz. This cut-off frequency was selected based on the average of the optimal cut-off frequencies determined by the power spectral density (PSD) analysis method. Using the PSD method, the choice of cut-off frequency is taken as the frequency at which 95 % of the signal's power is contained (Sinclair *et al.*, 2013; Duarte, 2020). Additionally, vertical forces with magnitudes less than 20 N, as well as their corresponding force components, COPs, and moments, are zeroed to remove low frequency noise (Matijevich *et al.*, 2019). In both of the above data filtering cases, the user may choose to use the dataset-specific cut-off frequencies for marker and force processing over the default settings.

The third process implemented in the motion capture signal processing functionality is event detection. As previously mentioned, the "C3DFileAdapter" functionality provided by the OpenSim API is utilized to read the motion capture file's marker trajectory and force data tables into the Python environment. As a result, the gait events detected by the motion capture system, such as FS and TO, cannot be accessed or extracted. Hence it was necessary to develop a method which may determine these events using marker trajectories and GRF magnitudes.

The filtered foot marker trajectories (in particular the toe, calcaneus, lateral anterior and lateral posterior foot marker trajectories) and GRFs are utilized as a guide for the determination and validation of FS events detected by the implemented algorithm. The foot marker trajectories are used to determine a viable time period for when FS and TO may occur. In order to determine this time period, the foot marker locations are averaged and evaluated against a unique vertical height threshold. The default vertical height threshold is defined as 150 % of the minimum, averaged, vertical height of the foot markers above the ground. This threshold was determined through a process of trial and error, as it is an indicator of how far away the foot of a participant is from the minimum mean height of the foot marker during the running trial. If the determined time stamps correspond to increasing GRFs, the identified FS period is deemed valid.

Stellenbosch University https://scholar.sun.ac.za

During experimental running trials, it is common practice for the study participants to run on a single treadmill belt as it improves the comfort and stability of the runner. As a result, the captured force data for each foot is stored in a single set of data columns which correspond to the treadmill belt used. OpenSim requires that each foot's GRFs, COPs, and moments be represented in separate data columns. To separate the force plate data accordingly, within the validated FS and TO time stamps, the vertical height of the foot markers were compared. The foot markers (left or right) closest to the ground are then assigned to the corresponding increasing GRFs during that validated time period. Once the GRFs were assigned to its corresponding foot, the sequence of the identified FS and TO events are analysed to determine whether the identified events are sequential (identify if right TO is followed by left FS, and that left TO is followed by right FS), as is expected for running. In the output motion file, the right foot is stored in the first set of data columns, and the left in the second.

EMG Signal Processing

The purpose of EMG signal processing is to express the raw EMG signals, measured in volts, as a representation of muscle activation. Muscle activation is expressed as a number between 0 (no muscle contraction) and 1 (maximum muscle contraction). Additionally, the raw signal is smoothed and filtered to remove noise and signal elements not related to muscle activity. Figure 4.4 illustrates the signal filtering process followed for filtering EMG data signals and Figure 4.5 illustrates the flowchart of the implemented signal processing workflow for processing EMG data signals in the developed Python processing pipeline.

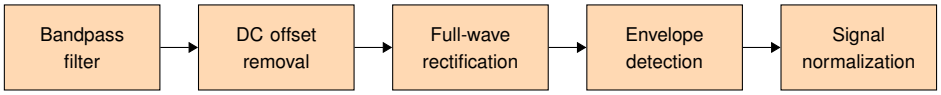

Figure 4.4: The implemented signal processing workflow for processing EMG signals

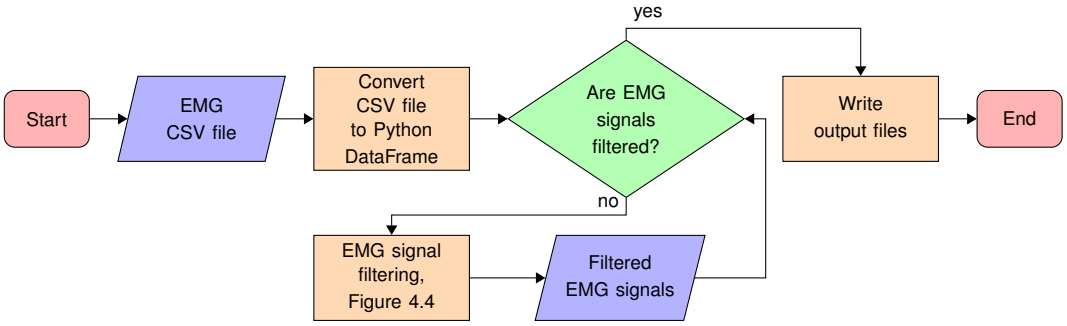

Figure 4.5: Flowchart of the implemented signal processing workflow for processing EMG data signals in the developed Python processing pipeline

First, the DC offset (mean) of the EMG signal is removed. This results in a data signal that is centered around zero. After the DC offset has been removed, the data signal undergoes an initial bandpass filtering process. The data signal then undergoes full wave

Stellenbosch University https://scholar.sun.ac.za

rectification and low-pass filtering (“linear envelope” detection). Finally, the rectified and filtered data signal is normalized against the maximum voltage reading for the muscle in the trial being processed (Rose, 2019).

For both the bandpass and low-pass filtering processes, fourth-order, zero-lag Butterworth filters are used. The lower and upper limit cut-off frequencies used in the bandpass filter are set as 5 Hz and 500 Hz, respectively. These cut-off frequencies are derived from the standards presented by the International Society of Electrophysiology and Kinesiology (ISEK). ISEK recommends that for surface EMG signals, a bandpass filter, with a lower cut-off of 5 Hz and upper cut-off of 500 Hz is sufficient (Rose, 2019; Merletti, 2015). Similarly, the selected cut-off frequency for the low-pass filter is set as 20 Hz (Rose, 2019).

4.2.3 Model Selection

The default model selected for the pipeline is the “Full Body Running” model (Hamner *et al.*, 2010). However, for versatility, the pipeline can accommodate other OpenSim models. To change the default model selection, the pipeline user is required to explicitly state the file path of the model they wish to use. The specified model is then utilized throughout the remainder of the pipeline’s workflow. For this study, the pipeline is used to analyse the Hamner *et al.* (2010) model and modified models discussed in Chapter 3.

4.2.4 OpenSim Gait Analysis

OpenSim gait analysis is the third process implemented in the processing pipeline, Figure 4.6. This functionality utilizes the specified musculoskeletal model and OpenSim API feed to programmatically write setup files and run the implemented gait analysis tools.

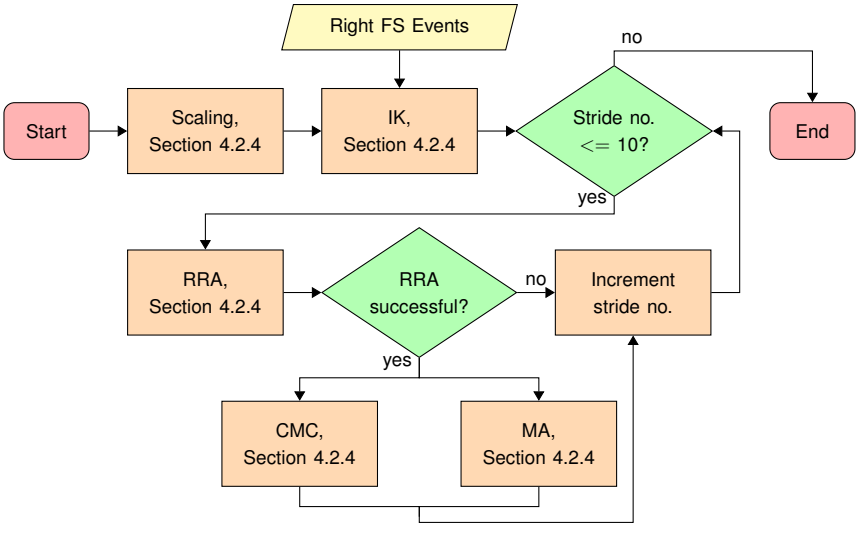

Figure 4.6: Flowchart of the OpenSim analysis workflow implemented in the developed Python processing pipeline

Stellenbosch University https://scholar.sun.ac.za

For this project, it is required that a reasonable time rage of the dynamic running trials are analysed. With reference to Figure 4.6, it is observed that 10 consecutive strides are analysed from a given running trial, where a stride is defined as the time period between two consecutive right FS events. The selection of 10 strides in particular is not only due to the fact that 10 strides accounts for a considerable portion of the captured running trials in this project, but is also common practice in the field of biomechanics (Groeneveld, 2020).

Figure 4.6 shows that Scaling and IK, unlike RRA, CMC, and MA, are implemented in a stand-alone fashion. This is due to the fact that model scaling is a static analysis process and does not form part of the dynamic gait analysis workflow. Further, the IK functionality has the ability to analyse all 10 strides in a single execution of the tool. Due to the sensitivity and time analysis limitations of the RRA, CMC, and MA optimization algorithms, they are conducted in a loop fashion where each of the 10 strides are analysed independently of one another.

The right FS events input block in Figure 4.6 feeds the time stamps of the 10 consecutive strides for the running trial to the dynamic gait analysis portion of the OpenSim workflow. The right FS event detection method evaluates the processed GRF file for the running trial being analysed. The method considers the start of a stride as the first non-zero force proceeding a zero force for the right foot (i.e. when the right FS occurs), and the end of a stride as the last zero force before the next right FS event.

The remainder of this section presents the manner in which the previously discussed OpenSim gait analysis tools are incorporated in the developed pipeline, refer to Section 2.4.2.

Scaling

As indicated by Figure 4.6, the first stage of the OpenSim gait analysis workflow is model scaling. During this stage, the selected musculoskeletal model is scaled to match the anthropometry and mass properties of the participant.

The implemented scale functionality takes two input files: a settings file for the scale tool, and a TRC file containing experimental marker locations for the subject's static calibration trial. Additionally, the subject's biological information (mass, height, and age) is processed.

Due to the limitations of the OpenSim API, the OpenSim scale tool cannot be implemented as a single process, but rather as three consecutive sub-processes: generic model maker, model scaler, and marker placement. These sub-processes address generic model definition, model scaling, and marker placement on the resulting scaled model, respectively. The model scaling process executes the first four steps of the scale tool highlighted in Section 2.4.2, and the final step is executed during marker placement.

In general, markers are grouped according to function, namely: anatomical and tracking markers. Anatomical markers are the markers placed on bony landmarks, and repre-

Stellenbosch University https://scholar.sun.ac.za

sent a high level of confidence. Tracking markers however, are the markers which are placed on the intermediate areas of body segments and work together with anatomical markers to increase tracking abilities during locomotion. Consequently, the level of confidence for the placement of tracking markers is significantly lower than for anatomical markers.

Kainz *et al.* (2017) investigated the reliability and accuracy of numerous musculoskeletal model scaling methods for the pelvis, thigh and shank of typically developed (TD) subjects, based on surface marker locations alone. Of the investigated methods, Kainz *et al.* (2017) concluded that the pelvic segment should be scaled independently along each axis according to width and height, and both the thigh and shank segments should be scaled uniformly along their longitudinal axes according to joint center marker locations (i.e. thigh: hip joint center (HJC) to knee joint center (KJC); shank: KJC to ankle joint center (AJC)).

Table 4.1 summarizes the measurement-based scale factor sets used to scale the defined musculoskeletal model in this pipeline. It is important to note that although Kainz *et al.* (2017) suggests that only the pelvic width and height should be considered, the implemented scaling method for the pelvis segment includes pelvic depth.

Table 4.1: Scaling marker pairs used to scaled the musculoskeletal model's rigid body segments

Scale Set	**Marker Pairs**	
Pelvis (X axis)	LPSI LASI	RPSI RASI
Pelvis (Y axis)	LPSI RPSI LHJC RHJC	LASI RASI
Pelvis (Z axis)	RPSI LPSI	RASI LASI
Thigh	LHJC LKJC	RHJC RKJC
Shank	LKJC LAJC	RKJC RAJC
Foot	LAJC LTOE	RAJC RTOE
Heel	LAJC LHEE	RAJC RHEE
Torso	LPSI C7 RPSI C7	LASI LSHO RASI RSHO
Humerus	LSHO LELB	RSHO RELB
Radius-Ulna	LELB LWRB	RELB RWRB

From Table 4.1 it is clear that only anatomical markers were used for the scaling process. In addition to body segment scaling, the unscaled model's mass and inertial properties are scaled using the scale factors resulting from the scale sets identified in Table 4.1, the subject's mass, and the activated PMD functionality. Consequently, the resulting scaled model's mass and height equal those of the subject.

Stellenbosch University https://scholar.sun.ac.za

Once the scale tool has been executed, the scaled subject-specific model and a file containing the model's static pose coordinate values are outputted, see Figure B.8 in Appendix B. Furthermore, the total squared, root mean squared (RMS), and maximum marker errors observed during the scaling process are recorded and printed to the console.

Inverse Kinematics

The second process in the gait analysis workflow is IK. As discussed in Section 2.4.2, the IK tool calculates the model's joint angles and marker translations which "best match" those observed during the testing procedure by solving the WLS problem.

The inputs for the IK functionality include the scaled subject-specific model from the scale functionality and a TRC file containing the marker trajectories for 10 consecutive strides of the dynamic running trial. Furthermore, the IK tracking weights of the markers for a given running trial are derived from those used in the dynamic simulation conducted by Hamner *et al.* (2010), and emphasize tracking the lower extremities joint angles with a high degree of confidence.

Once the IK functionality is complete, a STO file containing the marker errors for each time step in the analysis, as well as a MOT file containing the model's dynamic joint angle values for the trial duration are printed. Additionally, the IK error results are analysed. The OpenSim user guide recommendeds that the RMS marker error of IK process should be less than 4 cm (Simtk-confluence.stanford.edu, 2020). If the determined RMS error for the trial surpasses this bound, the pipeline user is notified via a error message in the console and has the option to continue or restart the IK process. Refer to Figure B.9 in Appendix B.

Residual Reduction Algorithm

The third process conducted in the implemented gait analysis workflow is that of RRA. As mentioned in Section 2.4.2, the main objective of the RRA process is to obtain a dynamically consistent model with respect to experimental GRFs and kinematics.

The inputs for the RRA functionality include the scaled musculoskeletal model, the resulting kinematics file from the IK process, an external loads file containing the GRFs for the running trial, and two additional settings files which contain the task set and model actuators for the RRA process, respectively.

The task set settings file defines the tracking weightings for the model's joint angles during locomotion, and consequently allow joints with higher weightings to be tracked with a greater degree of accuracy. For this study, the tracking weights used were derived from those demonstrated by Hamner *et al.* (2010), with tracking emphasis placed on the pelvic, hip, knee, and ankle joints.

Similarly, the model actuators settings file contains the ideal force and torque actuators for each DOF present in the model. It is important to note that six residual actuators

Stellenbosch University https://scholar.sun.ac.za

(three force and three torque) are applied to the COM of the scaled pelvis, and are used to compensate for dynamic inconsistencies during locomotion - i.e. $\boldsymbol{F}_{res}$ in Equation 2.4. The optimal force and torque values for each of the defined actuators are engineered such that they are small (optimal forces and torques are set to 1 N and 1 Nm, respectively), consequently preventing the RRA optimizer from "wanting to use" the residual actuators, and thus achieve reliable actuation results from the analysis.

Once the RRA process has completed, numerous files which contain the model's states, kinematics, and actuation results are outputted. Additionally, a mass-adjusted model and a CSV file summarizing the reliability of the RRA analysis results, are also outputted. Refer to Figure B.10 in Appendix B.

It is important to note that the outputted mass-adjusted model realizes the mass recommendations made by the RRA tool. The suggested mass changes are realized for each of the recommended body segments and are modified through the use of the OpenSim Model class. Furthermore, the RRA tool's "body COM adjustment" setting is used to modify the COM of the torso body segment of the new adjusted model, resulting in a mass distribution scheme that is consistent with the mass changes made.

Similarly, the CSV summary file is written via a method developed by the author. The method considers the residual force and torque values, as well as the translational and rotational errors observed in the RRA results files, and compares the observations to the threshold values recommended by OpenSim. Table 4.2 summarizes the recommended threshold values and their corresponding performance categories ("good", "okay", and "bad") for a 75 kg subject, used to evaluate RRA results for full-body simulations of walking and running. Due to the fact that the force and torque residuals provided by OpenSim are specific for a 75 kg subject, their threshold values are presented as a percentage of subject body weight (BW).

Table 4.2: The recommended error threshold values used to evaluate RRA results for full-body simulations of walking and running, as provided by OpenSim (Simtk-confluence.stanford.edu, 2020)

		Error Performance		
Error Parameter	**Unit**	**Good**	**Okay**	**Bad**
Maximum residual force	% BW	0 - 1.36	1.36 - 3.4	$>$ 3.4
RMS residual force	% BW	0 - 0.68	0.68 - 1.36	$>$ 1.36
Maximum residual moment	% BW	0 - 6.8	6.8 - 10.2	$>$ 10.2
RMS residual moment	% BW	0 - 4.08	4.08 - 6.8	$>$ 6.8
Maximum translation error	cm	0 - 2	3 - 5	$>$ 5
RMS translation error	cm	0 - 2	3 - 4	$>$ 4
Maximum rotational error	degrees	0 - 2	3 - 5	$>$ 5
RMS rotational error	degrees	0 - 2	3 - 5	$>$ 5

Stellenbosch University https://scholar.sun.ac.za

In its totality, the summary file documents the maximum RMS and actual error values for the residual force and torque results incurred during the RRA process. Additionally, the summary file documents the maximum RMS and actual error values for both the translational and rotational DOF of the model. These translational and rotational DOF of the model are grouped according to location, namely upper, lumbar, pelvic, and lower extremities. The summary file further indicates the error performance group based on the magnitude of the observed errors.

OpenSim recommends that RRA should be conducted as an iterative process, where the RRA process should be terminated only once the total recommended mass change of the model is less than or equal to 1 kg and/or the number of "bad" result groups are one or less (Simtk-confluence.stanford.edu, 2020). Consequently, the implemented RRA process is only deemed to have been successfully completed once both of the above mentioned termination criteria are met. Figure 4.6 illustrates this criteria as the RRA functionality's proceeding processes (CMC and MA) are only conducted once the RRA functionality is deemed successful.

In the event that the RRA optimization algorithm successfully solves for the dynamic analysis of a given stride but one or none of the above mentioned termination criteria are met, the pipeline will re-conduct the RRA process with the mass-adjusted model and a modified task set settings file as inputs. The pipeline is configured such that a maximum of 10 iterations of the RRA functionality may be executed before the process is aborted.

The modified task set settings file is generated via a method which considers the information stored in the summary CSV file. The tracking weights of the model's upper, lumbar, pelvic, and lower extremities are modified based on each of the extremities corresponding error performance group. If the performance group for a given body segment group is "bad", the tracking weights for those coordinates are increased by a factor of 10. Similarly, if the performance group for a given body segment group is "good", to reduce the computational costs incurred by the RRA optimization algorithm, the tracking weights for those coordinates are decreased by a factor of 10, or until the modified tracking weight is of a single order of magnitude. If the error performance group is "okay", the tracking weights for those coordinates are kept constant.

Computed Muscle Control

CMC is the fourth process conducted in the implemented OpenSim workflow. As discussed in Section 2.4.2, the CMC tool computes the muscle excitations that drive a subject-specific model such that the calculated excitations achieve the desired kinematic set.

The RRA functionality's mass-adjusted model and kinematic results are both used as inputs in the implemented CMC functionality. Additionally, the CMC process requires an external loads file which contains the GRFs for the specific running trial, as well as three settings files which describe the task sets, actuators, and control constraints for

Stellenbosch University https://scholar.sun.ac.za

the dynamic simulation.

The task set settings file is similar to that seen in the RRA functionality and describes which of the model's joint angles should be tracked, and to what degree of confidence (i.e. tracking weights). Similarly, the CMC actuators settings files performs the same function as the RRA's actuators settings file, as they both contain the ideal force and torque actuators for every DOF in the model. In this pipeline, the same task set and actuators files used in RRA are used by the CMC functionality.

The control constraints settings file is unique and only used by the CMC tool. The file describes each of the model's actuators, where each actuator has a minimum and maximum excitation value. These excitation values allows the CMC optimization algorithm to ensure that the excitation values experienced during the simulation are valid for the specific actuator. For the model's muscle actuators, the default minimum excitation value is set as 0.02, and the maximum as 1 - this corresponds with the EMG activation range discussed in Section 4.2.2.

Additionally, the control constraints file allows for specific actuators to be turned "on" or "off" at different periods during the analysis. In this project, the medial and lateral gastrocnemius muscle excitations were "turned off" (set to the minimum muscle activation level, $a = 0.02$ % (Thelen, 2003)) during early to mid swing. This was done such that the resulting muscle excitation curves better matched those of the experimental EMG signals, and has been recommended in literature (Rajagopal *et al.*, 2016; Hamner *et al.*, 2010). Consequently, the numerical stability of the simulation is improved as the likelihood of unrealistic interactions between the gastrocnemius muscles and other muscles during the gait analysis period is mitigated (Rajagopal *et al.*, 2016).

Once the CMC process has completed, numerous files which contain the model's states, kinematics, actuation, and controls results are outputted. Additionally, a CSV file summarizing the reliability of the CMC analysis results, is also outputted. Refer to Figure B.12 in Appendix B. It is important to note that the CSV summary file is written using a similar method to that used for generating the RRA results summary file. Table 4.3 summarizes the recommended threshold values and their corresponding performance categories ("good", "okay", and "bad") used to evaluate CMC results for full-body simulations of walking and running.

Table 4.3: The recommended error threshold values used to evaluate CMC results for full-body simulations of walking and running, as provided by OpenSim (Simtk-confluence.stanford.edu, 2020)

		Error Performance		
Error Parameter	**Unit**	**Good**	**Okay**	**Bad**
Maximum residual force	% BW	0 - 1.36	1.36 - 3.4	$>$ 3.4
RMS residual force	% BW	0 - 1.36	1.36 - 3.4	$>$ 3.4
Maximum residual moment	% BW	0 - 6.8	6.8 - 10.2	$>$ 10.2

Stellenbosch University https://scholar.sun.ac.za

Error Parameter	Unit	Error Performance		
		Good	Okay	Bad
RMS reserve moment error	% BW	0 - 1.36	1.36 - 3.4	$>$ 3.4
Maximum translation error	cm	0 - 1	1 - 2	$>$ 2
RMS translation error	cm	0 - 1	1 - 2	$>$ 2
Maximum rotational error	degrees	0 - 2	3 - 5	$>$ 5
RMS rotational error	degrees	0 - 2	3 - 5	$>$ 5

Figure 4.6 illustrates that CMC and MA are conducted concurrently. This is achieved by importing the basic settings of a MA process to the setup file of CMC tool. Refer to Section 4.2.4, for details regarding the settings used for the MA process.

Analysis Toolbox: Muscle Analysis

As mentioned in Section 2.4.2, analysis tools, such as the MA tool, can be concurrently with other simulation processes such as RRA and CMC. In the developed pipeline, MA is run concurrently with CMC and forms part of the fourth process in the OpenSim gait analysis workflow.

The specific MA settings required for MA to be run concurrently with CMC includes the definition of a valid analysis time period, a list of the muscles to be included in the analysis, a list of the generalized coordinates for which the muscle moment arms are to be computed, and lastly the activation or deactivation of the moment calculation functionality for the model's muscles. The start and end analysis time stamps for MA are defined as the same start and end time limits used for CMC and RRA - i.e. the duration of one stride. In this pipeline the default MA settings state that all of the model's muscles are to be included in the MA analysis, with specific focus on the muscles which actuate lumbar bending, extension, and rotation, hip flexion, adduction, and rotation, knee flexion, and ankle plantar flexion. For these emphasized muscles, both the moment arms and moment contribution calculation functionalities are activated.

The output files of the MA process include three STO files which contain the tendon forces, muscle moment arms, and muscle moments. Refer to Figure B.11 in Appendix B.

4.2.5 Result Processing

Result processing is the final stage implemented in the developed processing pipeline, Figure 4.7. The aim of the result processing functionality is to present the pipeline user with a simplified means of visualizing the obtained results, as well as allows the user to access the results from standard CSV files, rather than complex STO and MOT files.

Stellenbosch University https://scholar.sun.ac.za

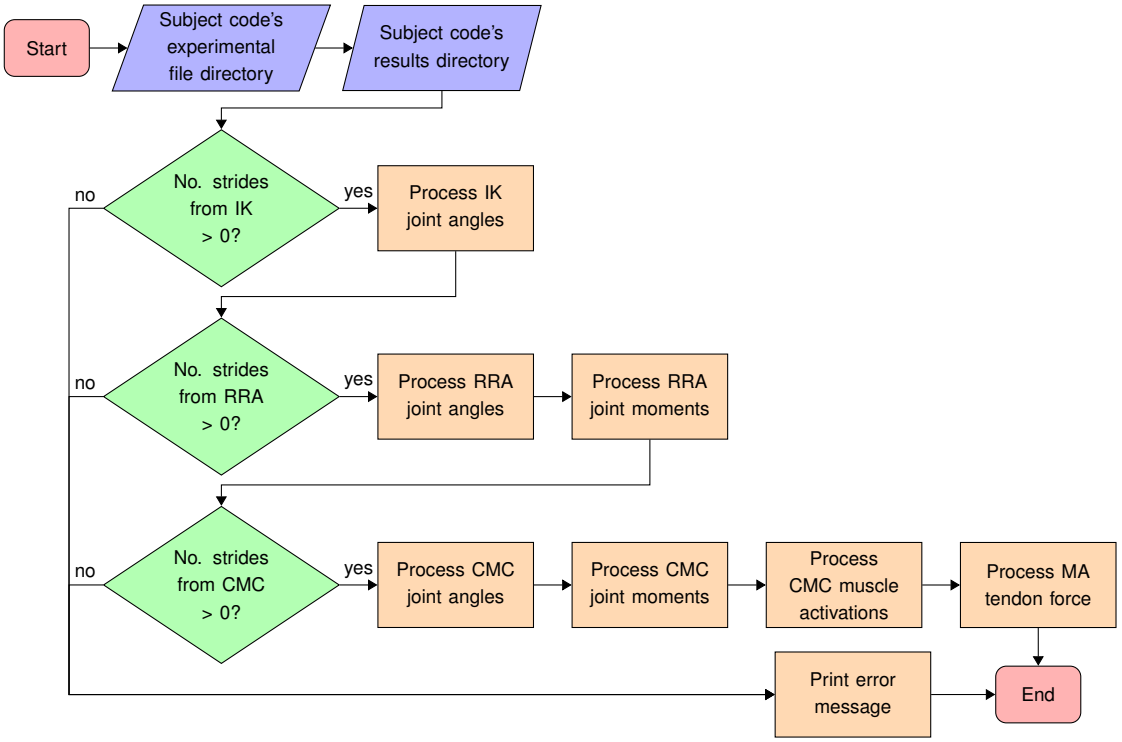

Figure 4.7: Flowchart of the implemented results processing workflow

The functionality outputs five different types of plots. The first two output plots illustrate the kinematic (joint angle) results from each of the dynamic analysis stages, namely: IK and RRA, and RRA and CMC. The third plot illustrates the actuation (joint moment) results obtained from the RRA and CMC processes. The fourth plot illustrates the CMC computed muscle activation signals against the experimental EMG activation signals for the running trial. The final plot indicates the tendon force curves for the Achilles and patella tendons, respectively.

In addition to the five different output plots, the functionality prints numerous CSV files which contain the mean and standard deviation curves for each of the kinematic, joint moment, muscle activation, and tendon force results obtained for all of the analysed running strides.

From Figure 4.7 it is clear that the pipeline's results processing functionality processes the OpenSim gait analysis results in three stages: IK, RRA, and CMC. In the event that either the IK, RRA or CMC tools do not successfully complete the analysis process for the initial 10 consecutive strides, an error message is printed to the Python console - stating which stride(s) have failed, the specific tool that failed, as well as the number of "bad" results for the respective stride(s) analysis. Section B.4 in Appendix B contains examples of the output plots generated by the results processing functionality.

Stellenbosch University https://scholar.sun.ac.za

5 Results

5.1 OpenSim Results

One of the principle objectives of this project is to develop an automated processing pipeline which may be applied to a range of different participants, running conditions, and musculoskeletal models. The following section presents the results obtained from the OpenSim running analysis workflow implemented in the processing pipeline.

Given that the project has a large study population (7 models, 5 participants, and 3 running conditions), it is important to note that only two of the seven investigated musculoskeletal models, in particular the "Full Body Running" model (Hamner *et al.*, 2010) and the third modified model (Model 3), will be discussed in this section. Furthermore, the presented OpenSim results focus on the project participants whose simulation results represent the entire OpenSim workflow for the analysed running conditions. Consequently, for level running conditions, results from Participants 1, 2, 3, and 5 are presented. Similarly, for the incline and decline running conditions, results from Participants 1, 2, and 5, and Participants 2, 3, and 5 are presented, respectively. Notably, the modified models (Models 1 - 6) achieved fewer complete simulations for the incline and decline running conditions than the baseline model. It is theorized that this is due to the generic default analysis settings and constraints used throughout the pipeline. All supplementary information for this section is documented in Appendix C.

5.1.1 Scaling

Scaling is arguably the most crucial process in the developed pipeline's workflow, as it generates the subject-specific model used throughout the analysis process. The OpenSim user guide (Simtk-confluence.stanford.edu, 2020) recommends that the RMS and maximum marker errors observed for anatomical markers should be less than 1 cm and 2 cm, respectively. Table 5.1 presents the total squared, RMS and maximum marker errors calculated by OpenSim during the scaling process for each participant.

Table 5.1: Musculoskeletal model scaling errors calculated in OpenSim

Participant	Total squared error (cm)	RMS (cm)	Maximum Anatomical Error (cm) [Marker]	Overall Maximum Error (cm) [Marker]
1	3.38	3.02	2.75 [RSHO]	5.62 [LTOE]
2	4.16	3.31	1.2 [LSHO]	7.49 [RUPA]
3	5.42	3.78	2.14 [RELB]	7.26 [LTHP]
4	5.83	3.92	2.03 [C7]	8.84 [LSHD]
5	4.96	3.61	2.78 [LWRB]	7.04 [LTHP]

Stellenbosch University https://scholar.sun.ac.za

Due to the fact that the generic placement locations of the virtual markers remained consistent across the investigated models and that the same static calibration file for each of the respective participants were used, the scale tool yielded identical scaling errors for all of the investigated models in this project. Consequently, the scaling errors communicated in Table 5.1, are applicable for all of the investigated models.

Table 5.1 shows that the overall maximum marker errors acquired during the scaling process are only observed for tracking markers, with the largest maximum error observed for Participant 4's left shin (LSHD) marker. Additionally, Table 5.1 shows that the maximum anatomical marker errors are only observed for upper body markers, and have errors less than 2.8 cm. The largest anatomical marker error was observed for the left inferior wrist (LWRB) marker of Participant 5. Notably, all of the RMS marker errors calculated by OpenSim are less than 4 cm. Due to the fact that the pipeline utilizes a generalized approach to scaling models and aims to provide a time efficient solution with reduced user intervention, these results may be considered as acceptable as they do not yield significant anatomical marker errors. Additionally, the observed RMS marker errors are relatively consistent for all of the project participants.

5.1.2 Inverse Kinematics

After a scaled subject-specific musculoskeletal model is realized, the pipeline determines the subject-specific, experimental kinematics (joint angles) observed during the analysed running trial. Figures 5.1 to 5.3 illustrate the IK results observed for the Hamner *et al.* (2010) model during level, incline, and decline running conditions. Each figure illustrates the mean joint coordinate angle observed during the running gait cycle (solid line), as well as indicates the single standard deviation (1 SD) clouds (shaded area). TO events for the respective participants are indicated by means of the vertical dotted lines.

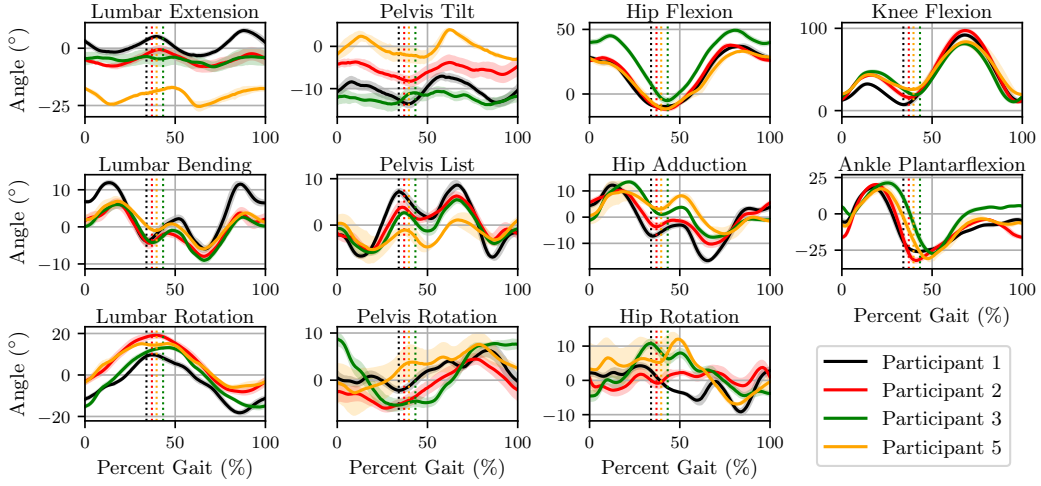

Figure 5.1: Hamner *et al.* (2010) model IK results for level running conditions

Stellenbosch University https://scholar.sun.ac.za

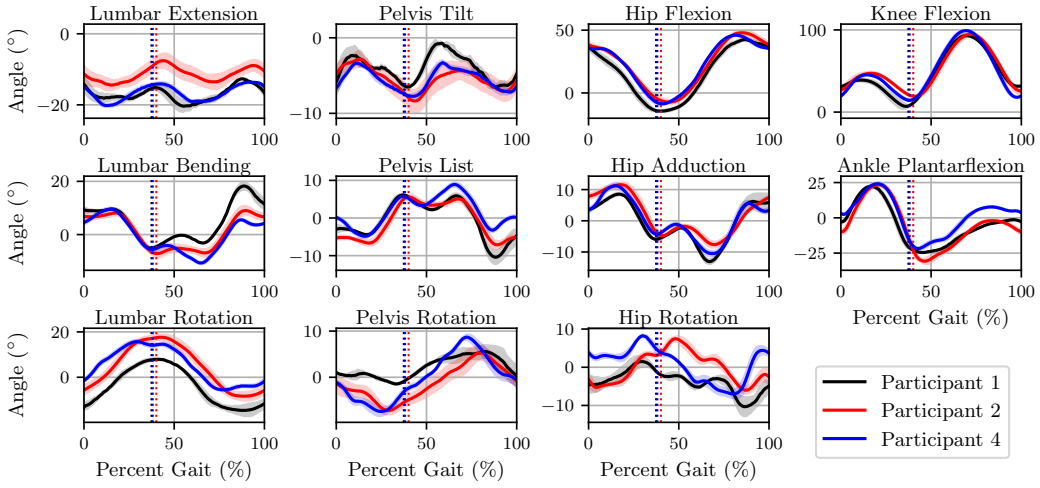

Figure 5.2: Hamner *et al.* (2010) model IK results for incline running conditions

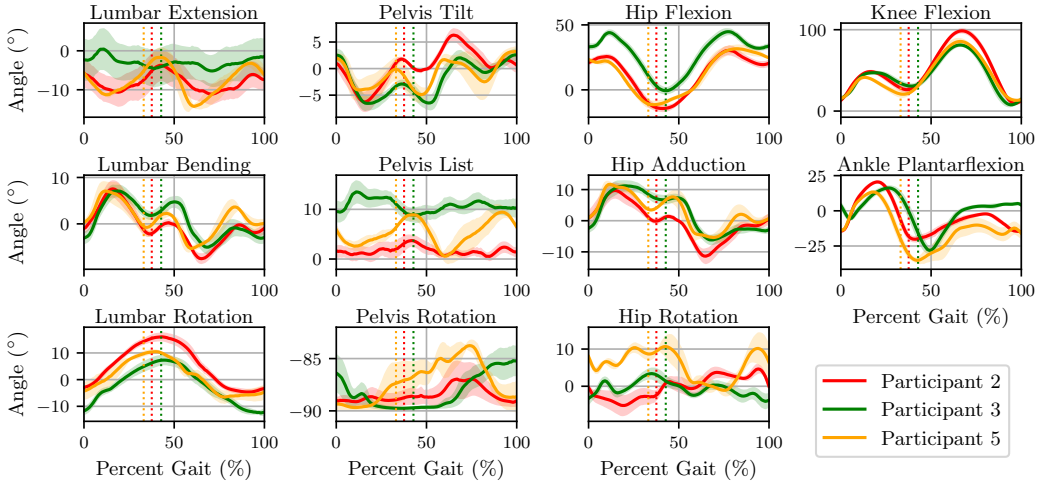

Figure 5.3: Hamner *et al.* (2010) model IK results for decline running conditions

For this project the hip, knee, and ankle joints are of special interest, as these joints make up the lower extremity kinetic chain (Palmitier *et al.*, 1991). Consequently, the kinematics of these joints are sensitive to any model assumptions and simplifications. Notably, the kinematics profiles for the hip, knee, and ankle joints display minimal variation across analysed running conditions. These findings are consistent with those documented by Telhan *et al.* (2010), who investigated the effect of moderately sloped running surfaces on lower limb joint kinetics. Additionally, the figures indicate that the participant-specific lumbar and pelvic kinematic profiles display the most variability in joint angle across the analysed running conditions. Notably, the pelvic rotation kinematic results during decline running conditions differ considerably when compared to those observed during level and incline running conditions. In a study conducted by Whittle *et al.* (2000), it was concluded that these kinematic deviations are present as

Stellenbosch University https://scholar.sun.ac.za

they are a direct result of the influence of running surface slope on running gait.

In general, the OpenSim user guide recommends that the total RMS marker error for the IK process should be less than 4 cm, where RMS errors below 2 cm are the most desirable (Simtk-confluence.stanford.edu, 2020). In addition to the RMS marker errors obtained by IK, to compare the performance of the modified models in relation to the baseline model, an average of the linear regression coefficients of determination (COD) observed for the hip, knee, and ankle joint angles, were computed - where the Hamner *et al.* (2010) model's kinematic results are considered as the datum data set for the COD evaluation ($R^2 = 1.0$). Table 5.2 summarizes the IK RMS errors and mean coefficients of determination (COD) observed for the hip, knee, and ankle joint angles of the baseline (Hamner *et al.*, 2010) and third modified model (Model 3) during level, incline, and decline running.

Table 5.2: RMS errors and mean coefficient of determination (R^2), acquired during the IK process for the Hamner *et al.* (2010) and third modified models during level, incline, and decline running conditions

		Level		**Incline**		**Decline**	
Model	**Participant**	**IK RMS (cm)**	R^2	**IK RMS (cm)**	R^2	**IK RMS (cm)**	R^2
Hamner *et al.* (2010) model	1	1.69	1.00	2.25	1.00		
	2	1.62	1.00	1.72	1.00	1.73	1.00
	3	2.14	1.00			2.21	1.00
	4			2.31	1.00		
	5	1.86	1.00			1.72	1.00
Model 3	1	1.76	0.97				
	2	1.63	0.9	1.68	0.99	1.75	0.98
	3	2.22	0.99			2.27	0.95
	4						
	5	1.84	0.96				

* R^2 is calculated in terms of the Hamner *et al.* (2010) model ($R^2_{baseline} = 1.0$)

** Blank table cells indicate no available data for the respective project participant and running condition, as the processing pipeline failed to successfully complete the entire OpenSim running gait analysis workflow implemented

From Table 5.2, it can be concluded that for each of the analysed running conditions, the IK results for Model 3 are similar to those of the Hamner *et al.* (2010) model. This conclusion is supported by the fact that the smallest mean COD (R^2) values observed for level, incline and decline running conditions in Table 5.2 are 0.9, 0.99, and 0.95, respectively. Furthermore, all of the RMS marker errors are less than the recommended error threshold of 4 cm, with the largest RMS error observed for Participant 4 during

Stellenbosch University https://scholar.sun.ac.za

incline running (RMS $=$ 2.31 cm). In general, Model 3 yielded marginally larger RMS error values than the baseline model and deviated by a maximum of 0.1 cm.

5.1.3 Residual Reduction Analysis

The third process implemented in the pipeline is RRA, where RRA aims to realize a modified subject-specific model that is dynamically consistent with the observed IK kinematic profiles and GRF data. Based on the termination criteria for RRA, discussed in Section 2.4.2, an important aspect to consider is how "active" residual forces and torques are during the RRA process. In general it is desired that the resulting residual forces and torques are small in relation to subject BW. The maximum X, Y, and Z residual force and torque components observed during level, incline, and decline running conditions, are tabulated in Tables 5.3 to 5.5. In the proceeding tables the "good", "okay", and "bad" error performance categories described in Table 4.2, and are represented by green, yellow, and red cell colours respectively.

Table 5.3: Maximum X, Y, and Z components of the residual forces and torques observed during RRA for level running

Model	**Participant**	**Residuals (% BW)**					
		F_X	F_Y	F_Z	M_X	M_Y	M_Z
Hamner *et al.* (2010) model	1	0.59	0.06	0.22	1.29	3.77	2.59
	2	0.25	0.04	0.09	0.81	2.73	2.31
	3	0.03	0.02	0.05	1.02	0.88	0.44
	5	0.24	0.72	0.08	1.49	1.55	0.71
Model 3	1	0.7	0.22	0.23	2.38	4.21	3.62
	2	0.45	0.11	0.14	1.67	3.69	2.43
	3	0.02	0.03	0.05	0.69	0.85	0.32
	5	0.2	2.32	0.03	0.38	2.46	0.32

Table 5.4: The maximum X, Y, and Z component values of the residual forces and torques observed during RRA for incline running

Model	**Participant**	**Residuals (% BW)**					
		F_X	F_Y	F_Z	M_X	M_Y	M_Z
Hamner *et al.* (2010) model	1	0.12	0.04	0.14	1.82	2.65	0.32
	2	0.01	0.04	0.19	1.32	2.54	0.42
	4	0.01	0.01	0.06	2.07	0.92	0.4
Model 3	2	0.04	0.14	0.33	2.68	3.79	1.99

Stellenbosch University https://scholar.sun.ac.za

Table 5.5: The maximum X, Y, and Z component values of the residual forces and torques observed during RRA for decline running

Model	Participant	Residuals (% BW)					
		F_X	F_Y	F_Z	M_X	M_Y	M_Z
Hamner *et al.* (2010) model	2	0.01	0.02	0.12	0.54	1.55	0.34
	3	0.1	0.24	0.27	4.21	3.55	1.61
	5	0.01	0	0.06	0.36	1.48	0.37
Model 3	2	0.06	0.01	0.24	0.33	2.09	0.14
	3	0.04	0.01	0.03	0.56	2.76	1.38

From the above tables it is clear that both the selected baseline model (Hamner *et al.*, 2010) and Model 3 have minimal residual force and torque activity during the RRA process, with most residual components representing a "good" error performance. One exception however is the "okay" vertical residual force component observed for Participant 5 during level running ($F_Y = 2.32$ % BW). This residual force overshoots the "good" error performance threshold by almost 1 % BW. Additionally, it is important to note that on numerous occasions Model 3 produced smaller force and torque residuals than those of the "Full Body Running" model (Hamner *et al.*, 2010). An example of this is seen during decline running for Participant 3, where Model 3 displays a significantly smaller X, Y, and Z torque residual components than those observed for the baseline model.

5.1.4 Computed Muscle Control

CMC is one of the final gait analysis functionalities implemented in the pipeline, and aims to estimate subject muscle activity during running. As discussed in Section 2.4.2, the residual forces and torques produced by CMC are evaluated in the same manner as in RRA. Tables 5.6 to 5.8 summarize the maximum X, Y, and Z residual force and torque components produced by CMC during level, incline, and decline running conditions. The "good", "okay", and "bad" error performance categories described in Table 4.3, and are represented by green, yellow, and red cell colours respectively.

Table 5.6: The maximum X, Y, and Z component values of the residual forces and torques observed during CMC for level running

Model	Participant	Residuals (% BW)					
		F_X	F_Y	F_Z	M_X	M_Y	M_Z
Hamner *et al.* (2010) model	1	1.64	2.73	2.22	1.68	3.58	4.34
	2	0.59	2.03	1.54	0.83	2.4	2.4
	3	5.97	0.93	2.2	2.97	1.08	0.43
	5	0.97	0.1	1.36	1.93	2.33	0.76

Stellenbosch University https://scholar.sun.ac.za

Model	Participant	Residuals (% BW)					
		F_X	F_Y	F_Z	M_X	M_Y	M_Z
Model 3	1	1.53	1.4	1.28	1.61	3.64	4.35
	2	0.88	1.16	2.08	1.35	3.27	2.78
	3	0.62	0.24	1.31	1.16	0.7	0.57
	5	0.57	2.94	2.12	1.81	1.61	0.62

Table 5.7: The maximum X, Y, and Z component values of the residual forces and torques observed during CMC for incline running

Model	Participant	Residuals (% BW)					
		F_X	F_Y	F_Z	M_X	M_Y	M_Z
Hamner *et al.* (2010) model	1	1.49	1.12	4.59	2.01	1.95	1.31
	2	0.77	1.92	1.42	1.49	2.31	0.9
	4	5.96	0.43	4.19	2.67	0.82	0.54
Model 3	2	0.93	1.27	2.18	2.57	3.34	3.04

Table 5.8: The maximum X, Y, and Z component values of the residual forces and torques observed during CMC for decline running

Model	Participant	Residuals (% BW)					
		F_X	F_Y	F_Z	M_X	M_Y	M_Z
Hamner *et al.* (2010) model	2	1.79	11.9	1.63	0.74	1.55	1.04
	3	1.8	0.42	3.38	3.06	2.53	1.84
	5	1.72	4.09	0.96	1.22	1.42	0.49
Model 3	2	3.29	12.3	1.65	1.39	1.91	1.18
	3	2.17	0.63	5.05	4.41	3.04	1.76

Tables 5.6 to 5.8 show that both the baseline model and Model 3 experience minimal residual torque activity during CMC, as all of the residual torque components fall within the “good” error performance bounds. In general, the residual torque components observed for Model 3 during level running are equivalent to those observed for the Hamner *et al.* (2010) model. However, for incline and decline running conditions, the observed residual torque values were larger than those for the Hamner *et al.* (2010) model.

A notable attribute of Model 3, in comparison to the generic model, is the reduced residual force components achieved during level and incline running conditions. In the case

Stellenbosch University https://scholar.sun.ac.za

of level running conditions, Model 3 produced no “bad” force residuals, and further reduced the number of “okay” force residuals observed for the baseline model. However, in the case of decline running, Model 3 produced force residuals that were significantly larger than those of the baseline model, with only one “good” residual force component (F_Y = 0.63 % BW).

5.1.5 Kinematics Comparison

As discussed in Chapter 4, the RRA functionality is configured such that it tracks the IK tool’s results. Similarly, the CMC tool is configured such that it tracks the resultant kinematics from RRA. To determine how well the RRA and CMC functionalities track their desired kinematic data sets, their resulting kinematic profiles are compared (Figure 5.4).

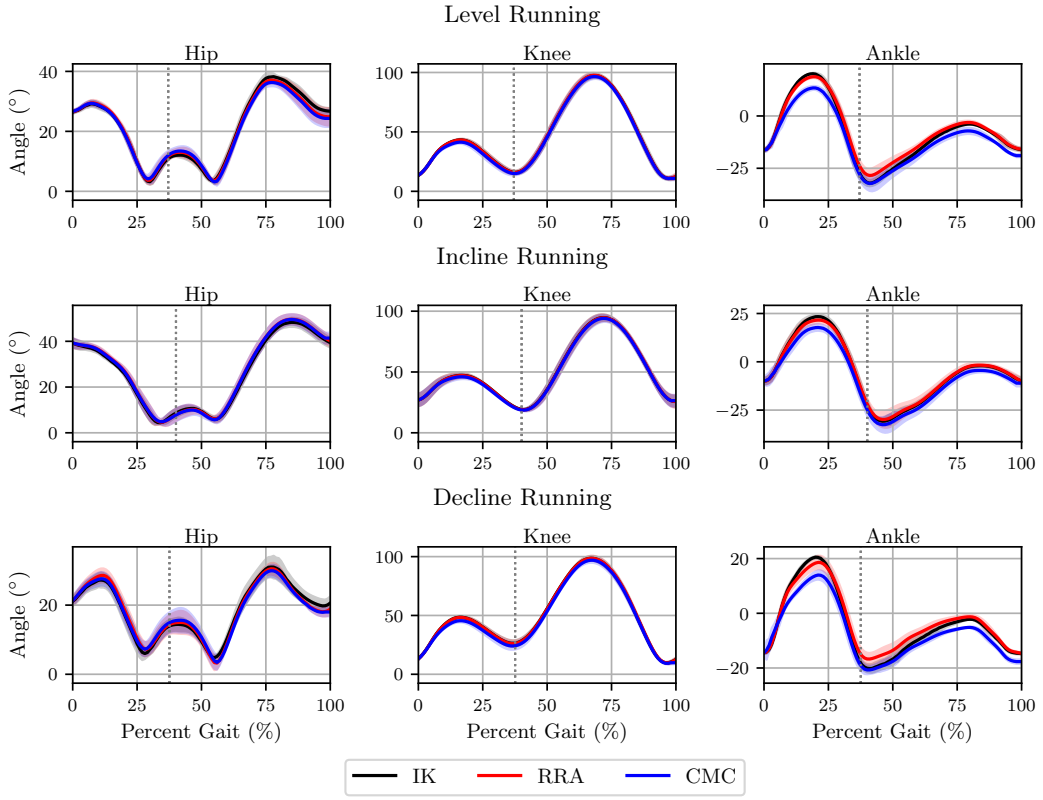

Figure 5.4: Comparison of Participant 2’s resultant hip, knee, and ankle joint kinematics from IK (black), RRA (red), and CMC (blue), for the Hamner *et al.* (2010) model during level (top), incline (middle), and decline (bottom) running conditions

Figure 5.4 indicates that the resultant hip and knee joint kinematics from RRA and CMC follows the IK kinematics curves accurately, with minor deviances in hip angle near the end of gait. However, for the ankle joint kinematics, the resultant joint angle achieved by CMC slightly undershoots the IK and RRA kinematic curves. Appendix C documents the kinematic tracking performance achieved for the remaining participants and models.

Stellenbosch University https://scholar.sun.ac.za

5.2 Model Sensitivity Analysis

Given that a key objective of the project is to develop a series of modified models, from a selected baseline model (Hamner *et al.*, 2010), it is necessary to investigate how the implemented modifications impact model performance (Thabane *et al.*, 2013). For this project in particular, the dynamic loading profiles of the Achilles and patella tendons are of interest, hence the model modifications realized focus on how these tendons are implemented, Chapter 3.

To assess the interactions and influence of these modifications on the dynamic tendon loading profiles, the resulting *in-silico* forces from all of the investigated models are compared using the two-sample t-test discussed in Section 2.5.1. It is important to note that the following section only presents the model sensitivity results of Participant 2, as Participant 2 is the only participant in this study to have a complete set of running analysis results for all of the investigated models and analysed running conditions. In general, the first and second tier models yield tendon force profiles which display significantly similar visual trends in both shape and timing. Consequently, the mean *in-silico* force profiles produced by related modified models, often overlay one another perfectly. Appendix D contains the results for the remaining project participants.

5.2.1 Patella Tendon

Figures 5.5 to 5.7 illustrate the sensitivity analysis results for the patella tendon implantations during level, incline, and decline running conditions. The figures contain numerous sub-figures which are arranged according to data type (rows) and the kind of patella tendon implementation realized within the analysed models (columns). For Figures 5.6 and 5.7, the first and second row of sub-figures present the **spm1d** two-sample t-test results for the comparison between the baseline and first tier models, and the first and second tier models, respectively. In order to provide some insight as to what the **spm1d** results represent, Figure 5.5 contains an additional row of sub-figures that illustrate the mean and SD clouds of the *in-silico* patella tendon loads. The tendon loads have been normalized according to subject BW.

The **spm1d** tests are conducted as two-tailed tests with an unequal variance assumption, Section 2.5.1. The grey shaded areas observed in the **spm1d** sub-figures indicate regions of statistical difference between the compared models, in particular where the p-value for a cluster of statistics is less than the defined statistical significance level ($p < \alpha$, where $\alpha = 0.05$), and is hence greater than the critical threshold value (t^*). The calculated critical threshold value (t^*) is represented by a horizontal dashed line. Due to the fact that the analyses are conducted as two-tailed tests, two horizontal dashed lines are present in each of the **spm1d** sub-figures, illustrating the positive and negative representations of t^*. Additionally, the defined statistical significance level and critical threshold values are indicated in red text at the top of each sub-figure.

Stellenbosch University https://scholar.sun.ac.za

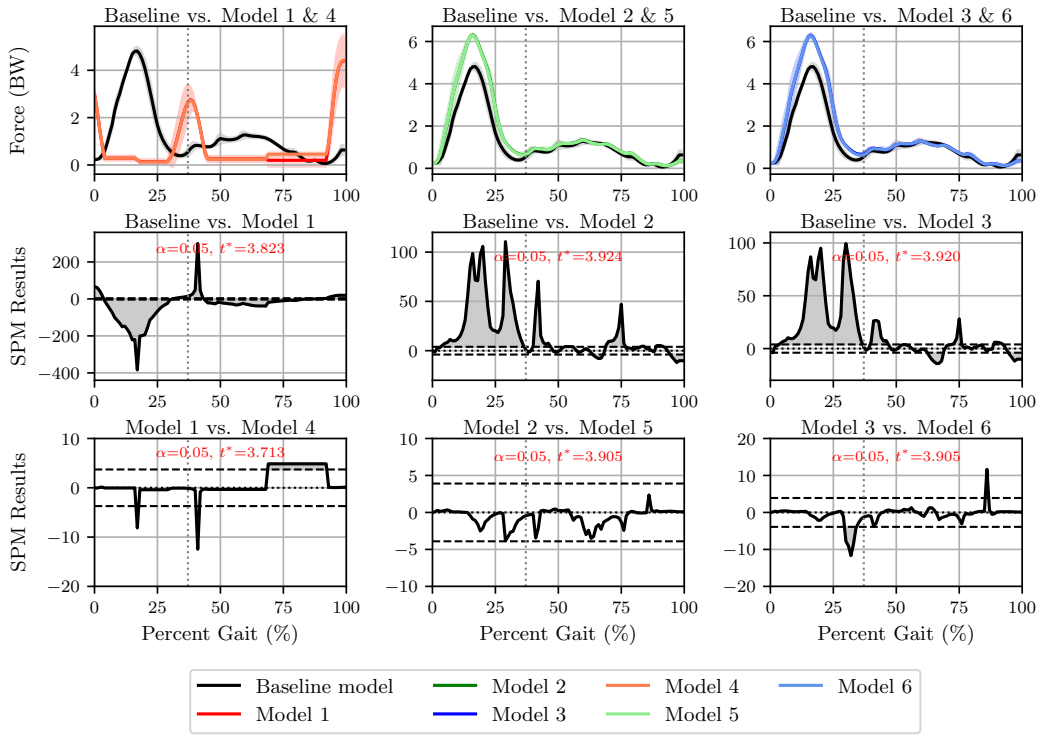

Figure 5.5: Two-sample t-test results of the *in-silico* patella tendon profiles for Participant 2 during level running conditions

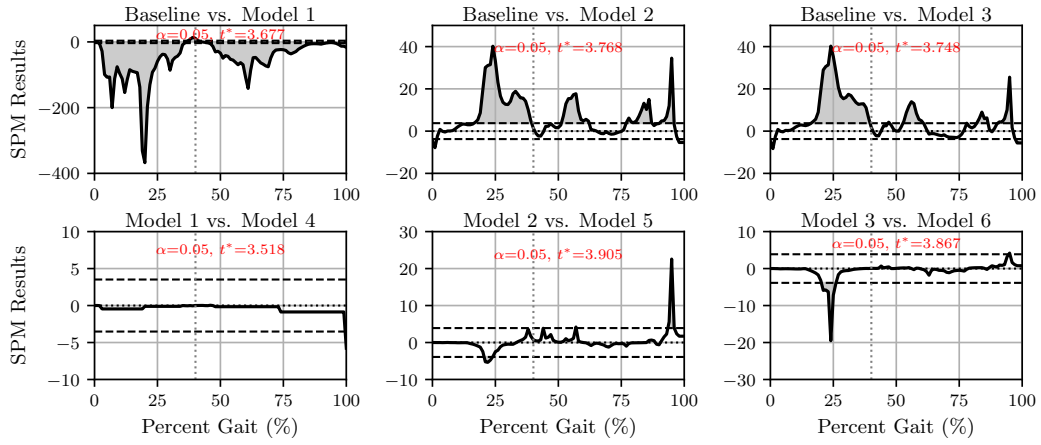

Figure 5.6: Two-sample t-test results of the *in-silico* patella tendon profiles for Participant 2 during incline running conditions

Stellenbosch University https://scholar.sun.ac.za

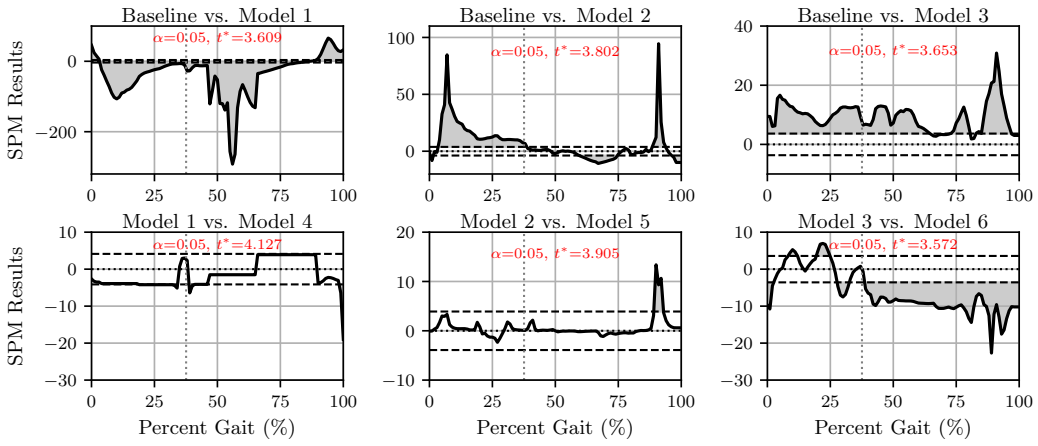

Figure 5.7: Two-sample t-test results of the *in-silico* patella tendon profiles for Participant 2 during decline running conditions

From the above figures it can be concluded that the model with the single ligament fibre implementation of the patella tendon (Model 1) yields the most statistically different results when compared to the baseline model (Hamner *et al.*, 2010). This is highlighted in the above figures by large magnitude to which the regions of statistical difference (clusters) exceed the critical threshold values - in general the "height" of the identified clusters for Model 1 exceed the magnitude of 100, and are significantly larger than the identified critical threshold values ($t^* \approx 3.8$) across all of the analysed running conditions. However, when comparing the *in-silico* loading profiles of the first and second tier models, the **spm1d** results indicate that Models 1 and 4 are the most statistically similar as the majority of the compared loading profiles fall within the critical threshold bands and have a mean peak cluster "height" and critical threshold value of 10 and $t^* \approx 3.9$, respectively.

Similarly, when analysing the **spm1d** results of the narrow and broad implicit tendon implementations (Models 2 and 5, and Models 3 and 6), it is clear that the implicit patella tendon implementations yield the most statistically similar loading profiles to that of the baseline model, as the "height" of the identified clusters are typically less than 100. In general, the patella tendon loading profile produced by Model 2 and 3 exhibit a larger peak force than that of the Hamner *et al.* (2010) model and is not only illustrated by the mean and SD curves in Figure 5.5 but also by the shaded areas that appear above the critical threshold limits in Figures 5.6 and 5.7 during the stance phase. For the comparison between Models 2 and 5, it can be concluded that they produce statistically similar patella tendon loading profiles during level and incline running conditions. The same observations hold true for the comparison between Models 3 and 6, however, during decline running conditions, it is clear that the magnitude of the force profiles produced by Model 6 are smaller than that of Model 3 - this is indicated by the identified cluster located below the critical threshold limit, Figure 5.7.

Stellenbosch University https://scholar.sun.ac.za

5.2.2 Achilles Tendon

Figures 5.8 to 5.10 illustrate the sensitivity analysis results for the Achilles tendon implantations during level, incline, and decline running conditions. The figures take on the same format as those presented in the previous section, Section 5.2.1.

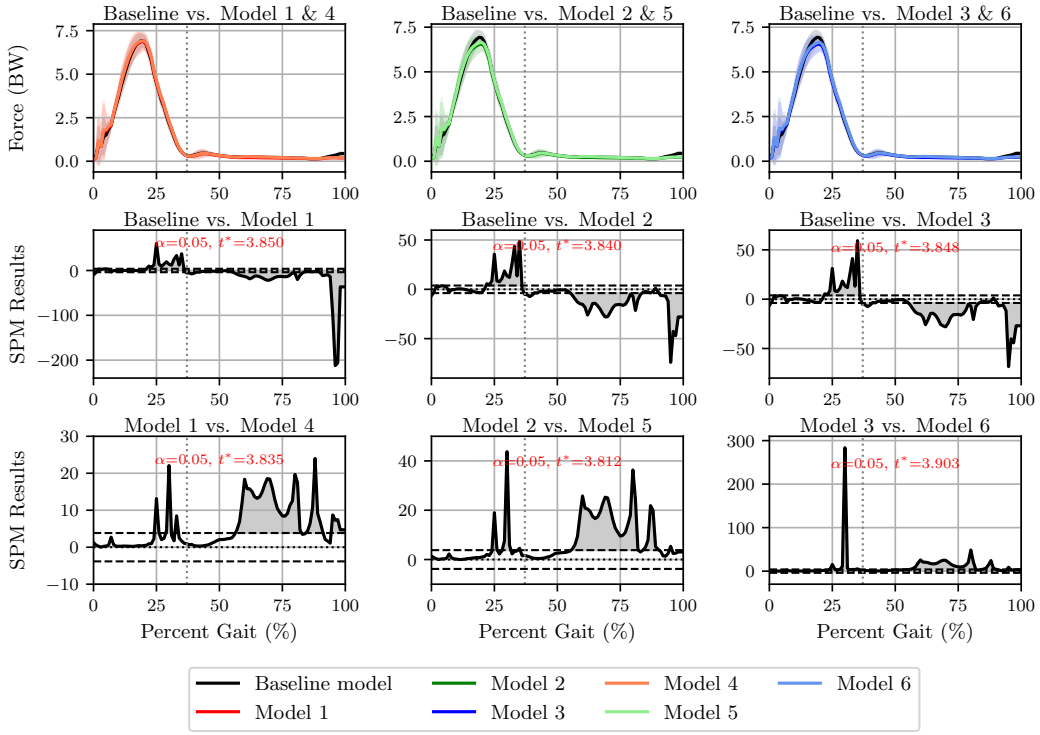

Figure 5.8: Two-sample t-test results of the *in-silico* Achilles tendon profiles for Participant 2 during level running conditions

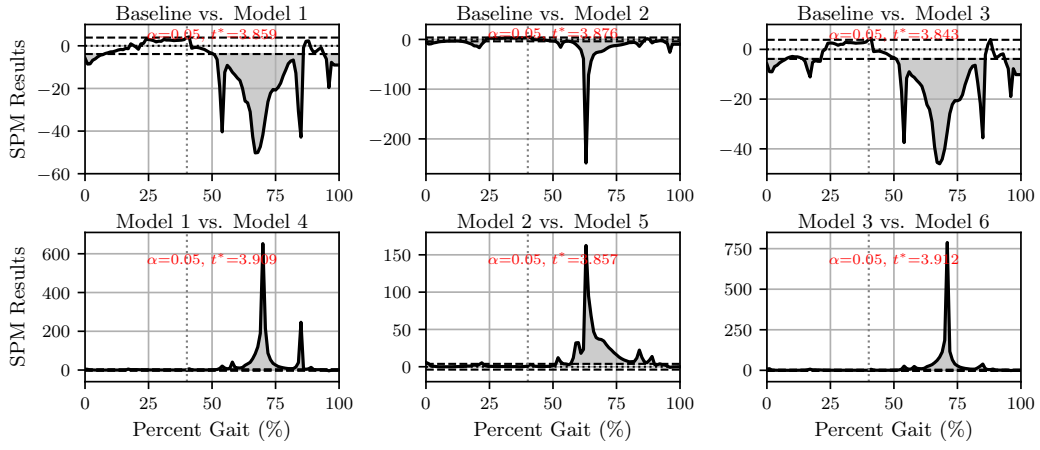

Figure 5.9: Two-sample t-test results of the *in-silico* Achilles tendon profiles for Participant 2 during incline running conditions

Stellenbosch University https://scholar.sun.ac.za

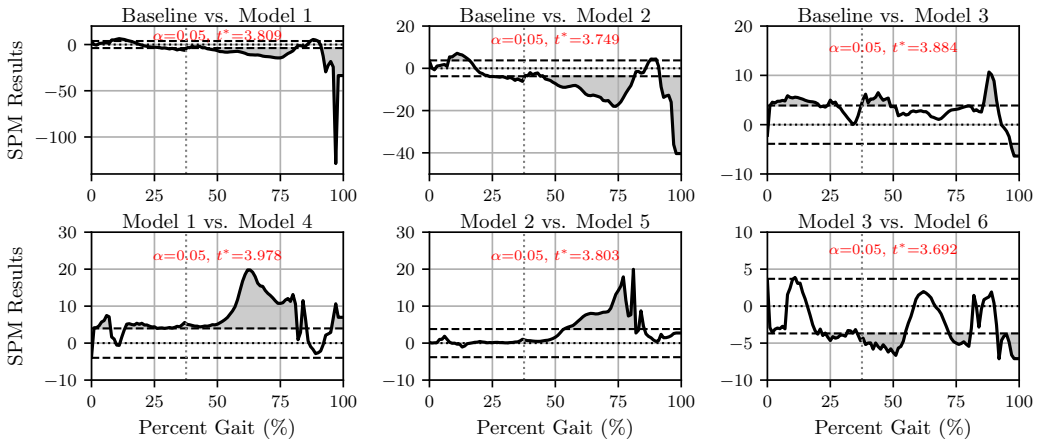

Figure 5.10: Two-sample t-test results of the *in-silico* Achilles tendon profiles for Participant 2 during decline running conditions

Due to the fact that most of the identified clusters in the first tier and baseline **spm1d** results occur below the critical threshold values, it can be concluded that the Achilles tendon profiles produced by the first tier models represent smaller force magnitudes than those produced by the baseline model. Additionally, the above figures indicate that the Achilles tendon loading profiles produced by the modified models display significant statistical differences between 50 % and 100 % gait. Although the observed mean and SD curves seem almost identical in shape and magnitude during this window, their respective SD bands are tight (Figure 5.8). Notably, the magnitude of the force profiles produced by the second tier models, are larger than those of the first tier models for all of the analysed running conditions.

5.3 Independent Trend Analysis

In order to investigate the validity of the *in-silico* method's estimated tendon loading profiles, it is necessary to compare the estimated tendon loading profiles to an independent data set, specifically the *in-vivo* loading profiles obtained during the previous study (Groeneveld, 2020). Due to the fact that the *in-vivo* data sets do not provide accurate tendon force magnitudes (refer to Section 2.3), the validity of the model outputs are only addressed in terms of trends - specifically the trends of the normalized *in-vivo* and *in-silico* data sets. It is important to note that the *in-vivo* and *in-silico* datasets are normalized independently, according to the maximum *in-vivo* and *in-silico* tendon force observed during the running trial, respectively. Due to the fact that the patella tendon implementation realized in Models 1 and 4 do not describe the experimental data well, they will not be discussed in this section and are documented in Appendix E instead. Furthermore, given that the results produced by the narrow and broad implicit patella tendon implementations are similar, and that both variations provide reasonable approximations of the *in-vivo* data, only Models 3 and 6 are discussed in this section, and the results for Models 2 and 5 are documented in Appendix E.

Stellenbosch University https://scholar.sun.ac.za

5.3.1 Patella Tendon

The normalized *in-vivo* and *in-silico* loading profiles for the patella tendon during level, incline, and decline running conditions are illustrated in Figures 5.11 to 5.13. Each figure illustrates the mean tendon force observed during the running gait cycle for the respective data sets and analysed running strides. It is important to note that the mean *in-vivo* tendon force is representative of the first 10 consecutive strides of a given running trial (the same strides which were analysed in the processing pipeline), and the mean *in-silico* tendon forces only represent the running strides that were successfully analysed by the pipeline. Notably, the respective first and second tier models yield force profiles which display significant trend similarities, resulting in the overlaying of some of the *in-silico* force profiles. Furthermore, the shaded areas in each of the proceeding figures illustrate the SD cloud for the respective data sets. TO events are represented by the dotted vertical lines.

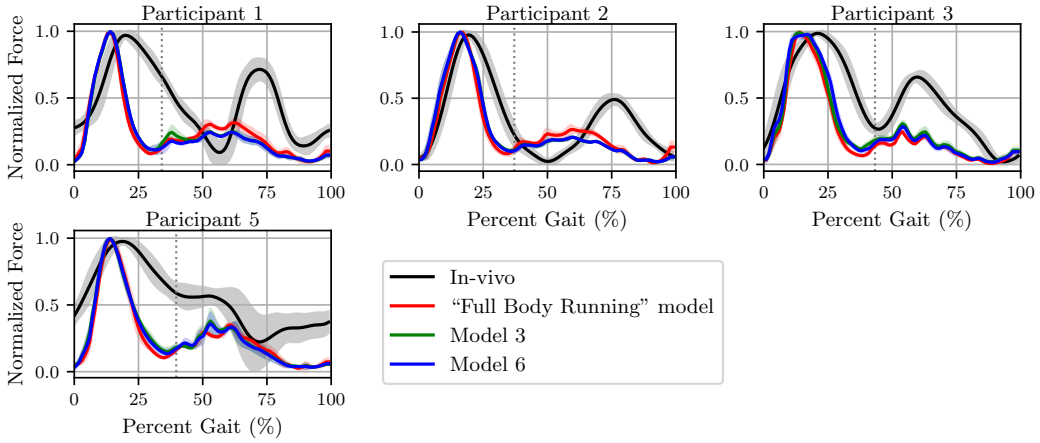

Figure 5.11: Trend comparison between the *in-vivo* and estimated patella tendon loading profiles observed during level running conditions

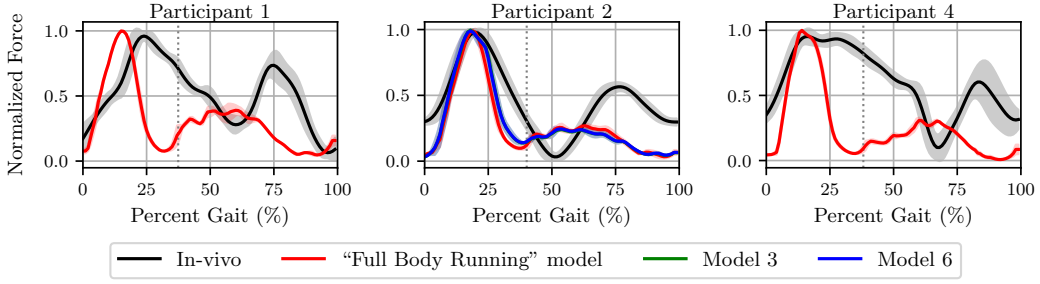

Figure 5.12: Trend comparison between the *in-vivo* and estimated patella tendon loading profiles observed during incline running conditions. Notably, Participant 1 and 4 only have results for the Hamner *et al.* (2010) model

Stellenbosch University https://scholar.sun.ac.za

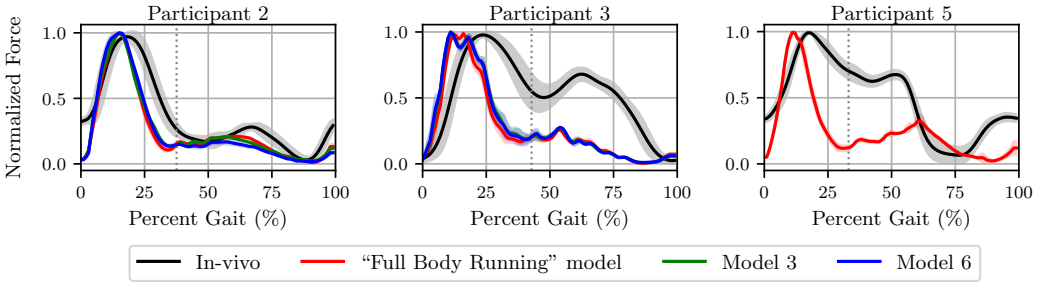

Figure 5.13: Trend comparison between the *in-vivo* and estimated patella tendon loading profiles observed during decline running conditions. Notably, Participant 5 only has results for the Hamner *et al.* (2010) model

From the above figures it can be concluded that despite the fact that the Hamner *et al.* (2010) model has a different patella tendon implementation to Models 3 and 6, all of the compared *in-silico* tendon force profiles have an almost identical shape and timing scheme. In general, the *in-silico* patella tendon loading profiles contain two peaks which occur at different stages of the gait cycle: one during early-to-mid stance ($\approx$ 20 % gait) and the other during early-to-mid swing ($\approx$ 55 % gait). A notable feat of the investigated models is the magnitude of the *in-silico* tendon forces at the end of the gait cycle - they are close to those observed at the beginning of the gait cycle (0 % gait). This indicates that despite the fact that each stride was analysed independently from one another in the processing pipeline, both the Hamner *et al.* (2010) and modified patella tendon implementations result in a continuous, cyclic curve - which is consistent with reality and is expected as running is a continuous, cyclic motion. Furthermore, when comparing the *in-vivo* and estimated profiles, the timing of the first *in-vivo* peak is similar to that of the first *in-silico* peak. This is observed for all participants and running conditions in the Hamner *et al.* (2010) and implicit tendon models, where the *in-silico* peak force leads the *in-vivo* peak force by a maximum of 5 % gait.

With reference to Figures 5.11 and 5.13, the normalized *in-silico* tendon curves for Participants 2 and 3 are the most similar to their respective *in-vivo* loads. Notably, the *in-silico* force curves display almost identical gradient profiles during early stance (0 % - 20 % gait). Additionally, the timing of the second force peak observed for Participants 2 and 3 are most comparable to their reference profile. Table 5.9 presents the COD (R^2) observed for the patella tendon during the investigated running conditions, where the datum COD value is selected as the *in-vivo* patella tendon force for the respective participants and running conditions.

Stellenbosch University https://scholar.sun.ac.za

Table 5.9: Coefficient of determination (R^2) observed for the estimated patella tendon forces during level, incline, and decline running

		R^2		
Model	**Participant**	**Level**	**Incline**	**Decline**
Hamner *et al.* (2010) model	1	0.13	0.04	
	2	0.51	0.51	0.78
	3	0.6		0.35
	4		0.18	
	5	0.52		0.28
Model 3	1	0.21		
	2	0.58	0.58	0.81
	3	0.63		0.27
	4			
	5	0.62		
Model 6	1	0.2		
	2	0.57	0.58	0.83
	3	0.66		0.25
	4			
	5	0.6		

* R^2 is calculated in terms of the *in-vivo* patella tendon loading profiles (Groeneveld, 2020) for the respective running trials ($R^2_{\textit{in-vivo}} = 1.0$)

** Blank table cells indicate no available data for the respective project participant and running condition, as the processing pipeline failed to successfully complete the entire OpenSim running gait analysis workflow implemented

Table 5.9 indicates that the majority of the R^2 values realized by the modified models are consistently larger than those of the Hamner *et al.* (2010) model, with the exception of Participant 3 during decline running conditions. In addition to this, Table 5.9 also indicates that Model 3 performs slightly better than Model 6. Notably, the weakest statistical fit values observed in Table 5.9 are for the Hamner *et al.* (2010) model, specifically for Participant 1 during incline ($R^2 = 0.04$) running conditions. Conversely, the strongest statistical fit values observed in the above table are for Models 3 and 6, specifically Participant 2 during decline running ($R^2 > 0.8$). Given the information in Table 5.9 and Figures 5.11 to 5.13, it can be concluded that the *in-silico* results obtained for Participants 2 and 3 are the most consistent to their corresponding *in-vivo* data sets, across all of the investigated running conditions.

5.3.2 Achilles Tendon

As discussed in Section 2.3.5, Groeneveld (2020) was only able to quantify the *in-vivo* Achilles tendon load for Participant 2. Subsequently, the normalized *in-vivo* and *in-silico* loading profiles of the Achilles tendon for Participant 2 during level, incline, and decline

Stellenbosch University https://scholar.sun.ac.za

running conditions are illustrated in Figure 5.14. The figure takes on the same format as those presented in Section 5.3.1.

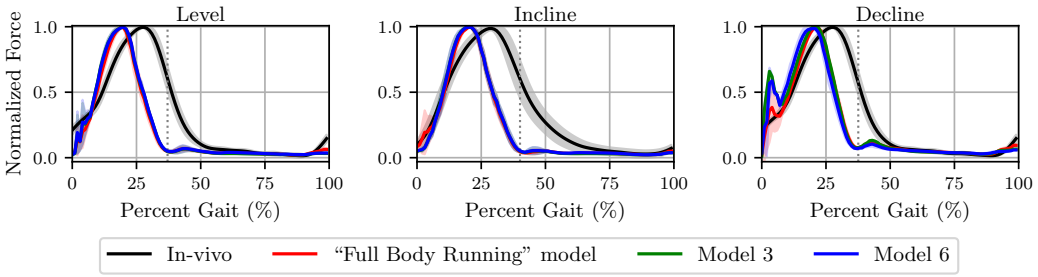

Figure 5.14: Trend comparison between the *in-vivo* and *in-silico* Achilles tendon loading profiles observed during level, incline, and decline running conditions for Participant 2

From the above figure it is clear that the estimated tendon loading profiles during level and incline running are most similar to their corresponding *in-vivo* loading profiles. Despite the fact that both the Hamner *et al.* (2010) model and Model 3 have a different Achilles tendon implementation to that of Model 6, the illustrated *in-silico* tendon force profiles have an almost identical shapes and timing schemes. In general the shape of the *in-silico* Achilles tendon force profiles for the level and incline running conditions comprise of a single major peak near the middle of the stance phase ($\approx$ 20 % gait). For the remainder of the gait cycle, the experienced *in-silico* tendon force is close to zero. Like with the patella tendon implementations discussed in Section 5.3.1, the Achilles tendon implementations display similar force magnitudes at the start and end of the gait cycle, indicating that investigated Achilles tendon implementations yield continuous, cyclic force profiles. Notably, the identified shape and timing trends are observed across all of the *in-silico* Achilles tendon loads (see Appendix D and E).

However, when considering the tendon loading profiles for the decline running condition in Figure 5.14, it is clear that the general shape of the *in-silico* Achilles tendon profile differs to that of the *in-vivo* force profile. In particular, the force profiles differ during early stance (0 % - 10 % gait), where the *in-silico* profiles feature a minor impact peak. Despite this point of difference, the timing of the major peaks in both the *in-vivo* and *in-silico* tendon profiles are similar for all of the analysed models and running conditions, where the *in-silico* peak force leads the *in-vivo* peak force by a maximum of 5 % gait. Table 5.10 presents the COD (R^2) observed for the Achilles tendon during the investigated running conditions and musculoskeletal models, where the respective COD values are calculated in terms of the *in-vivo* Achilles tendon force for Participant 2 and the respective running conditions.

Stellenbosch University https://scholar.sun.ac.za

Table 5.10: Coefficient of determination (R^2) observed for the estimated Achilles tendon forces during level, incline, and decline running for Participant 2

	R^2		
Model	**Level**	**Incline**	**Decline**
Hamner *et al.* (2010) model	0.61	0.61	0.6
Model 3	0.62	0.62	0.61
Model 6	0.62	0.62	0.59

* R^2 is calculated in terms of the *in-vivo* Achilles tendon loading profiles (Groeneveld, 2020) for the respective running trials ($R^2_{\textit{in-vivo}} = 1.0$)

In general, Table 5.10 indicates that both the baseline and modified models, estimate the *in-vivo* Achilles tendon force during level and incline running conditions to a relatively high degree of confidence, with a mean COD value greater than 0.61. As observed in Figure 5.14, the decline running condition yields the weakest statistical fit values observed in Table 5.10, with the smallest R^2 value observed for Model 6 ($R^2 = 0.59$).

Stellenbosch University https://scholar.sun.ac.za

6 Discussion

The aim of this project was to develop an open-source, subject non-specific *in-silico* method that may be utilized to estimate the dynamic loading profiles of the Achilles and patella tendons during treadmill running. As mentioned in Chapter 1, the developed *in-silico* method was restricted to the development of a series of modified musculoskeletal models and an automated processing pipeline. A key focus of the project was to investigate the sensitivity and reliability of the resulting *in-silico* tendon loading profiles, and was addressed by conducting model sensitivity and independent trend analyses. Furthermore, to explore the flexibility of the developed *in-silico* method's capabilities, the *in-silico* method was applied to a large experimental data set (comprising of 5 participants and 3 running conditions) (Groeneveld, 2020).

The most important finding of the study is that subject non-specific gait analysis and musculoskeletal modelling methods may be utilized to achieve reasonable approximations of the Achilles tendon force during various treadmill running conditions. Achieving reasonable estimations of the patella tendon force profile proved to be more challenging, as the *in-vivo* forces experienced by the patella tendon during treadmill running are dependent on subject-specific running gait and muscle activity. Furthermore, the study indicates that the utilization of minimal, non-invasive experimental data sets are sufficient to achieve these reasonable estimations. The following chapter underlines the project's pitfalls and successes. Suggestions and improvements that may be applied in future related studies are discussed in Chapter 7.

6.1 Processing Pipeline

An integral component of the developed *in-silico* method is the automated processing pipeline. In addition to the pipeline objectives highlighted in Section 4.1, the pipeline aims to simplify and streamline the gait analysis process by eliminating the tedious task of manually conducting gait analysis procedures through a GUI, whilst simultaneously reducing the need for user intervention. The pipeline was developed in Python and implements a generic running gait analysis workflow that was designed in OpenSim, see Chapter 4. Moreover, the pipeline has batch processing capabilities and is designed to be malleable, in order to fit the user's needs. An automated data processing functionality, which was developed by the author, provides the necessary tools to transform and filter experimental motion capture (marker trajectory and force place data) and EMG data files, and is included in the pipeline as a voluntary, pre-gait analysis process.

6.1.1 OpenSim Workflow Performance

The implemented OpenSim gait analysis workflow comprised of five processes, namely: Scaling, IK, RRA, CMC, and MA. It is important to note that in order to achieve the desired level of automation and subject non-specific specifications for the pipeline, some

Stellenbosch University https://scholar.sun.ac.za

accuracy was sacrificed. The performance of the implemented OpenSim running gait analysis workflow is evaluated in terms of the degree to which the utilized OpenSim functionalities achieve and minimize their respective error thresholds documented in the OpenSim Users Manual (Simtk-confluence.stanford.edu, 2020).

The scaling process was the first process implemented and was utilized to obtain a scaled version of the desired musculoskeletal model that would be used throughout the remaining gait analysis workflow. The scaling errors were consistent across all of the investigated models for the respective participants, and are discussed in Section 5.1.1. Although the achieved overall RMS errors were not optimal, the project's findings indicate that the incurred scaling errors had little influence on the pipeline's outputs downstream - typically, significant scaling errors would give rise to poor performance of the IK and RRA functionalities. In general, the IK and RRA functionalities performed well, achieving minimal RMS marker errors (RMS $\leq$ 2.3 cm) and "good" force and torque residuals across all of the analysed models and running conditions, see Sections 5.1.2 and 5.1.3, respectively. Furthermore, the IK results were comparable to those documented in literature (Whittle *et al.*, 2000; Telhan *et al.*, 2010).

The results obtained for the CMC functionality displayed "good" residual torque values and inconsistent residual force values. Notably, CMC was the most problematic functionality of the implemented OpenSim workflow, and was the greatest limiting factor of the pipeline. The difficulties encountered with the CMC functionality are likely the product of the utilization of generic tracking weights and control constraints settings. Consequently, these difficulties may be overcome through the utilization of subject and data-specific settings (derived from both kinematic, EMG, and GRF data). However, due to the fact that the project focused on developing a generalized *in-silico* solution, the determination of subject and data-specific settings do not fall within the project scope. Machine learning (ML) algorithms, such as those developed by Samaan *et al.* (2016), provide a relatively simple solution to this problem, however, they are time consuming to implement and computationally demanding. Additionally, if the utilization of different weights and control settings is desired, the generic settings (for any of the implemented gait analysis tools) may be manually altered by the pipeline user through the source-code or the imported XML setup files.

6.1.2 Computational Performance

The computational performance of the pipeline was evaluated in terms of the time taken to complete the implemented OpenSim workflow analysis. In general, the scaling and IK processes each took less than 2 minutes to complete, where the IK process computed the joint kinematic profiles for 10 consecutive running strides. Due to the fact that the RRA tool is run in a loop-fashion until the termination criteria are met, or until the number of iterations exceeds the maximum iteration limit (10 iterations), the computation of dynamically consistent, smoothed joint kinematics took less than 15 minutes per running stride (approximately 1.5 minutes per iteration). The CMC and MA processes ran concurrently and the observed computation time was twice as long as what was experienced for the RRA process, averaging 30 minutes per running stride. Cumulatively, running one instance of the developed processing pipeline, for a single subject

Stellenbosch University https://scholar.sun.ac.za

and a single running trial of 10 strides, equates to approximately 7 hours and 35 minutes. These computational times are based on a the use of one thread of a 2.4 GHz Intel(R) Core™ i7 processor. Using the same machine, the implemented workflow was conducted manually though the OpenSim GUI. Notably, the manual gait analysis process took longer ($\approx$ 45 minutes) to complete one instance of the outlined workflow. Additionally, the manual analysis and processing required extensive user supervision.

6.2 Patella Tendon Modelling

In this study four implementations of the patella tendon were investigated, in particular the original Hamner *et al.* (2010) implementation and three modified variations, Chapter 3. Notably, the *in-silico* patella tendon force profiles realized by the narrow and broad implicit patella tendon implementations display similar shape and timing characteristics to the force profiles produced by the Hamner *et al.* (2010) patella tendon variation. The general shape of these three tendon implementations comprise of two force peaks, one major peak at mid-stance and one minor peak during early-to-mid swing.

The magnitude of the peak *in-silico* forces observed for the investigated patella tendon implementations range between 4 - 6 times BW, and correspond to literature (Scott and Winter, 1990; Schmitz and Piovesan, 2016). To investigate the effect of gradient on the estimated patella tendon forces, the tendon forces observed during incline and decline running conditions were normalized according to the maximum tendon force observed during level running conditions, see Table C.10. The results indicate that the peak tendon loads observed during decline running conditions are larger than those observed during level running conditions. Conversely, the same comparison found that smaller peak forces are observed during incline running conditions compared to those observed during level running conditions. These results correspond with literature (Groeneveld, 2020; Ho *et al.*, 2018; French *et al.*, 2018).

The statistical discrepancies and similarities between the selected baseline model (Hamner *et al.*, 2010) and the modified patella tendon implementations, were identified in the model sensitivity analysis (Pataky, 2012). An important aspect of the model sensitivity analysis results lies in the fact that two models, each representing the same subject, will always differ statistically as their inherent model calculations are consistently different. Consequently, not only does the model sensitivity analysis identify inter-model deviances, but also contains additional inter-subject variability. Notably, the analysis between the baseline and single ligament fibre implementations highlighted numerous regions of significant statistical difference between the tendon force profiles - indicating that the single ligament fibre variation generates a force profile with a significantly different shape and timing scheme to the baseline model. Conversely, the only significant statistical difference that was identified between the two modified implicit and baseline patella tendon force profiles, was the increased peak tendon force observed in the narrow and broad implicit tendon models. This force magnitude deviation is a result of the modifications made to the respective quadriceps muscle parameters during the model development stage, see Table A.4. Finally, the model sensitivity analysis results indicate that the incorporation of the modified Achilles tendon implementation, had no

Stellenbosch University https://scholar.sun.ac.za

significant effect on the performance of the investigated patella tendon variations - as only minor statistical difference regions were identified between the first and second tier model comparisons.

As previously discussed, Chapter 2, the patella tendon forms part of the complex knee extensor mechanism, which is actuated and influenced by a number of different muscles and subject-specific factors. The independent trend analysis indicated that achieving reasonable approximations of the dynamic patella tendon load during running, with minimal subject and data-specific modelling and analysis techniques, would be no simple feat. Given that the normalized *in-vivo* tendon force profiles, as well as the subject-specific EMG signals, deviated significantly across the study's participant pool, it may be concluded that the load experienced by the patella tendon is highly sensitive to subject-specific running styles and muscle usage/manipulation during running. In general, the narrow and broad implicit tendon implementations (Models 2 and 5, and Models 3 and 6, respectively) performed best, achieving the best statistical fit values for level ($R^2 >$ 0.6 for Participants 3 and 5), incline ($R^2 =$ 0.58 for Participant 2), and decline ($R^2 >$ 0.8 for Participant 2) running conditions. This superior performance is due to the fact that the modified implicit implementations of the patella tendon, provide more accurate representations of the patellofemoral joint than the Hamner *et al.* (2010) model. Notably, the fit values for Participant 2 during level running conditions were also reasonable ($R^2 >$ 0.56). Conversely, the fit values achieved for the single ligament fibre implementation (Models 1 and 4) were extremely weak for all of the running conditions ($R^2 \leq$ 0.13).

When analysing the general timing schemes of the patella *in-silico* and *in-vivo* force profiles, the narrow and broad implicit tendon implementations, as well as the Hamner *et al.* (2010) tendon implementation, estimate the major peak tendon force 5 % gait earlier than the observed *in-vivo* peak patella tendon force (Section 5.3.1 and Appendix E.1). Hicks *et al.* (2015) indicates that when validating musculoskeletal model performance in terms of experimental data, a timing difference of approximately 75 ms between simulated muscle-tendon forces and experimental data sets is acceptable (this roughly equates to 7.5 % gait).

With respect to the single ligament fibre patella tendon implementation, as highlighted in Chapter 3, it was expected that the single ligament fibre implementation of the patella tendon would yield undesirable results. This expectation was based on the understanding and research into the fundamental operating capabilities of OpenSim and how ligament forces are determined. The project findings confirmed that the single ligament fibre implementation performed poorly. The poor performance of this patella tendon variation may be as a result of two factors. The first reason considers the fact that OpenSim requires bone translation (in this case the patella bone) to be defined as along a specific path and in a fixed manner during a certain range of joint angles, and does not account for applied muscle forces on bone movement. Furthermore, implemented ligament force is a function of the defined normalized force-length curve and instantaneous fibre length during locomotion, refer to Equation 3.8 and Figure A.4. With the consideration of the length curve in relation to knee flexion angle (Figure A.5), it was concluded that at knee flexion angles larger than 40°, the length of the ligament fibres

Stellenbosch University https://scholar.sun.ac.za

are less than the normalized fibre length - hence no tensile force is generated.

6.3 Achilles Tendon Modelling

The study investigated two implementations of the Achilles tendon, in particular the original Hamner *et al.* (2010) implementation, as well as a modified variation, Chapter 3. The *in-silico* Achilles tendon force profiles realized in this study display similar characteristics to the profiles documented in literature (Roberts and Belliveau, 2005) and represent the cumulative tendon force of the soleus and gastrocnemius muscles in the investigated OpenSim models (Doral *et al.*, 2010). In general, the estimated dynamic force profiles exhibit a single major peak force at mid-stance, and little to no force during the swing phase. Notably, the estimated force profiles for the Achilles tendon during decline running conditions also display a minor impact peak during early stance. The magnitude of the *in-silico* peak forces for the investigated Achilles tendon implementations range between 4 - 7.5 times BW, and correspond to literature (Scott and Winter, 1990; Burdett, 1982).

To investigate the effect of gradient on the estimated tendon forces, the tendon forces observed during incline and decline running conditions were normalized according to the maximum tendon force observed during level running conditions, Table C.11. The investigation found that the peak tendon loads observed during decline running conditions were less than those observed during level running conditions. Conversely, the peak tendon loads observed during incline running conditions were greater than those observed during level running conditions. Neves (2014) investigated the Achilles tendon during level and moderately sloped ($\pm$ 6° gradient) running conditions, and concluded that the peak Achilles tendon forces observed during decline running conditions are greater than those observed during level running conditions. Additionally, Neves (2014) indicated that incline running conditions yield the smallest peak Achilles tendon loads.

Although the identified relationship between the peak Achilles tendon *in-silico* forces and gradient do not correspond with literature (Neves, 2014), the resulting deviations can be explained in terms of how the CMC and MA tools compute muscle-tendon forces. As discussed in Chapter 2, CMC and MA compute musculotendon forces based on the estimated muscle activation levels and muscle-tendon fibre lengths which achieve the desired kinematic and GRF data sets. This approach yields musculotendon force estimations that are a direct reflection of the instantaneous muscle-tendon fibre length during an analysed motion. Consequently, the increased and decreased peak Achilles tendon forces observed during incline and decline running conditions are the direct result of an increased dorsiflexion and plantar flexion angle of the foot, respectively (Lichtwark and Wilson, 2006).

In terms of the model sensitivity analysis, the only significant statistical differences that were identified between the Hamner *et al.* (2010) and modified Achilles tendon implementations, occurred during the swing phase. As mentioned in Chapter 5, these statistical differences are most likely as a result of the small variances observed for respective force profiles during the swing phase (i.e. tight SD bands), as visually, the force curves

Stellenbosch University https://scholar.sun.ac.za

lie precisely on-top of one another.

Given that the only available *in-vivo* data for the Achilles tendon was for Participant 2, for all of the respective running conditions, the independent trend analysis of the *in-silico* Achilles tendon force is considered to be a case study. The trend analysis found that for all of the analysed running conditions, both the Hamner *et al.* (2010) and modified Achilles tendon implementations achieve reasonable approximations of the *in-vivo* Achilles force profiles ($R^2 > 0.55$). Notably, the best statistical fit values observed for level running conditions were achieved by Models 2, 3, 5, and 6 ($R^2 = 0.62$). Similarly, for incline and decline running conditions the best statical fit values were achieved by Models 2 and 5 ($R^2 = 0.64$), and Model 3 ($R^2 = 0.61$), respectively.

When comparing the general, visual trends and timing schemes of the Achilles *in-silico* and *in-vivo* force profiles, there are two points of difference. The first point of difference is the timing of the peak *in-silico* force: in general, the peak *in-silico* force leads the peak *in-vivo* force by a maximum of 5 % gait - this is a reasonable and acceptable performance as reported by Hicks *et al.* (2015). The second point of difference is observed during late stance and early swing - the *in-silico* force profiles demonstrate a faster de-loading period (approximately 2 times faster than observed in the *in-vivo* force profiles). These two observations may be described as a result of the inherent effects of a simulation environment, where the idealistic results which do not account for real-world interferences and tendon characteristics are realized.

6.4 Problems and Pitfalls

With the consideration of the entire *in-silico* method, the gait analysis of running trials for inclined and declined running conditions proved to be challenging. In general, the developed *in-silico* method is best suited for level running trial analyses as all of the conducted analyses, for the project participants with level running experimental data, were successful. When comparing the size of the complete results population for the selected baseline (Hamner *et al.*, 2010) and modified models, the Hamner *et al.* (2010) model yielded the larger results population for both the incline (Participants 1, 2, and 4) and decline (Participants 2, 3, and 5) running conditions. The observation is most likely the result of unintentional musculoskeletal modelling constraints and over-generalized gait analysis settings.

Underlying musculoskeletal modelling constraints give rise to model performance instability. Despite the fact that the patella bone geometry has been incorporated in many other musculoskeletal models (Rajagopal *et al.*, 2016; Arnold *et al.*, 2010; Lai *et al.*, 2017; Schmitz and Piovesan, 2016), it is likely that its incorporation into the modified models, and the accompanying modified tendon variations, introduced unforeseen constraints on model performance (Delp *et al.*, 1999). In addition to modelling constraints, the defined gait analysis settings are derived from the simulations conducted by Hamner *et al.* (2010) with the study's selected baseline model, and are likely over-generalized, Section 6.1.1.

Stellenbosch University https://scholar.sun.ac.za

7 Conclusion

In this study an open-source, subject non-specific *in-silico* method was developed and utilized to estimate the dynamic loading profiles of the patella and Achilles tendons during varying treadmill running conditions. The study expands on a previous Masters project (Groeneveld, 2020), and aims to provide a basic tool that offers a low-risk and non-invasive alternative to current dynamic tendon load quantification processes. The developed *in-silico* method comprises of a series of pre-existing and modified musculoskeletal models, as well as a fully automated processing pipeline that implements a generic OpenSim gait analysis workflow (Simtk-confluence.stanford.edu, 2020). The robustness and reliability of the *in-silico* method was evaluated through model sensitivity and independent trend analyses.

The study found that subject non-specific modelling and gait analysis techniques may be used to achieve reasonable estimations of the dynamic loading profiles of the Achilles tendon during level, incline, and decline running conditions. Furthermore, the study indicates that the utilization of minimal, non-invasive experimental data sets are sufficient to achieve these reasonable estimations. Realizing reasonable approximations for the patella tendon proved to be challenging, as the project focused on developing a generalized solution which would not take into account subject-specific muscle activity. The study findings also indicate that the stability of the developed solution is sensitive to running surface gradient, and is best suited for level running gait analyses. Although Models 2, 3, 5, and 6 achieve marginally better trend approximations than the selected baseline model (Hamner *et al.*, 2010), the study indicates that the baseline model has better computational stability. Consequently, the utilization of the Hamner *et al.* (2010) model in future studies is sufficient. For studys that focus on incline and decline running conditions, it is recommended that the default gait analysis settings be modified.

Given that the scope of the project restricted the utilization of the OpenSim gait analysis workflow tools to those of the basic, core functionalities distributed with the OpenSim GUI software, the utilization of user-contributed plug-ins was not realized in the developed processing pipeline. Research shows that the probability of achieving better estimations of muscle-tendon parameters significantly improves when using EMG-driven and informed algorithms (Pizzolato *et al.*, 2015; Atkinson, 2018). The Calibrated EMG-Informed Neuromusculoskeletal Modelling Toolbox (CEINMS) is an example of such an algorithm and is a popular open-source, user-contributed OpenSim plug-in (Pizzolato *et al.*, 2015). The incorporation of an EMG-informed method, such as CEINMS in the developed pipeline (or similar workflows), could provide improved muscle-tendon parameter estimations for the patella tendon in particular. Furthermore, differences between the two muscle estimation methods in this specific application, may be realized. The investigation of the modified patella tendon structures, in particular the single ligament fibre variation, on a software platform which incorporates the influence of muscle activity on bone translation and rotation during locomotion, is further recommended.

Stellenbosch University https://scholar.sun.ac.za

A OpenSim Models: Supplementary Information

A.1 Hamner *et al.* (2010) Musculoskeletal Model

The following section presents supplementary information for the Hamner *et al.* (2010) model, discussed in Chapter 3. Table A.1 shows the inertial and mass properties of the generic and unscaled version of the Hamner *et al.* (2010) model's body segments.

Table A.1: Inertial and mass properties of each body segment of the "Full Body Running" model (Hamner *et al.*, 2010). The tabulated data is based off of the height and weight settings of the default, unscaled version of the model

Segment	Mass (kg)	Inertia XX ($kg \cdot m^2$)	Inertia YY ($kg \cdot m^2$)	Inertia ZZ ($kg \cdot m^2$)
Pelvis	11.77	0.1028	0.0871	0.0579
Femur	9.30	0.1339	0.0351	0.1412
Tibia/Fibia	3.71	0.0504	0.0051	0.0051
Talus	0.10	0.0010	0.0010	0.0010
Calcaneus	1.25	0.0014	0.0039	0.0041
Toes	0.22	0.0001	0.0002	0.0010
HAT	26.83	1.4745	0.7555	1.4314
Humerus	2.03	0.0119	0.0041	0.00134
Ulna	0.61	0.0030	0.0006	0.0032
Radius	0.61	0.0030	0.0006	0.0032
Hand	0.46	0.0009	0.0005	0.0013

Similarly, Table A.2 shows the musculotendon properties of the generic and unscaled version of the Hamner *et al.* (2010) model's body segments.

Stellenbosch University https://scholar.sun.ac.za

Table A.2: Musculotendon parameters of the “Full Body Running” model (Hamner *et al.*, 2010)

Muscle	**Max. Isometric Force,** F_0^M **(N)**	**Optimal Fibre Length,** l_0^M **(m)**	**Tendon Slack Length,** l_0^T **(m)**	**Pennation Angle,** θ_{PA} **(°)**
Adductor brevis	429	0.133	0.02	0
Adductor longus	627	0.138	0.11	6
Adductor magnus (distal)	381	0.087	0.06	5
Adductor magnus (middle)	343	0.121	0.12	3
Adductor magnus (posterior)	488	0.131	0.249	5
Biceps femoris long head	896	0.109	0.326	0
Biceps femoris short head	804	0.173	0.089	23
Extensor digitorum longus	512	0.102	0.345	8
Extensor hallucis longus	162	0.111	0.305	6
External oblique	900	0.120	0.14	0
Erector spinae	2500	0.120	0.03	0
Flexor digitorum longus	310	0.034	0.4	7
Flexor hallucis longus	322	0.043	0.38	10
Gastrocnemius lateral head	683	0.064	0.38	8
Gastrocnemius medial head	1558	0.06	0.39	17
Gluteus maximus (superior)	573	0.142	0.125	5
Gluteus maximus (middle)	819	0.147	0.127	0
Gluteus maximus (inferior)	552	0.144	0.145	5
Gluteus medius (anterior)	819	0.054	0.078	8
Gluteus medius (middle)	573	0.085	0.053	0

Stellenbosch University https://scholar.sun.ac.za

Muscle	Max. Isometric Force, F_0^M (N)	Optimal Fibre Length, l_0^M (m)	Tendon Slack Length, l_0^T (m)	Pennation Angle, θ_{PA} (°)
Gluteus medius (posterior)	653	0.065	0.053	19
Gluteus minimus (anterior)	270	0.068	0.016	10
Gluteus minimus (middle)	285	0.056	0.026	3
Gluteus minimus (posterior)	323	0.038	0.051	1
Gemellus	164	0.024	0.039	0
Gracilis	162	0.352	0.126	3
Iliacus	1073	0.1	0.1	7
Internal oblique	900	0.1	0.1	0
Periformis	444	0.026	0.115	10
Peroneus brevisde	435	0.05	0.161	5
Peroneus longusde	943	0.049	0.345	10
Peroneus tertius	180	0.079	0.1	13
Psoas	1113	0.1	0.16	8
Quadratus femoris	381	0.054	0.024	0
Rectus femoris	1169	0.114	0.31	5
Sartorius	156	0.052	0.1	0
Semimembranosus	1288	0.08	0.359	15
Semitendinosus	410	0.201	0.256	5
Soleus	3549	0.05	0.25	25
Tensor fascia latae	233	0.095	0.425	3
Tibialis anterior	905	0.098	0.223	5
Tibialis posterior	1588	0.031	0.31	12
Vastus intermedius	1365	0.087	0.136	3
Vastus lateralis	1871	0.084	0.157	5
Vastus medialis	1294	0.089	0.126	5

Figures A.1 and A.2 illustrate the front and back view of the reflective marker placement on the participants, respectively. It is important to note that the orange markers are computed, virtual markers based off of the Vicon Motion Capture Systems algorithms, and are not physical markers.

Stellenbosch University https://scholar.sun.ac.za

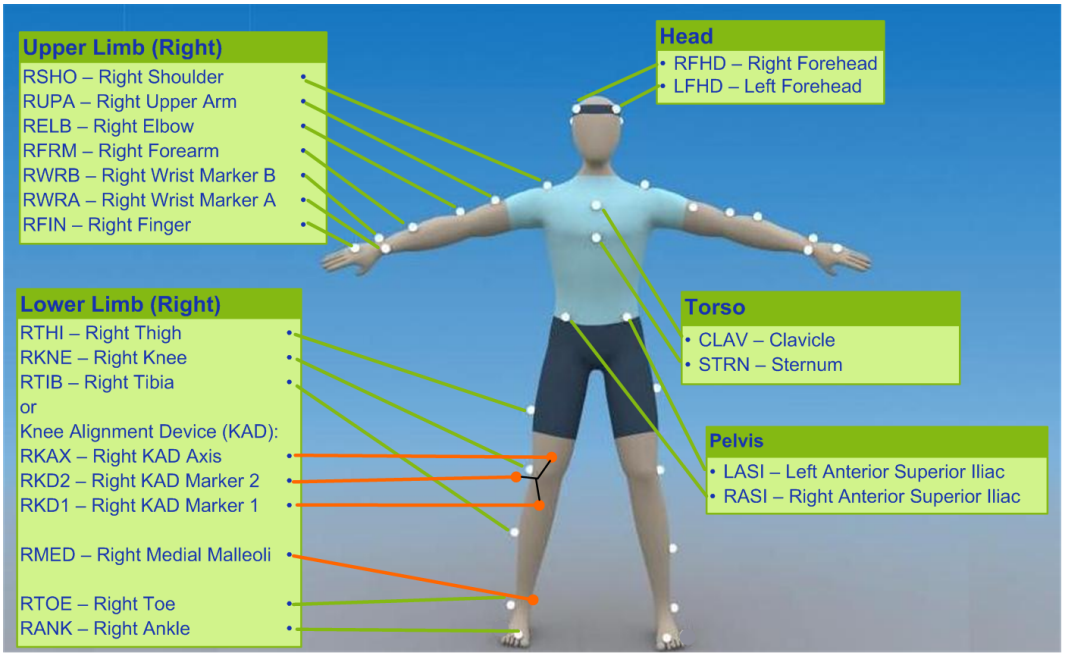

Figure A.1: Front view of marker placement (Groeneveld, 2020; Vicon, 2019)

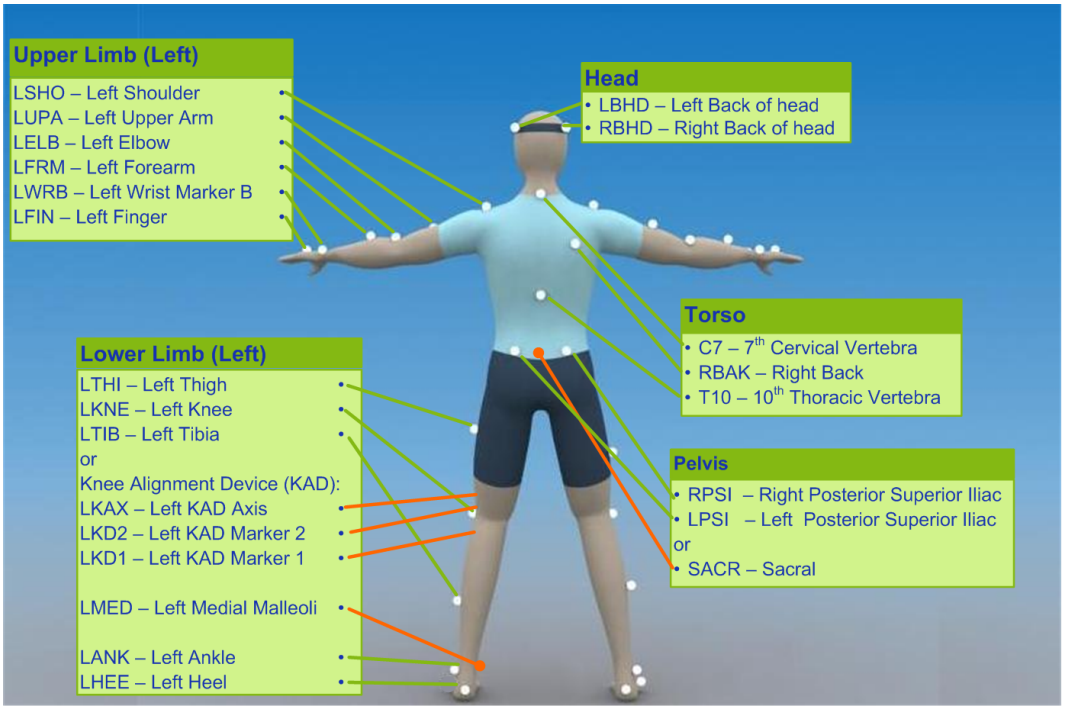

Figure A.2: Back view of marker placement (Groeneveld, 2020; Vicon, 2019)

Stellenbosch University https://scholar.sun.ac.za

A.2 Modified Musculoskeletal Models

The following section presents supporting information to the decisions made in Chapter 3, with regards to model development and modification. Table A.3 shows the inertial and mass properties of the patella bone geometry incorporated in each of the 6 modified models.

Table A.3: Inertial and mass properties of the patella bone geometry. The mass and inertial properties are defined according to cadaver literature (Delp, 1990; Anderson and Pandy, 1999), and are based off of the height and weight settings of the default, unscaled version of the Hamner *et al.* (2010) model

Segment	**Mass (kg)**	**Inertia XX ($kg{\cdot}m^2$)**	**Inertia YY ($kg{\cdot}m^2$)**	**Inertia ZZ ($kg{\cdot}m^2$)**
Patella	0.0862	0.00000287	0.00001311	0.00001311

Figure A.3 illustrates the moment arm curves for the single ligament fibre implementation of the patella tendon during different angles of knee flexion. The moment arm curve was validated against the Arnold *et al.* (2010) model's single muscle fibre patella tendon and is illustrated by the black dashed curve. It is important to note that unlike the modified models in this study, the Arnold *et al.* (2010) model has a maximum knee flexion angle of 100°.

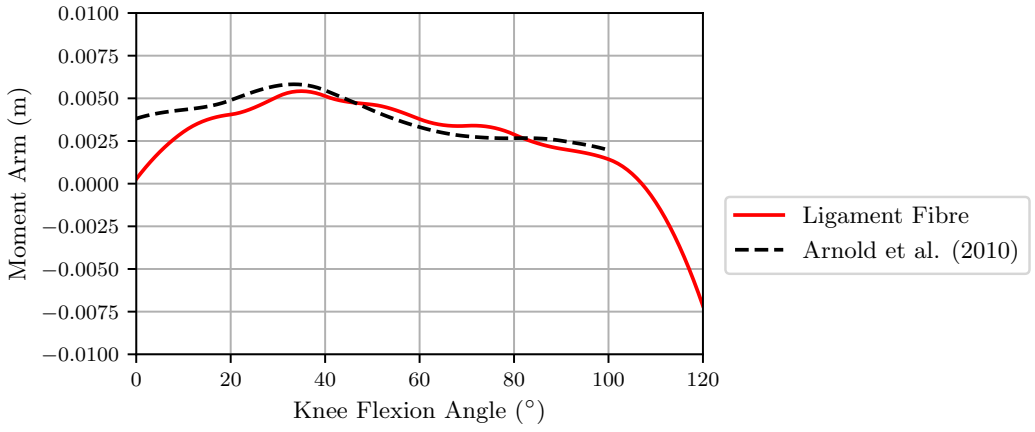

Figure A.3: Moment arm validation plot of the implemented patella tendon single ligament fibre model documented in Chapter 3. The ligament (red) fibre's moment arm is compared to the moment arm of the patella tendon fibre realized in the Arnold *et al.* (2010) model (black dashed) during different angles of knee flexion

Figure A.4 illustrates the derived normalized force-length curve of the single ligament fibre variation of the patella tendon, based off of Equation 3.8 (Thelen, 2003).

Stellenbosch University https://scholar.sun.ac.za

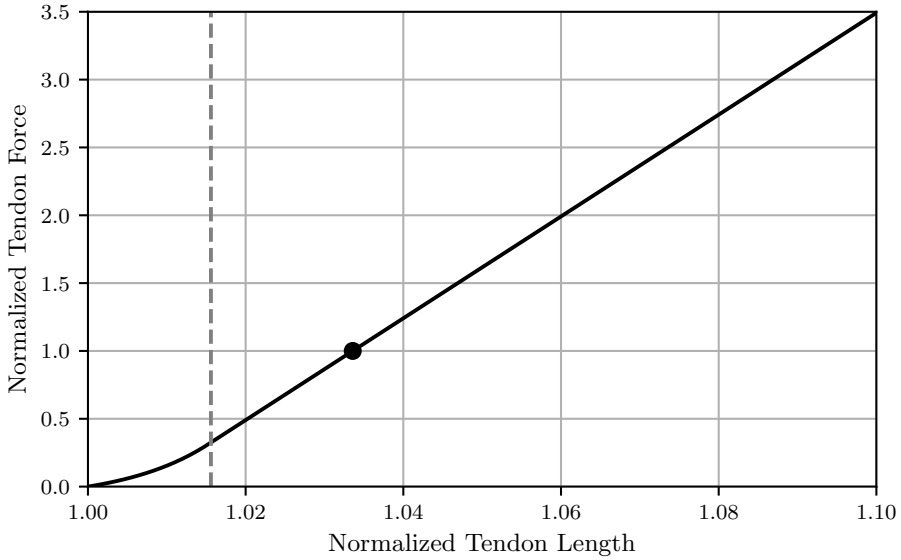

Figure A.4: Graph illustrating the derived normalized force-length curve of the patella tendon, Equation 3.8 (Thelen, 2003). The dashed grey line separates the toe region (left of the dashed line) and the linear-elastic region (right of the dashed line) of the tendon. The black dot highlights the normalized length at which one norm of the tendon force is realized - i.e. F_0^M is reached

As discussed in Chapter 3, the force produced by a ligament fibre is a function of its normalized force-length curve and instantaneous length during locomotion, refer to Equation 3.8 and Figure A.4. Due to the fact that modelled ligament fibre connects the distal end of the patella to the tibial tuberosity of the tibia, and that both the patella and tibia translate and rotate relative to the distal end of the femur during knee flexion (Arnold *et al.*, 2010; Delp *et al.*, 1999), the generated force is representative of the instantaneous distance between the respective attachment sites on the two bone geometries. Figure A.5 shows respective normalized instantaneous length curves of the ligament fibre in relation to knee flexion angle, during the full knee flexion range and running gait.

Stellenbosch University https://scholar.sun.ac.za

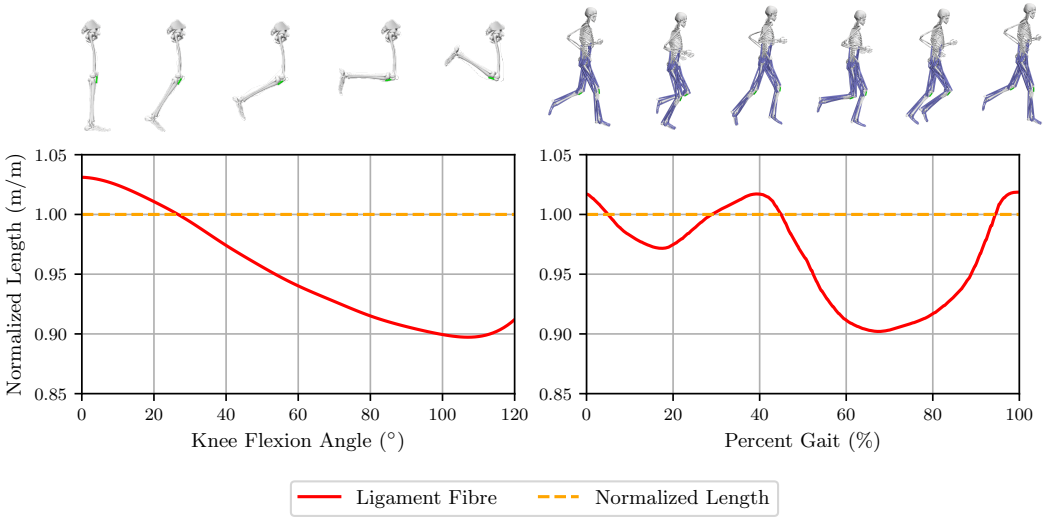

Figure A.5: Investigation of the normalized ligament fibre length in relation to knee flexion angle. The left subplot illustrates the normalized ligament fibre length curve observed during the full knee flexion range realized in the modified models (0° - 120°). The right subplot illustrates the normalized ligament fibre length observed during the running gait cycle. The normalized length of the ligament fibre (red), as well as the normalized fibre length threshold (dashed yellow) are illustrated in both figures

Table A.4 shows the modified muscle properties of the rectus femoris, vastus lateralis, vastus medialis, and vastus intermedius muscles in the implicit patella tendon model variations.

Table A.4: Summary of the modified muscle properties of the rectus femoris, vastus lateralis, vastus medialis, and vastus intermedius muscles in the implicit patella tendon model variations, values adapted from Rajagopal *et al.* (2016)

Muscle	**Max. Isometric Force,** F_0^M **(N)**	**Optimal Fibre Length,** l_0^M **(m)**	**Tendon Slack Length,** l_0^T **(m)**	**Pennation Angle,** θ_{PA} **(°)**
Rectus femoris	2192	0.076	0.448	12.4
Vastus lateralis	5149	0.099	0.221	14.5
Vastus medialis	2748	0.097	0.200	24.2
Vastus intermedius	1697	0.099	0.202	3.6

Stellenbosch University https://scholar.sun.ac.za

B Processing Pipeline: Supplementary Information

B.1 Folder Structure Requirements

The following section communicates the general folder structure requirements for the developed processing pipeline, Figures B.1 to B.6.

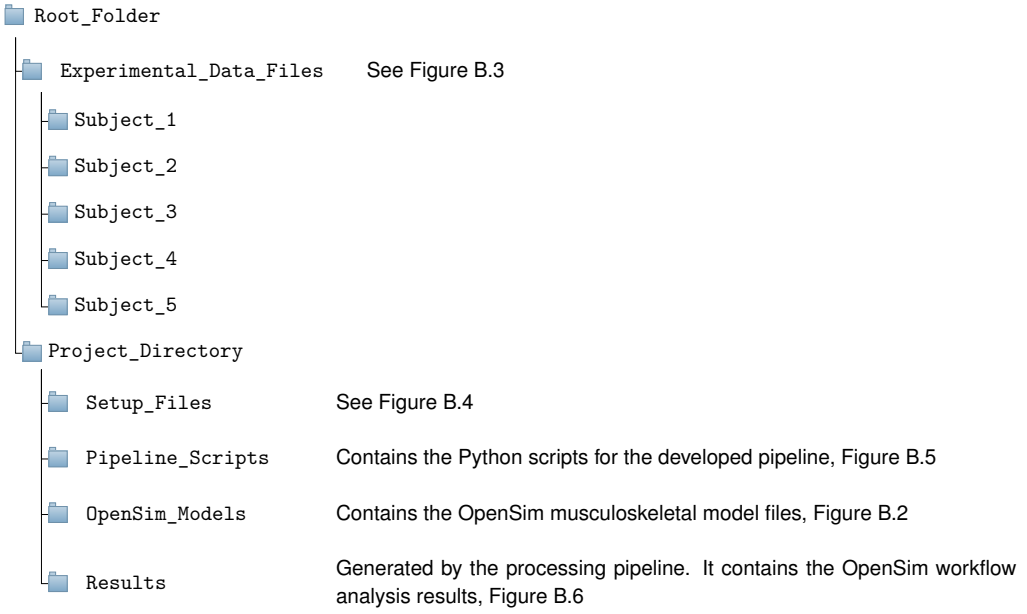

Figure B.1: Folder structure requirements for the developed processing pipeline

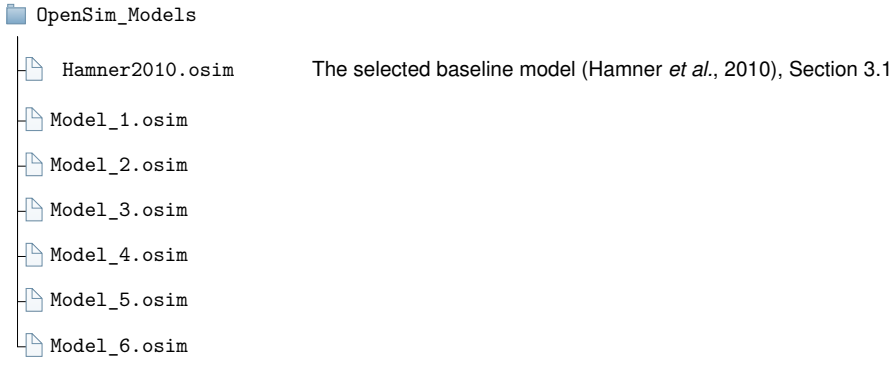

Figure B.2: Folder format for the OpensSim musculoskeletal model folder

Stellenbosch University https://scholar.sun.ac.za

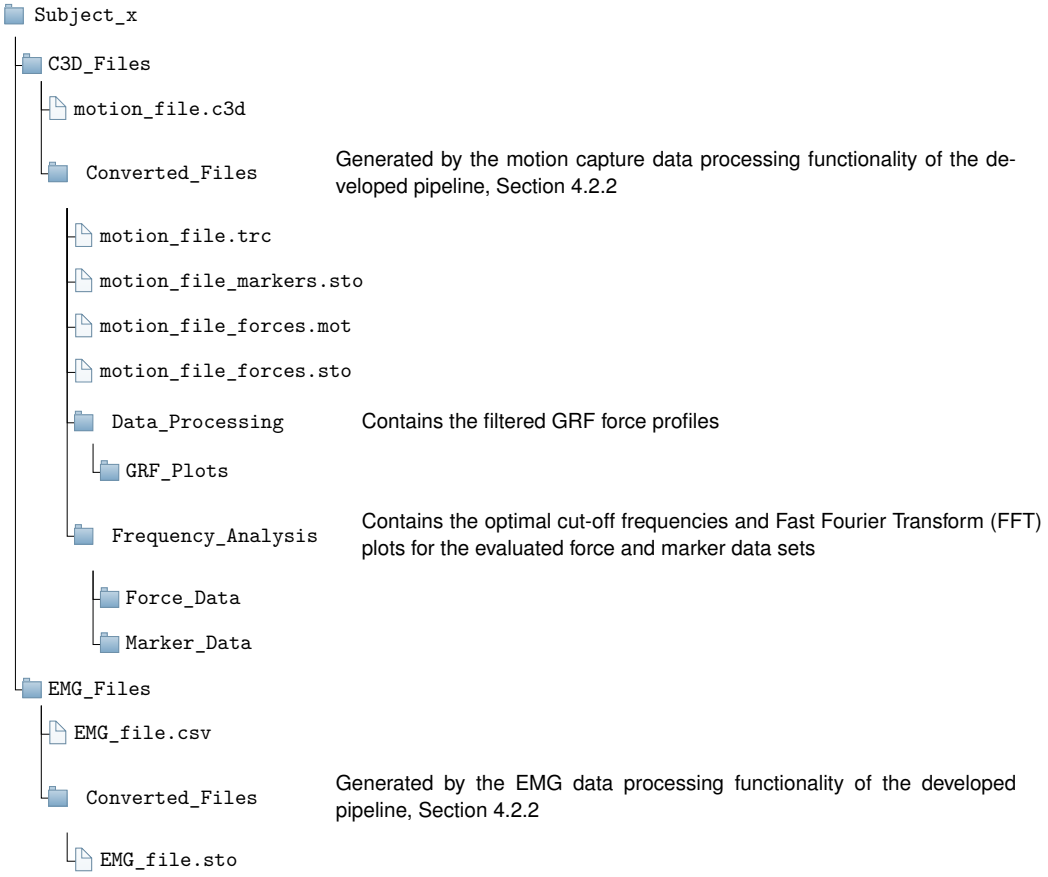

Figure B.3: Folder structure requirements for each subject's experimental data folder

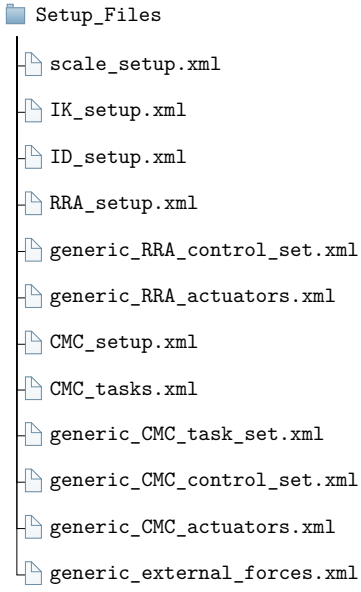

Figure B.4: Folder structure requirements for the OpensSim workflow setup files

Stellenbosch University https://scholar.sun.ac.za

Figure B.5: Internal folder structure for the developed processing pipeline scripts

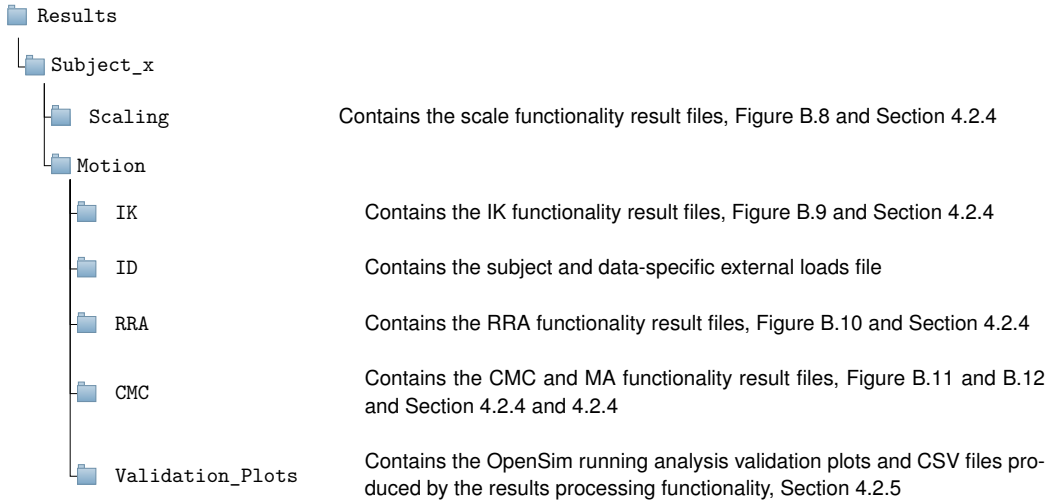

Figure B.6: Results folder structure generated by the processing pipeline

Stellenbosch University https://scholar.sun.ac.za

B.2 Residual Analysis Signal Filtering Technique

Figure B.7 illustrates the theory behind the Winter (2009) residual analysis technique used for determining the optimal cut-off frequency for filtering marker trajectories in the data processing portion of the developed pipeline, Section 4.2.2.

The plot shows the residual signal between a filtered and unfiltered signal as a function of the filter cut-off frequency (f_c). The dashed line *ad* represents the best, linear estimate of the noise residual. The optimal cut-off frequency ($f_c^{'}$) for the data signal is selected with the best suited compromise of signal distortion and the amount of noise allowed to pass through the filter. This frequency is determined by the intersection of horizontal line, stemming from the Y axis intersection of line *ad*, and the residual signal. The vertical line *bc* illustrates the estimated amount of noise that will pass through the filter with $f_c = f_c^{'}$ (Winter, 2009).

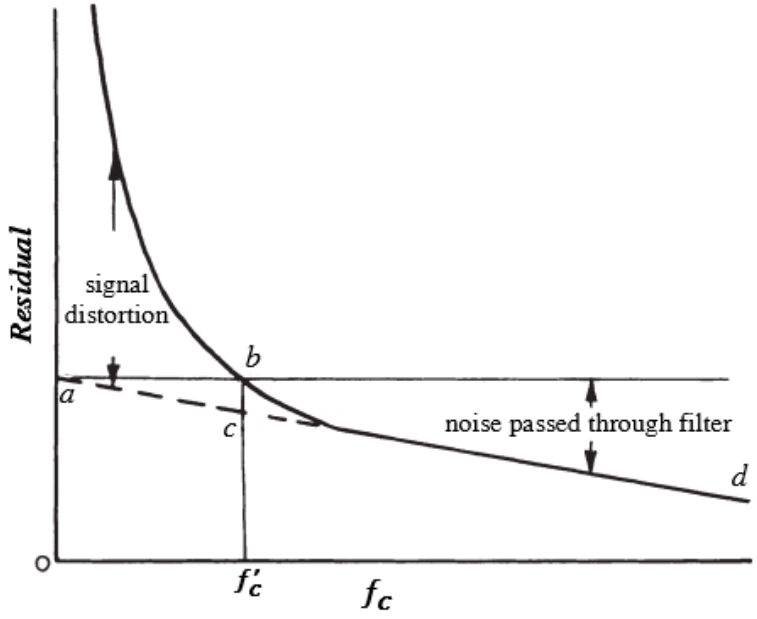

Figure B.7: Illustration of the theory behind the Winter (2009) residual analysis used for filtering marker trajectories. The plot shows the residual signal between a filtered and unfiltered signal as a function of the filter cut-off frequency (f_c). The optimal cut-off frequency ($f_c^{'}$) is defined as the frequency at which the intersection of horizontal line (0 gradient line from the Y axis intersection of the line *ad*) and the residual signal occurs (Winter, 2009)

B.3 Process Flowcharts

Figures B.8 to B.12 illustrate the input-output workflows for each of the OpenSim analysis functionality implemented in the Python processing pipeline.

Stellenbosch University https://scholar.sun.ac.za

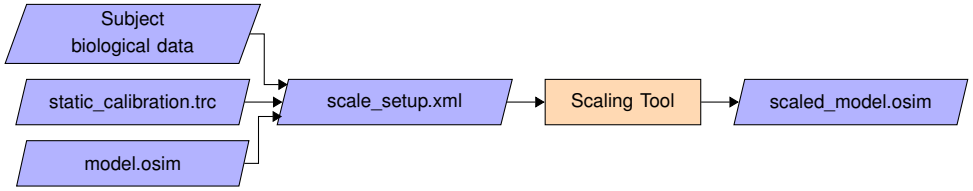

Figure B.8: Input-output flowchart of the OpenSim Scaling process implemented in the developed Python processing pipeline

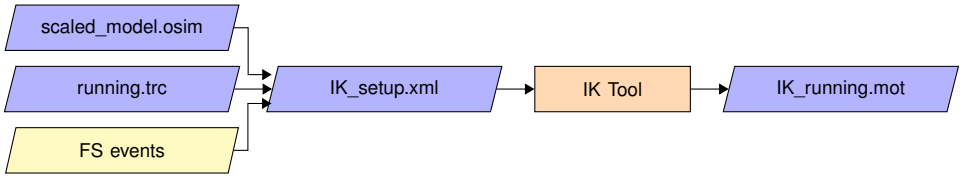

Figure B.9: Input-output flowchart of the OpenSim IK process implemented in the developed Python processing pipeline

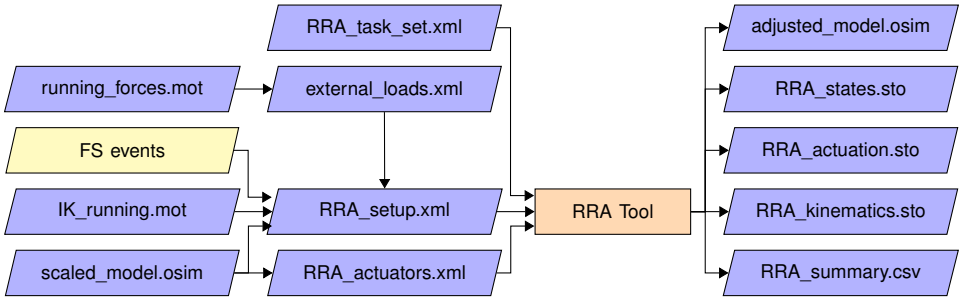

Figure B.10: Input-output flowchart of the OpenSim RRA process implemented in the developed Python processing pipeline

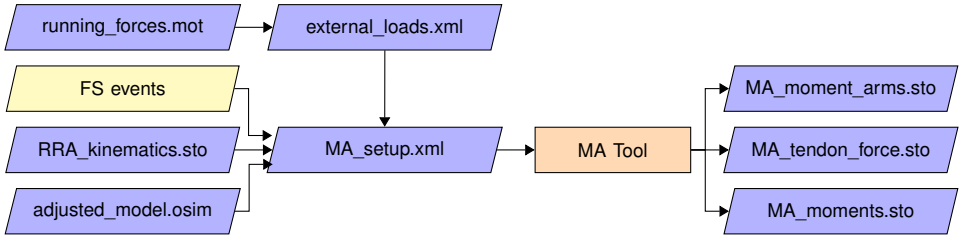

Figure B.11: Input-output flowchart of the Muscle Analysis process implemented in the developed Python processing pipeline. Due to the fact that the MA Tool is run in conjunction with the CMC Tool, the MA setup file is fed into the CMC setup file, in Figure B.12

Stellenbosch University https://scholar.sun.ac.za

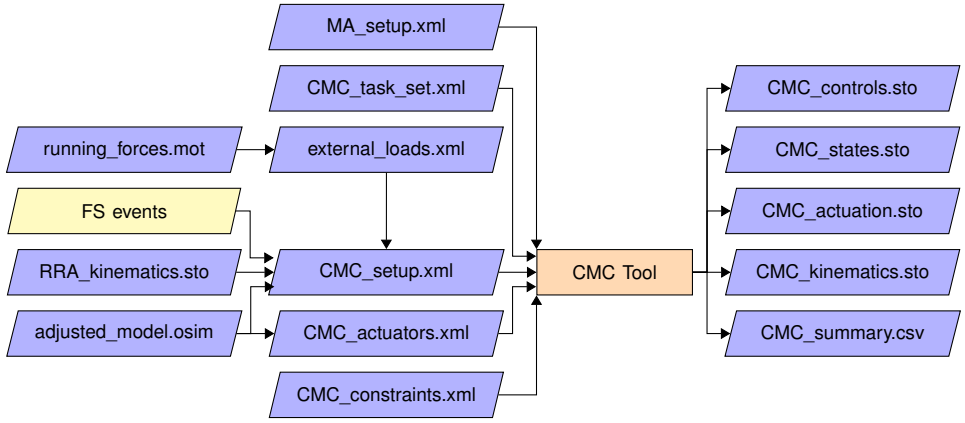

Figure B.12: Input-output flowchart of the OpenSim CMC process implemented in the developed Python processing pipeline

B.4 Sample Output Figures

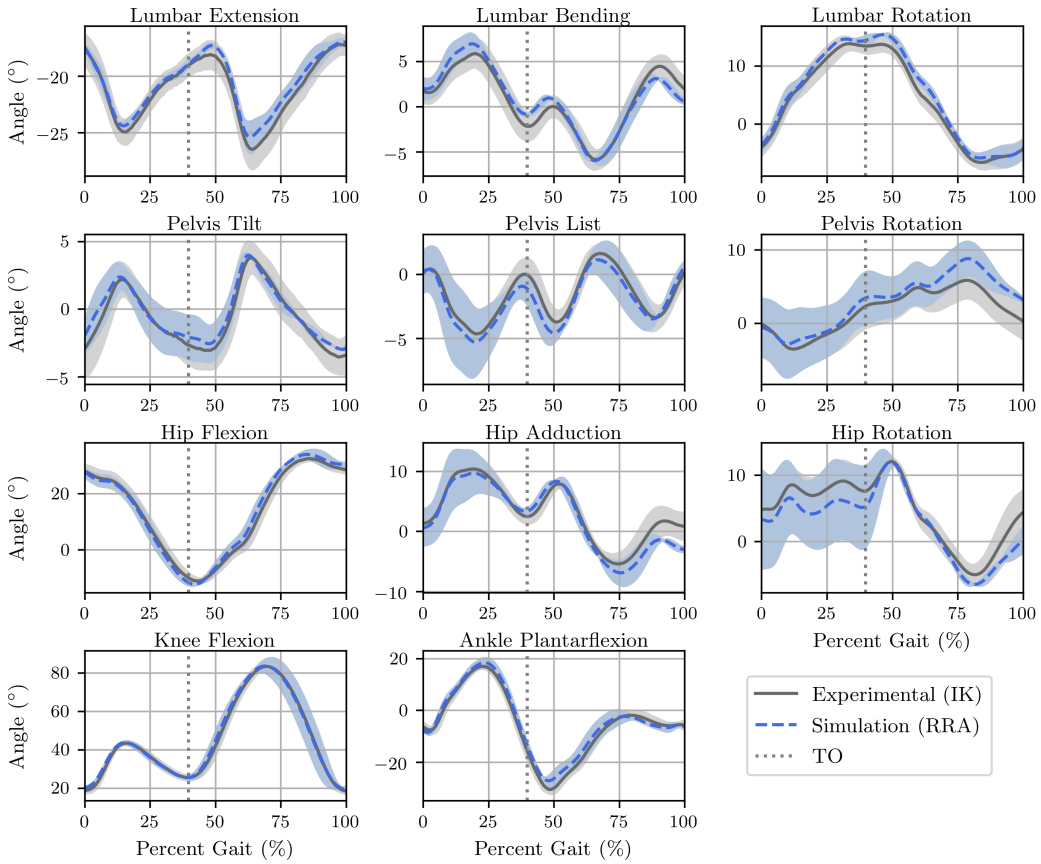

Figure B.13: Example plot of the IK (grey) and RRA (blue) kinematics results

Stellenbosch University https://scholar.sun.ac.za

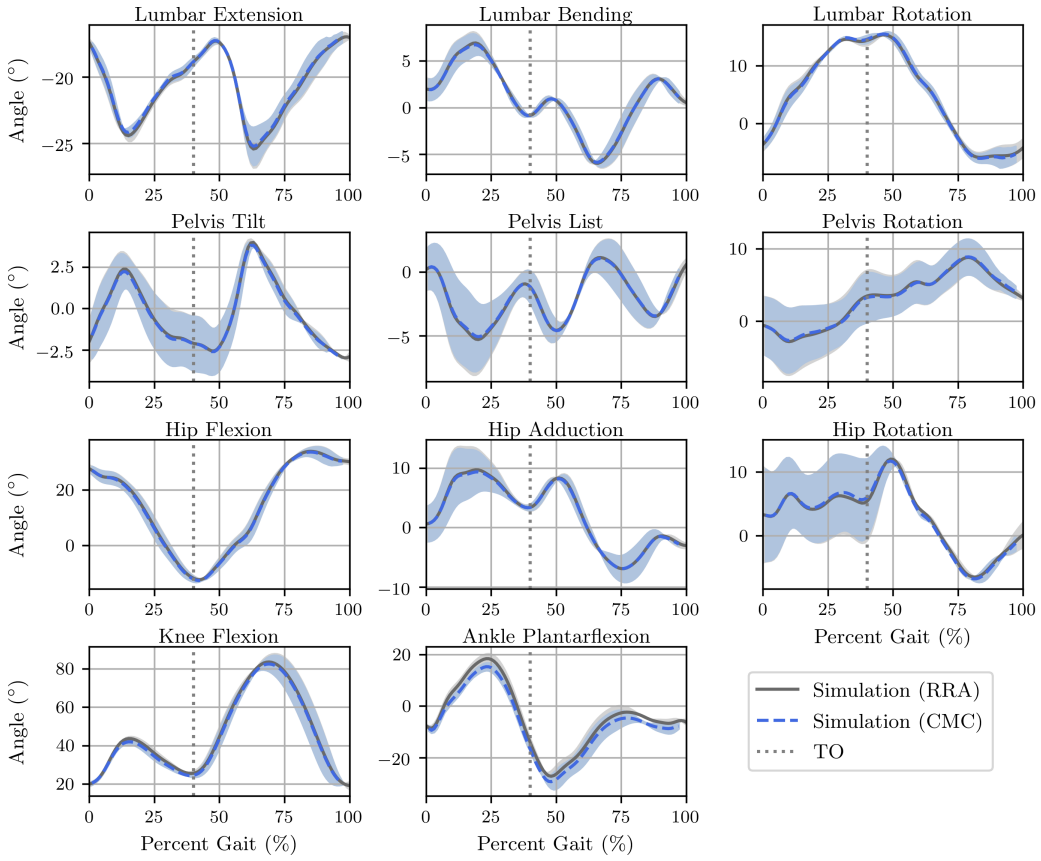

Figure B.14: Example plot of the RRA (grey) and CMC (blue) kinematics results

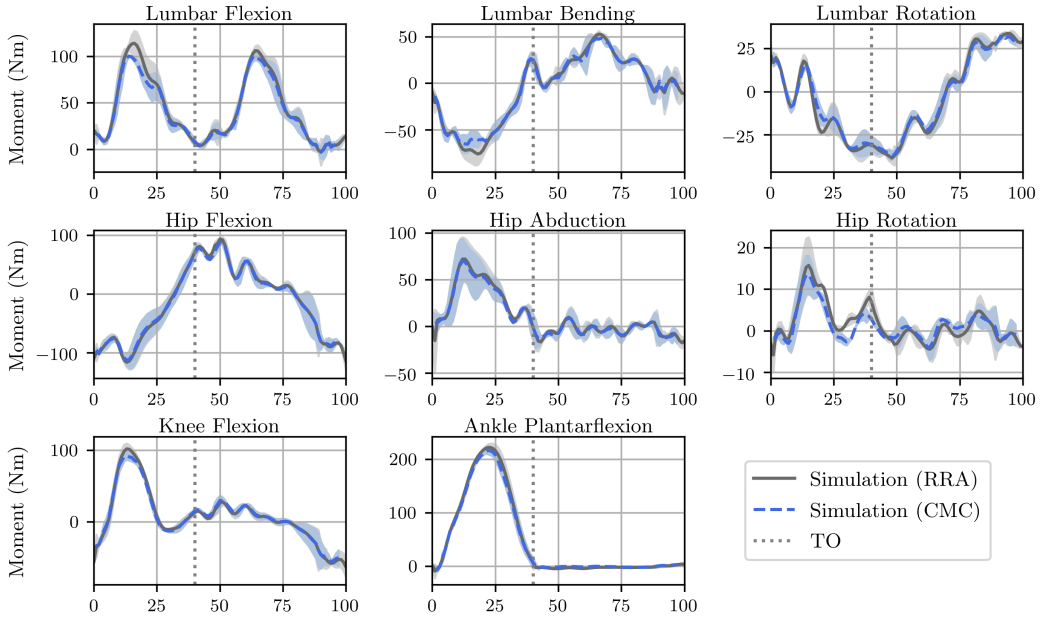

Figure B.15: Example plot of the RRA (grey) and CMC (blue) joint moment results

Stellenbosch University https://scholar.sun.ac.za

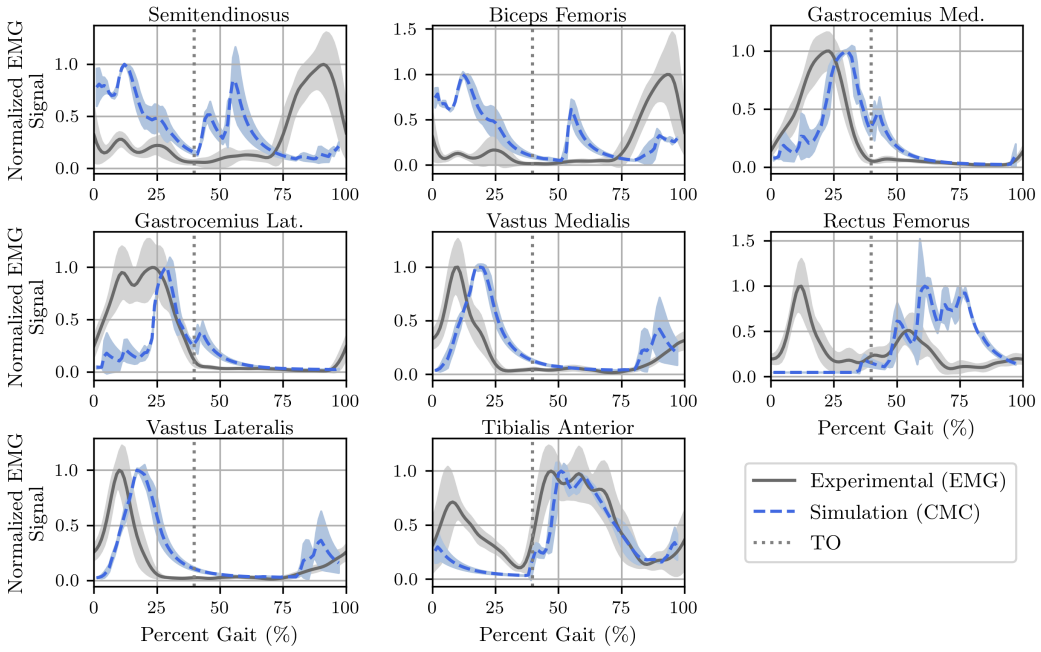

Figure B.16: Example plot of the muscle activation signal results. The experimental EMG (grey) and CMC (blue) muscle activation signals are compared in an effort to identify if the CMC process has yielded reliable results which match those experienced in reality

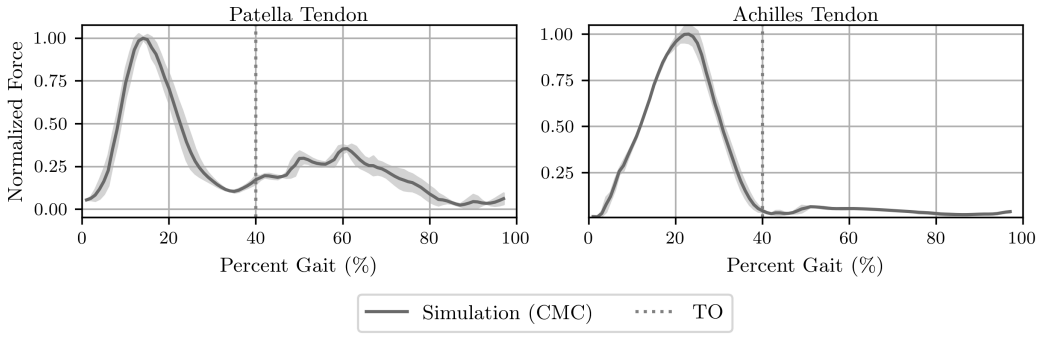

Figure B.17: Example plot of the Achilles and patella tendon force results

Stellenbosch University https://scholar.sun.ac.za

C OpenSim Results

The following appendix presents the developed processing pipeline's OpenSim workflow results for Models 1, 2, 4, 5, and 6, as they were not discussed in Section 5.1. It is important to note, that like Section 5.1, only the results for the participants with a complete set of OpenSim results are presented.

C.1 Inverse Kinematics

Table C.1 presents the IK RMS errors and mean COD (R^2) for the hip, knee, and ankle joints of Models 1, 2, 4, 5, and 6 during level, incline, and decline running conditions.

Table C.1: RMS errors and mean coefficient of determination (R^2), acquired for Models 1, 2, 4, 5, and 6 during IK for level, incline, and decline running conditions

		Level		**Incline**		**Decline**	
Model	**Participant**	**IK RMS (cm)**	R^2	**IK RMS (cm)**	R^2	**IK RMS (cm)**	R^2
Model 1	1	1.76	0.97				
	2	1.63	0.9	1.68	0.99	1.75	0.95
	3	2.22	0.99			2.27	0.96
	4						
	5	1.84	0.97			1.72	
Model 2	1	1.76	0.97				
	2	1.63	0.9	1.68	0.99	1.75	0.95
	3	2.22	0.99			2.27	0.96
	4						
	5	1.84	0.96				
Model 4	1	1.76	0.97				
	2	1.63	0.9	1.68	0.99	1.75	0.98
	3	2.22	0.99			2.27	0.96
	4						
	5	1.84	0.92				

Stellenbosch University https://scholar.sun.ac.za

Model	Participant	Level		Incline		Decline	
		IK RMS (cm)	R^2	IK RMS (cm)	R^2	IK RMS (cm)	R^2
Model 5	1	1.76	0.97				
	2	1.63	0.9	1.68	0.99	1.75	0.95
	3	2.22	0.99			2.27	0.96
	4						
	5	1.84	0.96				
Model 6	1	1.76	0.97				
	2	1.63	0.9	1.68	0.99	1.75	0.95
	3	2.22	0.99			2.27	0.95
	4						
	5	1.84	0.97				

* R^2 is calculated in terms of the Hamner *et al.* (2010) model ($R^2_{baseline} = 1.0$)

** Blank table cells indicate no available data for the respective project participant and running condition, as the processing pipeline failed to successfully complete the entire OpenSim running gait analysis workflow implemented

C.2 Residual Reduction Analysis

Tables C.2 to C.4 illustrate the RRA residual force and torque vector components (X, Y, and Z) observed for the Models 1, 2, 4, 5, and 6 during level, incline, and decline running conditions. Table 4.2 defines the "good", "okay", and "bad" error performance categories for RRA residuals, and are represented by green, yellow, and red cell colours in Tables C.2 to C.4, respectively.

Table C.2: Maximum X, Y, and Z components of the residual forces and torques observed for Models 1, 2, 4, 5, and 6 during RRA for level running conditions

Model	Participant	Residuals (% BW)					
		F_X	F_Y	F_Z	M_X	M_Y	M_Z
Model 1	1	0.7	0.22	0.23	2.38	4.21	3.62
	2	0.45	0.11	0.14	1.67	3.69	2.43
	3	0.02	0.03	0.04	0.78	0.94	0.31
	5	0.04	0	0.08	0.69	1.55	0.42
Model 2	1	0.7	0.22	0.23	2.38	4.21	3.62
	2	0.45	0.11	0.14	1.67	3.69	2.43
	3	0.01	0.02	0.05	0.78	0.99	0.35
	5	0.02	0.03	0.1	1.42	2.13	0.59

Stellenbosch University https://scholar.sun.ac.za

Model	Participant	Residuals (% BW)					
		F_X	F_Y	F_Z	M_X	M_Y	M_Z
Model 4	1	0.75	0.14	0.23	1.94	4.19	3.33
	2	0.45	0.11	0.14	1.67	3.69	2.43
	3	0.02	0.03	0.05	0.69	0.85	0.32
	5	0.05	0.02	0.06	2.26	2.23	1.4
Model 5	1	0.7	0.22	0.23	2.38	4.21	3.62
	2	0.45	0.11	0.14	1.67	3.69	2.43
	3	0.01	0.02	0.05	0.78	0.99	0.35
	5	0.02	0.03	0.1	1.42	2.13	0.59
Model 6	1	0.7	0.22	0.23	2.38	4.21	3.62
	2	0.45	0.11	0.14	1.67	3.69	2.43
	3	0.01	0.02	0.05	0.78	0.99	0.35
	5	0.04	0	0.08	0.69	1.55	0.42

Table C.3: Maximum X, Y, and Z components of the residual forces and torques observed for Models 1, 2, 4, 5, and 6 during RRA for incline running conditions

Model	Participant	Residuals (% BW)					
		F_X	F_Y	F_Z	M_X	M_Y	M_Z
Model 1	2	0.04	0.14	0.33	2.68	3.79	1.99
Model 2	2	0.03	0.02	0.22	0.7	2.61	1.13
Model 4	2	0.04	0.14	0.33	2.68	3.79	1.99
Model 5	2	0.03	0.02	0.22	0.7	2.61	1.13
Model 6	2	0.04	0.14	0.33	2.68	3.79	1.99

Table C.4: Maximum X, Y, and Z components of the residual forces and torques observed for Models 1, 2, 4, 5, and 6 during RRA for decline running conditions

Model	Participant	Residuals (% BW)					
		F_X	F_Y	F_Z	M_X	M_Y	M_Z
Model 1	2	0.02	0.01	0.06	0.8	1.77	0.73
	3	0.04	0.01	0.03	0.56	2.76	1.38
Model 2	2	0.02	0.01	0.06	0.8	1.77	0.73
	3	0.01	0.01	0.03	0.75	2.67	0.67

Stellenbosch University https://scholar.sun.ac.za

Model	Participant	Residuals (% BW)					
		F_X	F_Y	F_Z	M_X	M_Y	M_Z
Model 4	2	0.06	0.01	0.24	0.33	2.09	0.14
	3	0.04	0.01	0.03	0.56	2.76	1.38
Model 5	2	0.02	0.01	0.06	0.8	1.77	0.73
	3	0.04	0.01	0.03	0.56	2.76	1.38
Model 6	2	0.02	0.01	0.06	0.8	1.77	0.73
	3	0.04	0.01	0.03	0.66	2.86	1.41

C.3 Computed Muscle Control

Tables C.5 to C.7 illustrate the CMC residual force and torque vector components (X, Y, and Z) observed for the Models 1, 2, 4, 5, and 6 during level, incline, and decline running conditions, respectively. Table 4.3 defines the “good”, “okay”, and “bad” error performance categories for CMC residuals, and are represented by green, yellow, and red cell colours in Tables C.5 to C.7, respectively.

Table C.5: The maximum X, Y, and Z component values of the residual forces and torques observed for Models 1, 2, 4, 5, and 6 during CMC for level running

Model	Participant	Residuals (% BW)					
		F_X	F_Y	F_Z	M_X	M_Y	M_Z
Model 1	1	1.35	1.29	1.42	1.57	3.65	4.39
	2	0.84	1.12	1.87	1.38	3.3	2.83
	3	0.64	0.09	1.17	1.02	0.68	0.56
	5	0.62	3.12	1.78	1.56	1.66	0.63
Model 2	1	1.72	1.43	1.29	1.63	3.67	4.35
	2	0.88	1.16	1.92	1.36	3.28	2.71
	3	1.78	0.8	2.3	2.98	1.24	0.39
	5	1.27	0.26	2.14	2.68	2.4	0.45
Model 4	1	1.7	1.87	1.75	3.14	3.62	3.77
	2	0.88	1.12	2.04	1.37	3.32	2.69
	3	0.63	0.15	1.37	1.06	0.7	0.61
	5	2.88	23.6	1.29	2.48	2.18	1.8
Model 5	1	1.62	1.36	1.32	1.62	3.68	4.36
	2	0.9	1.12	2.3	1.34	3.25	2.75
	3	1.79	0.8	2.27	2.98	1.23	0.39
	5	1.32	0.29	2.27	2.65	2.39	0.46

Stellenbosch University https://scholar.sun.ac.za

Model	Participant	Residuals (% BW)					
		F_X	F_Y	F_Z	M_X	M_Y	M_Z
Model 6	1	1.63	1.41	1.35	1.63	3.68	4.36
	2	0.9	1.1	2.02	1.35	3.28	2.67
	3	5.77	0.85	2.32	2.95	1.24	0.4
	5	0.75	2.88	1.93	1.64	1.62	0.61

Table C.6: The maximum X, Y, and Z component values of the residual forces and torques observed for Models 1, 2, 4, 5, and 6 during CMC for incline running

Model	Participant	Residuals (% BW)					
		F_X	F_Y	F_Z	M_X	M_Y	M_Z
Model 1	2	0.98	1.22	1.98	2.53	3.31	2.94
Model 2	2	0.82	1.26	2.15	0.7	2.0	2.0
Model 4	2	0.86	1.17	1.96	2.58	3.29	2.91
Model 5	2	0.76	1.18	2.16	0.74	1.99	2.03
Model 6	2	0.91	1.22	2.19	2.61	3.29	2.99

Table C.7: The maximum X, Y, and Z component values of the residual forces and torques observed for Models 1, 2, 4, 5, and 6 during CMC for decline running

Model	Participant	Residuals (% BW)					
		F_X	F_Y	F_Z	M_X	M_Y	M_Z
Model 1	2	1.29	12.0	1.73	1.09	1.53	0.68
	3	2.11	0.73	5.09	4.12	3.04	1.68
Model 2	2	1.23	2.69	0.69	1.03	1.54	0.51
	3	1.18	0.25	0.99	1.18	2.58	0.91
Model 4	2	2.05	5.57	1.1	1.0	1.88	0.19
	3	1.96	0.7	5.14	4.24	3.04	1.68
Model 5	2	1.25	2.63	0.73	1.08	1.53	0.5
	3	2.36	0.71	5.65	4.97	3.1	1.99
Model 6	2	1.23	11.8	1.65	0.98	1.54	0.53
	3	2.54	0.64	5.25	3.99	3.17	1.76

Stellenbosch University https://scholar.sun.ac.za

C.4 Kinematics Comparison

Table C.8 compares the mean COD (R^2) for the resultant hip, knee, ankle joint angles observed during RRA and IK for level, incline, and decline running conditions. Similarly, Table C.9 compares the mean COD observed during RRA and CMC for the resultant hip, knee, ankle joint angles.

Table C.8: Comparison of the mean coefficient of determination (R^2) for the net hip, knee, ankle joint angles, acquired during IK and RRA for level, incline, and decline running conditions

		R^2		
Model	**Participant**	**Level**	**Incline**	**Decline**
Hamner *et al.* (2010) model	1	1.0	1.0	
	2	1.0	1.0	0.99
	3	0.99		0.92
	4		1.0	
	5	1.0		1.0
Model 1	1	1.0		
	2	1.0	1.0	0.99
	3	1.0		0.99
	4			
	5	1.0		
Model 2	1	1.0		
	2	1.0	1.0	0.99
	3	1.0		1.0
	4			
	5	1.0		
Model 3	1	1.0		
	2	1.0	1.0	0.99
	3	1.0		0.99
	4			
	5	1.0		
Model 4	1	1.0		
	2	1.0	1.0	0.99
	3	1.0		0.99
	4			
	5	1.0		

Stellenbosch University https://scholar.sun.ac.za

		R^2		
Model	**Participant**	**Level**	**Incline**	**Decline**
Model 5	1	1.0		
	2	1.0	1.0	0.99
	3	1.0		0.99
	4			
	5	1.0		
Model 6	1	1.0		
	2	1.0	1.0	0.99
	3	1.0		0.99
	4			
	5	1.0		

* R^2 is calculated in terms of the corresponding IK R^2 results documented in Tables 5.2 and C.1 ($R^2_{IK} = 1.0$)

** Blank table cells indicate no available data for the respective project participant and running condition, as the processing pipeline failed to successfully complete the entire OpenSim running gait analysis workflow implemented

Table C.9: Comparison of the mean coefficient of determination (R^2) for the net hip, knee, ankle joint angles, acquired during RRA and CMC for level, incline, and decline running conditions

		R^2		
Model	**Participant**	**Level**	**Incline**	**Decline**
Hamner *et al.* (2010) model	1	1.0	1.0	
	2	0.99	1.0	1.0
	3	1.0		0.92
	4		1.0	
	5	1.0		1.0
Model 1	1	1.0		
	2	0.99	1.0	0.99
	3	1.0		1.0
	4			
	5	1.0		

Stellenbosch University https://scholar.sun.ac.za

		R^2		
Model	**Participant**	**Level**	**Incline**	**Decline**
Model 2	1	1.0		
	2	0.99	1.0	0.99
	3	1.0		1.0
	4			
	5	1.0		
Model 3	1	1.0		
	2	0.99	1.0	0.99
	3	1.0		1.0
	4			
	5	1.0		
Model 4	1	1.0		
	2	0.99	1.0	0.99
	3	1.0		1.0
	4			
	5	1.0		
Model 5	1	1.0		
	2	0.99	1.0	0.99
	3	1.0		1.0
	4			
	5	1.0		
Model 6	1	1.0		
	2	0.99	1.0	0.99
	3	1.0		0.99
	4			
	5	1.0		

* R^2 is calculated in terms of the corresponding RRA R^2 results documented in Table C.8 ($R^2_{RRA} = 1.0$)

** Blank table cells indicate no available data for the respective project participant and running condition, as the processing pipeline failed to successfully complete the entire OpenSim running gait analysis workflow implemented

C.5 Tendon Force Profiles

Tables C.10 and C.11 summarize the normalized peak tendon forces for the patella and Achilles tendons during the analysed running conditions, respectively. It is important to note that the peak tendon forces observed during incline and decline running conditions are normalized according to the maximum tendon force experienced during level running conditions.

Stellenbosch University https://scholar.sun.ac.za

Table C.10: Normalized *in-silico* peak patella tendon forces

Model	Participant	Normalized Tendon Force (F^T)		
		Level	**Incline**	**Decline**
Hamner *et al.* (2010) model	1	1.0	0.92	
	2	1.0	0.97	1.36
	3	1.0		1.11
	4			
	5	1.0		1.1
Model 1	1			
	2	1.0	0.26	1.12
	3	1.0		1.14
	4			
	5			
Model 2	1	1.0		
	2	1.0	0.85	1.25
	3	1.0		1.28
	4			
	5	1.0		
Model 3	1	1.0		
	2	1.0	0.86	1.35
	3	1.0		1.0
	4			
	5	1.0		
Model 4	1	1.0		
	2	1.0	0.26	1.03
	3	1.0		1.12
	4			
	5	1.0		
Model 5	1	1.0		
	2	1.0	0.84	1.25
	3	1.0		1.11
	4			
	5	1.0		

Stellenbosch University https://scholar.sun.ac.za

Model	Participant	Normalized Tendon Force (F^T)		
		Level	Incline	Decline
Model 6	1	1.0		
	2	1.0	0.84	1.27
	3	1.0		1.13
	4			
	5	1.0		

* Peak forces are computed as a percentage of the maximum tendon force experienced during level running conditions ($F^T_{level} = 1.0$)

** Blank table cells indicate no available data for the respective project participant and running condition, as the processing pipeline failed to successfully complete the entire OpenSim running gait analysis workflow implemented

Table C.11: Normalized *in-silico* peak Achilles tendon forces

Model	Participant	Normalized Tendon Force (F^T)		
		Level	Incline	Decline
Hamner *et al.* (2010) model	1	1.0	1.05	
	2	1.0	1.1	0.79
	3	1.0		0.84
	4			
	5	1.0		0.86
Model 1	1	1.0		
	2	1.0	1.11	0.8
	3	1.0		0.84
	4			
	5	1.0		
Model 2	1	1.0		
	2	1.0	1.1	0.81
	3	1.0		0.85
	4			
	5	1.0		
Model 3	1	1.0		
	2	1.0	1.14	0.95
	3	1.0		0.82
	4			
	5	1.0		

Stellenbosch University https://scholar.sun.ac.za

Model	Participant	Normalized Tendon Force (F^T)		
		Level	Incline	Decline
Model 4	1	1.0		
	2	1.0	1.12	0.87
	3	1.0		0.81
	4			
	5	1.0		
Model 5	1	1.0		
	2	1.0	1.1	0.81
	3	1.0		0.85
	4			
	5	1.0		
Model 6	1	1.0		
	2	1.0	1.14	0.81
	3	1.0		0.84
	4			
	5	1.0		

* Peak forces are computed as a percentage of the maximum tendon force experienced during level running conditions ($F^T_{level} = 1.0$)

** Blank table cells indicate no available data for the respective project participant and running condition, as the processing pipeline failed to successfully complete the entire OpenSim running gait analysis workflow implemented

Stellenbosch University https://scholar.sun.ac.za

D Model Sensitivity Analysis

The following appendix documents the model sensitivity analysis (two-sample t-test) results obtained for project participants which were not discussed in Section 5.2.

D.1 Patella Tendon

Figures D.2 to D.4 illustrate the sensitivity analysis results for the patella tendon implantations during level running conditions for Participants 1, 3, and 5. Similarly, Figure D.5 illustrates the sensitivity analysis results for the patella tendon implantations during decline running conditions for Participant 3. Each of the figures are formatted in the same manner as Figure 5.5, in Section 5.2.1. The legend for the mean and SD clouds in the proceeding figures is indicated below, Figure D.1.

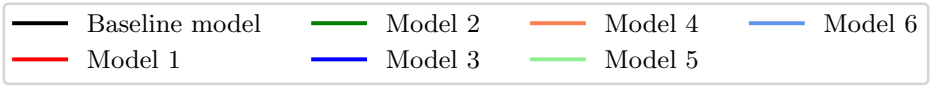

Figure D.1: Plot legend for the patella tendon mean and SD clouds illustrated in Appendix D

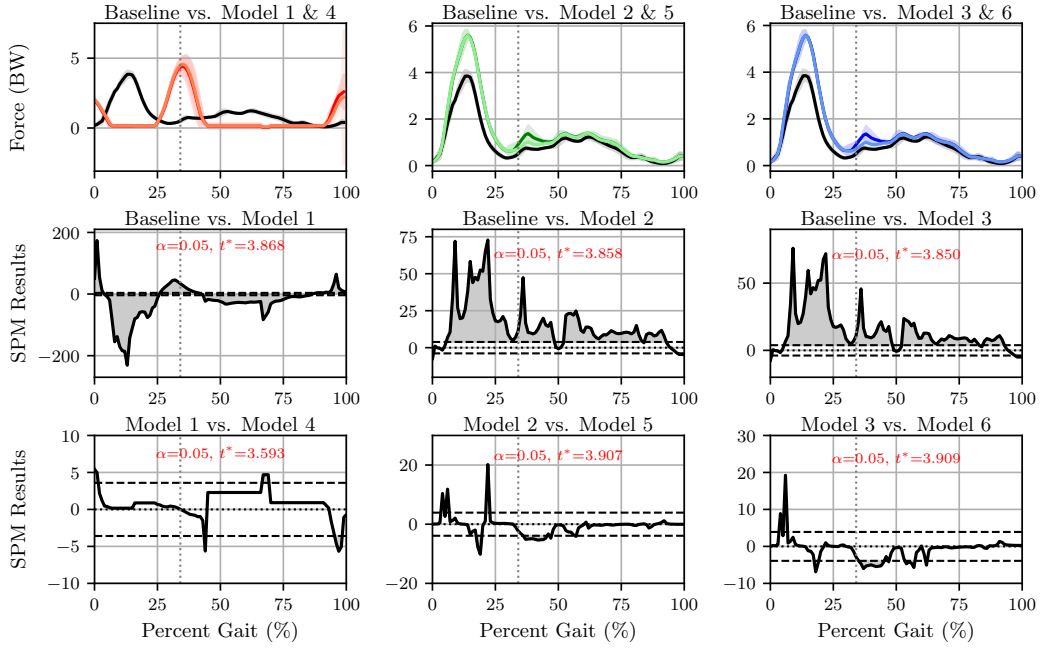

Figure D.2: Two-sample t-test results of the *in-silico* patella tendon profiles for Participant 1 during level running conditions

Stellenbosch University https://scholar.sun.ac.za

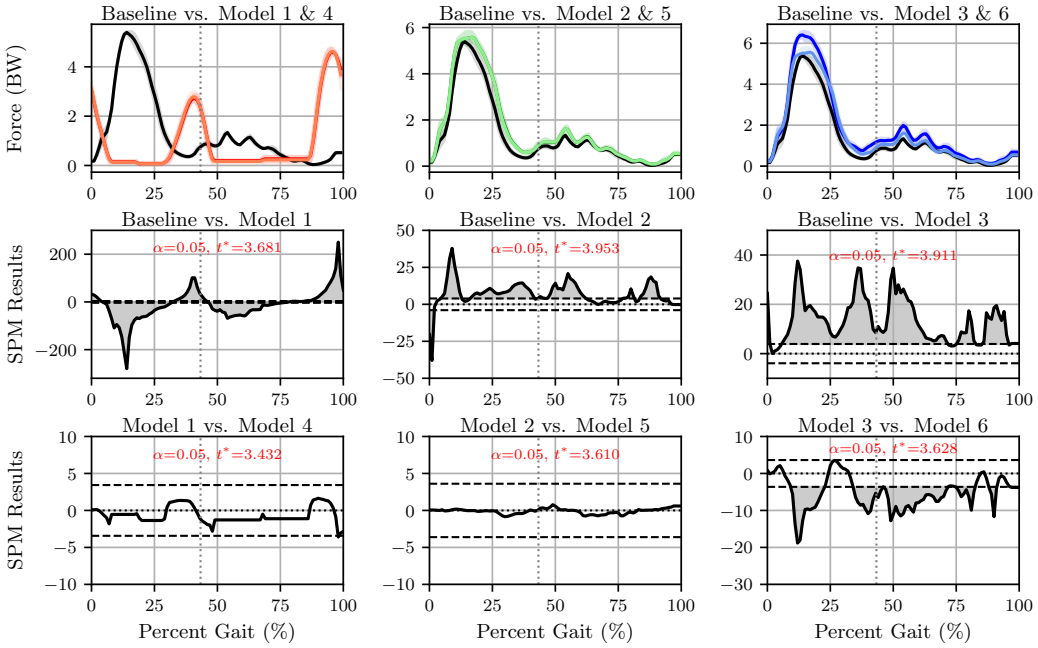

Figure D.3: Two-sample t-test results of the *in-silico* patella tendon profiles for Participant 3 during level running conditions

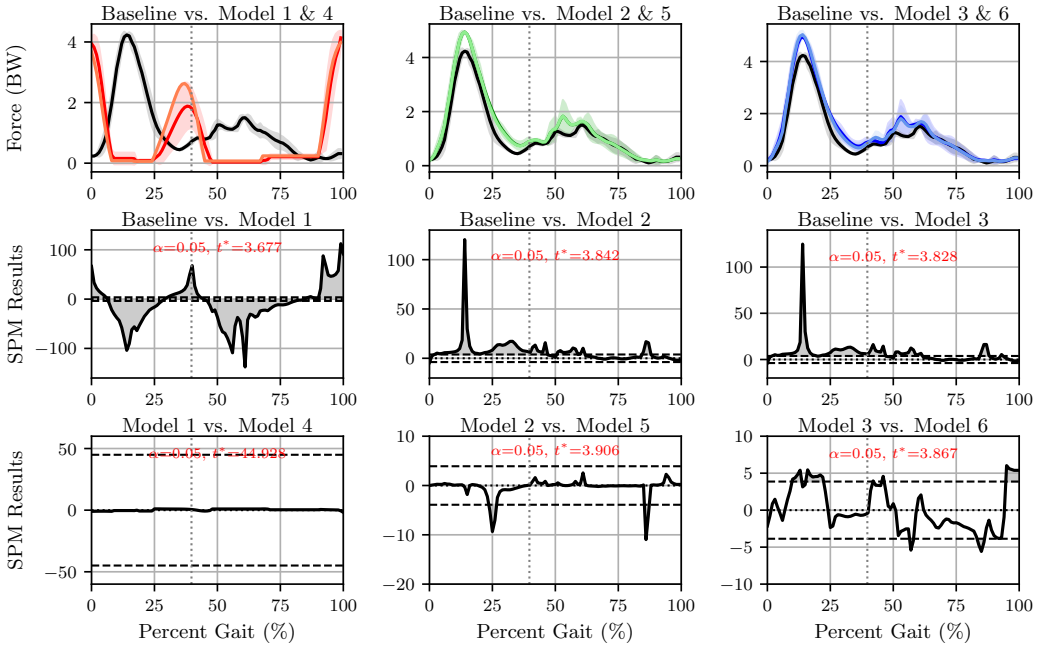

Figure D.4: Two-sample t-test results of the *in-silico* patella tendon profiles for Participant 5 during level running conditions

Stellenbosch University https://scholar.sun.ac.za

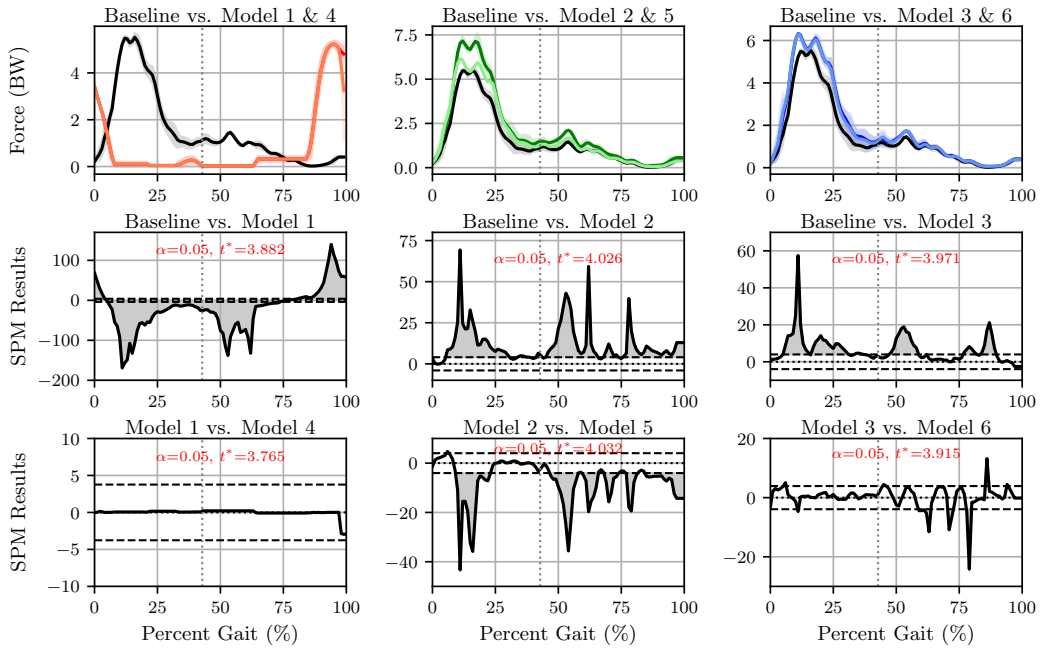

Figure D.5: Two-sample t-test results of the *in-silico* patella tendon profiles for Participant 3 during decline running conditions

D.2 Achilles Tendon

Figures D.7 to D.9 illustrate the sensitivity analysis results for the Achilles tendon implantations during level running conditions for Participants 1, 3, and 5. Similarly, Figure D.10 illustrates the sensitivity analysis results for the Achilles tendon implantations during decline running conditions for Participant 3. Each of the figures are formatted in the same manner as Figure 5.5, in Section 5.2.1. The legend for the mean and SD clouds in the proceeding figures is indicated below, Figure D.6.

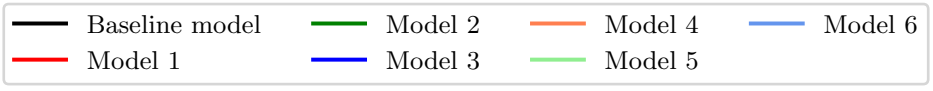

Figure D.6: Plot legend for the Achilles tendon mean and SD clouds illustrated in Appendix D

Stellenbosch University https://scholar.sun.ac.za

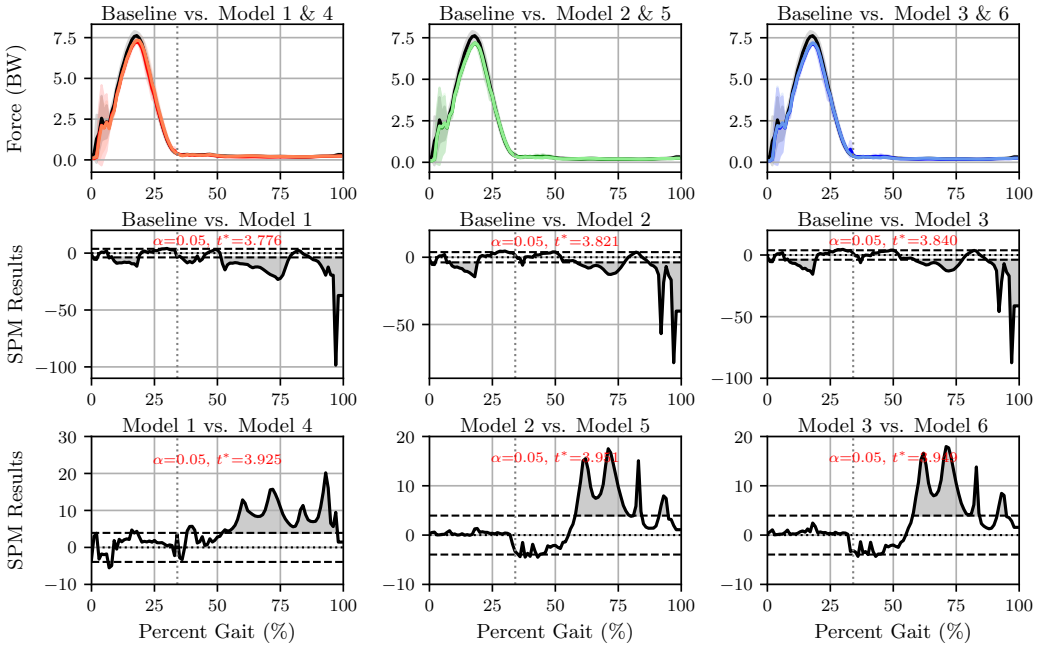

Figure D.7: Two-sample t-test results of the *in-silico* Achilles tendon profiles for Participant 1 during level running conditions

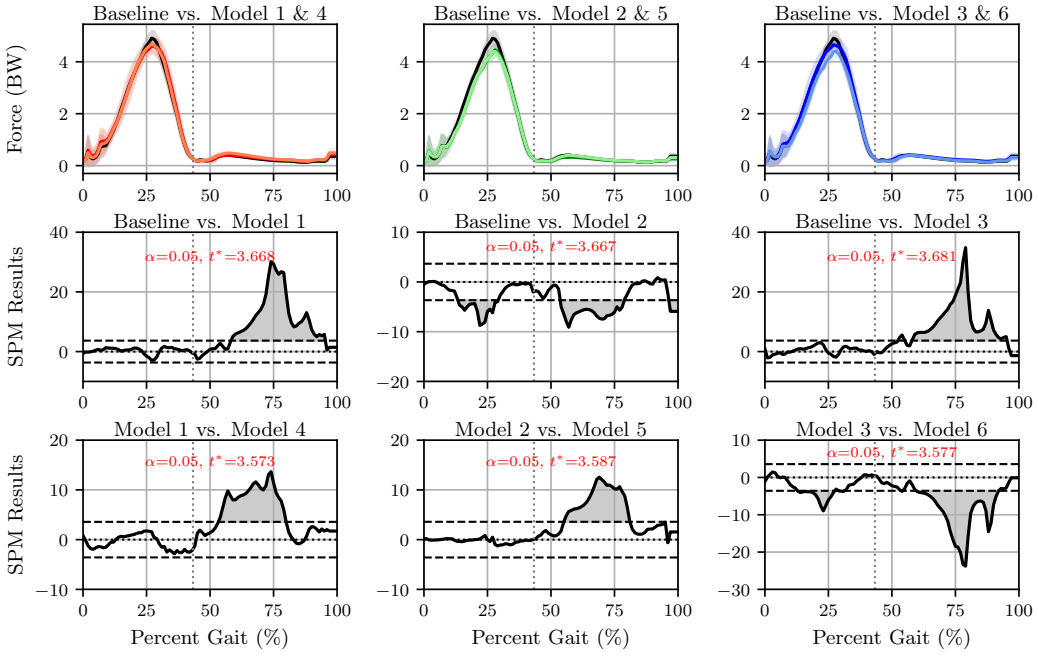

Figure D.8: Two-sample t-test results of the *in-silico* Achilles tendon profiles for Participant 3 during level running conditions

Stellenbosch University https://scholar.sun.ac.za

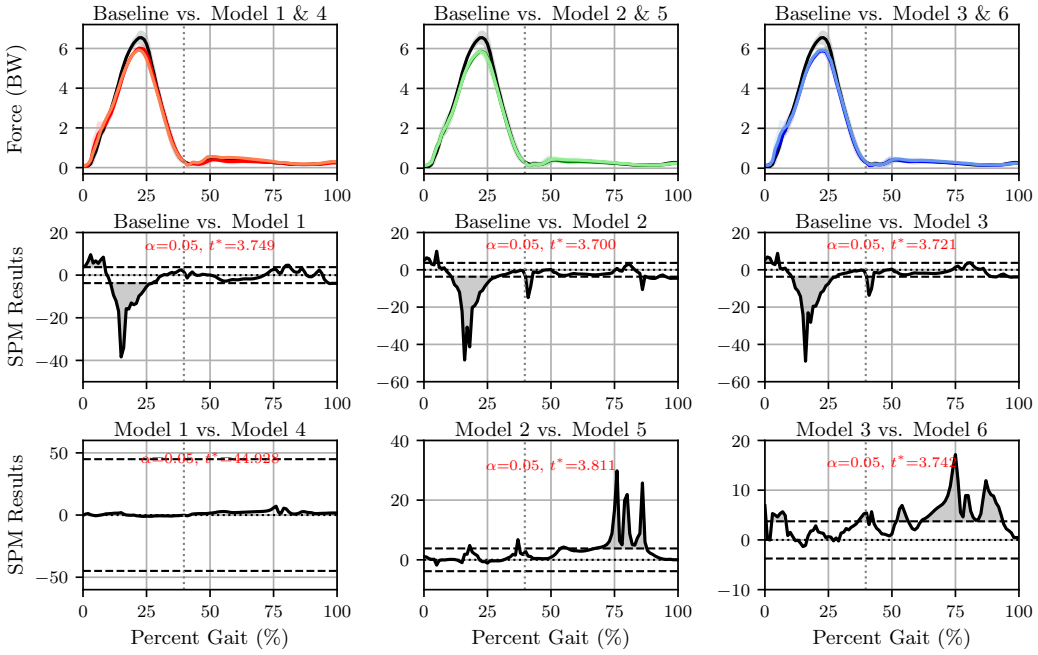

Figure D.9: Two-sample t-test results of the *in-silico* Achilles tendon profiles for Participant 5 during level running conditions

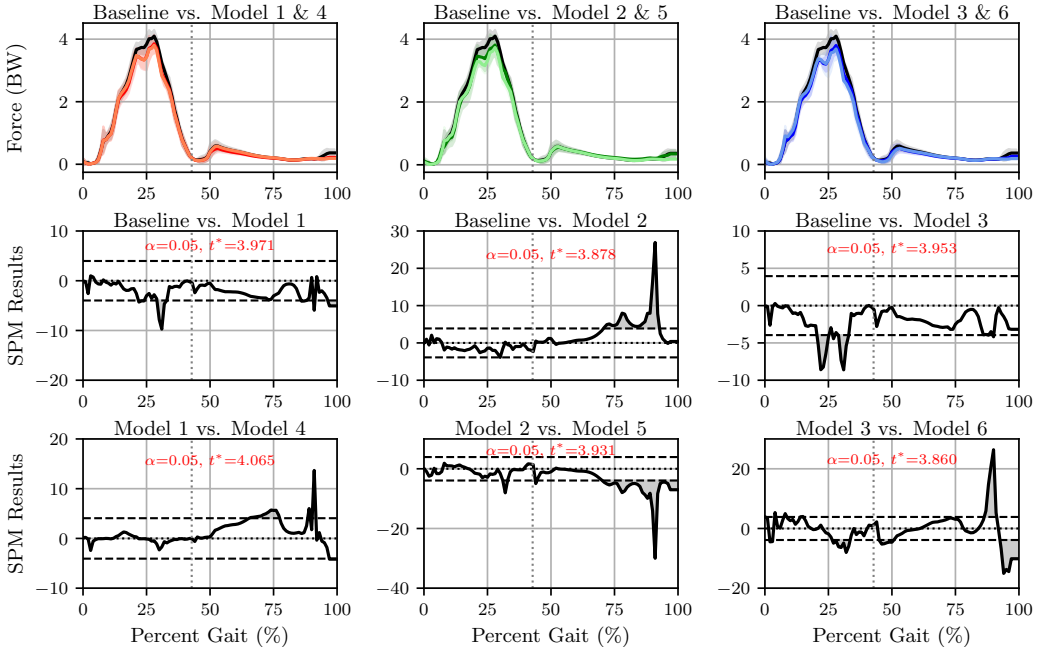

Figure D.10: Two-sample t-test results of the *in-silico* Achilles tendon profiles for Participant 3 during decline running conditions

Stellenbosch University https://scholar.sun.ac.za

E Independent Trend Analysis

The following appendix documents the results obtained from the independent trend analysis conducted between the normalized *in-vivo* and *in-silico* Achilles and patella tendon force profiles. The appendix focuses specifically on Models 1, 2, 4, and 5 as they were not discussed in Section 5.3.

E.1 Patella Tendon

The normalized *in-vivo* and *in-silico* loading profiles for the patella tendon during level, incline, and decline running conditions are illustrated in Figures E.1 to E.3. The figures take on the same format as those presented in the Section 5.3.1.

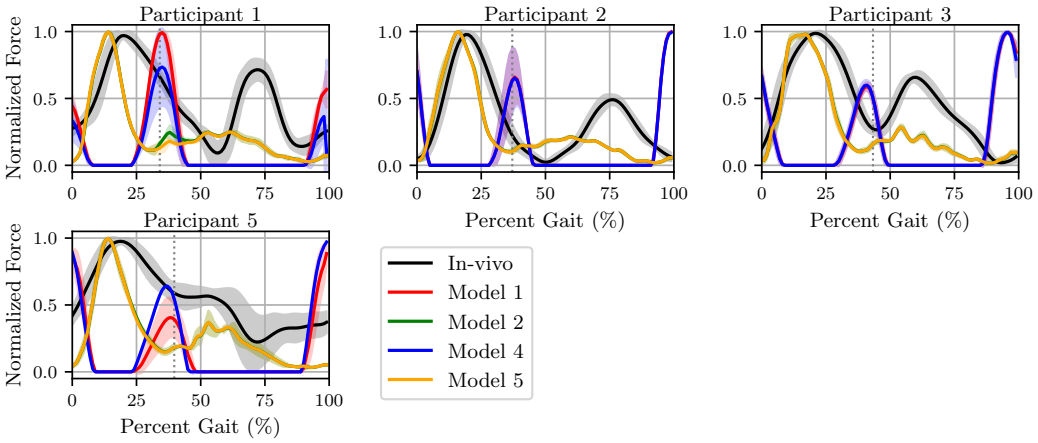

Figure E.1: Trend comparison between the *in-vivo* (black) and estimated patella tendon force observed for Models 1, 2, 4, and 5 during level running conditions

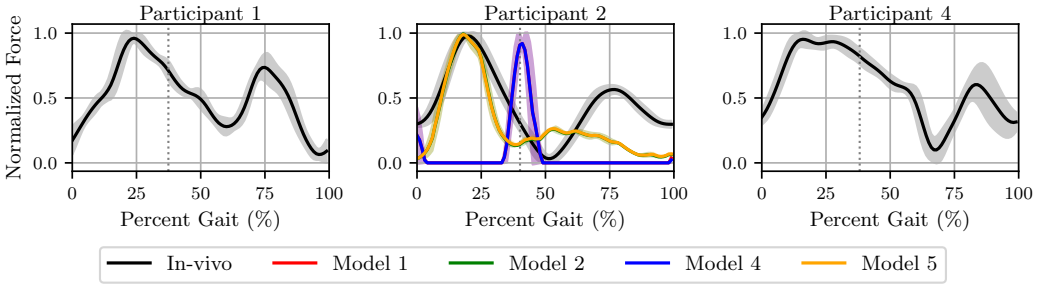

Figure E.2: Trend comparison between the *in-vivo* and estimated patella tendon force observed for Models 1, 2, 4, and 5 during incline running conditions. Notably, Participant 2 is the only participant with results for the presented modified models

Stellenbosch University https://scholar.sun.ac.za

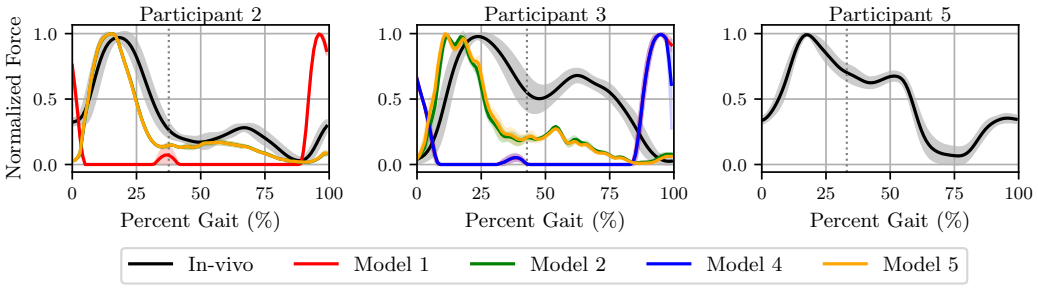

Figure E.3: Trend comparison between the *in-vivo* and estimated patella tendon force observed for Models 1, 2, 4, and 5 during decline running conditions. Notably, Participant 2 and 3 are the only participants with results for the presented modified models

Table E.1 presents the COD (R^2) observed for the patella tendon during the investigated running conditions, where the datum COD value is selected as the *in-vivo* patella tendon force for the respective participants and running conditions.

Table E.1: Coefficient of determination (R^2) observed for the estimated patella tendon forces of Models 1, 2, 4, and 5 during level, incline, and decline running

		R^2		
Model	**Participant**	**Level**	**Incline**	**Decline**
Model 1	1	0.01		
	2	0.13	0.06	0.04
	3	0.11		0.05
	4			
	5	0.02		
Model 2	1	0.21		
	2	0.58	0.58	0.84
	3	0.65		0.26
	4			
	5	0.62		
Model 4	1	0.02		
	2	0.13	0.06	0.04
	3	0.11		0.07
	4			
	5	0.01		

Stellenbosch University https://scholar.sun.ac.za

Model	Participant	R^2		
		Level	Incline	Decline
Model 5	1	0.2		
	2	0.57	0.58	0.83
	3	0.65		0.25
	4			
	5	0.61		

* R^2 is calculated in terms of the *in-vivo* patella tendon loading profiles (Groeneveld, 2020) for the respective running trials ($R^2_{in\text{-}vivo}$ = 1.0)

** Blank table cells indicate no available data for the respective project participant and running condition, as the processing pipeline failed to successfully complete the entire OpenSim running gait analysis workflow implemented

E.2 Achilles Tendon

Given that Groeneveld (2020) was only able to quantify the *in-vivo* Achilles tendon load for Participant 2, the normalized *in-vivo* and *in-silico* loading profiles for the Achilles tendon during level, incline, and decline running conditions for Participant 2 are shown in Figure E.4. The figure takes on the same format as those presented in the Section 5.3.1.

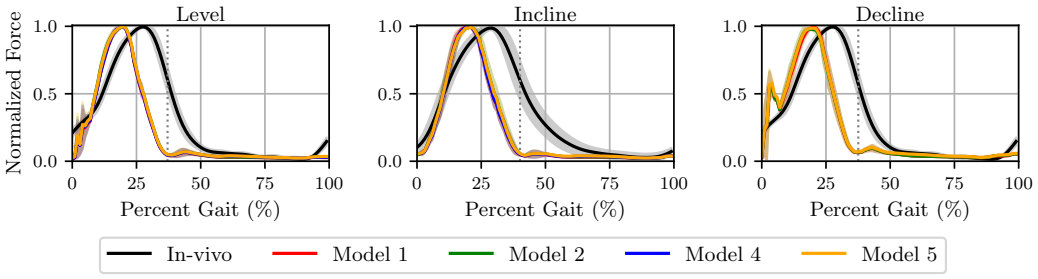

Figure E.4: Trend comparison between the *in-vivo* and estimated Achilles tendon force observed for Models 1, 2, 4, and 5 during level, incline, and decline running conditions

Table E.2 presents the COD (R^2) observed for the Achilles tendon during the investigated running conditions and musculoskeletal models, where the respective COD values are calculated in terms of the *in-vivo* Achilles tendon force for Participant 2 and the respective running conditions.

Stellenbosch University https://scholar.sun.ac.za

Table E.2: Coefficient of determination (R^2) observed for the estimated Achilles tendon forces of Models 1, 2, 4, and 5 during level, incline, and decline running

	R^2		
Model	**Level**	**Incline**	**Decline**
Model 1	0.61	0.62	0.57
Model 2	0.62	0.64	0.56
Model 4	0.61	0.62	0.6
Model 5	0.62	0.64	0.56

* R^2 is calculated in terms of the *in-vivo* Achilles tendon loading profiles (Groeneveld, 2020) for the respective running trials ($R^2_{\textit{in-vivo}}$ = 1.0)

Stellenbosch University https://scholar.sun.ac.za

List of References

Adler, R.J. and Taylor, J.E. (2007). *Random fields and geometry*. Springer-Verslag, New York (NY).

Alegre, L.M., Hasler, M., Wenger, S., Nachauer, W. and Csapo, R. (2016). Does knee joint cooling change in vivo patellar tendon mechanical properties? *Eur J Appl Physiol*, vol. 116, no. 10, pp. 1921–1929.

Alexander, R.M. (1991). Energy saving mechanisms in walking and running. *Journal of Experimental Biology*, vol. 160, no. 1, pp. 55–69.

Anderson, F.C. and Pandy, M.G. (1999). A dynamic optimization solution for vertical jumping in three dimensions. *Computer Methods in Biomechanics and Biomedical Engineering*, vol. 2, no. 3, pp. 201–231.

Anderson, T. (1996). Biomechanics and running economy. *Sports medicine*, vol. 22, no. 2, pp. 76–89.

Apaydin, N., Bozkurt, M., Loukas, M., Vefali, H., S., T.R. and Esmer, A.F. (2009). Relationships of the sural nerve with the calcaneal tendon: an anatomical study with surgical and clinical implications. *Journal of Surgical and Radiologic Anatomy*, vol. 31, no. 10, pp. 775–780.

Arnold, E.M., Ward, S.R., Lieber, R.L. and Delp, S.L. (2010). A model of the lower limb for analysis of human movement. *Ann Biomed Eng*, vol. 38, no. 2, pp. 269–279.

Atkinson, J. (2018 March). *Computational Modelling Techniques to Determine Patellofemoral Joint Loads*. Master's thesis, Department of Mechanical and Mechatronic Engineering, University of Stellenbosch.

Au, C. and Dunne, J. (2012). Gait 2392 and 2354 models. OpenSim Documentation. Available at: `http://simtk-confluence.stanford.edu:8080/display/OpenSim/Gait+2392+and+2354+Models`

Baeyens, J.P., Goossens, M. and Serrien, B. (2019). Statistical parametric mapping of biomechanical one-dimensional data with bayesian inference. *International Biomechanics*, vol. 6, pp. 9–18.

Barclay, T. (2017). The patella ligament [Online]. Available at: `https://www.innerbody.com/image_skelfov/ligm02_new.html`, [2019, May 10].

Behrmann, G.P., Hidler, J. and Mirotznik, M.S. (2012). Fiber optic micro-sensor for the measurement of tendon forces. *Biomedical Engineering Online*, vol. 11, p. 77.

Bertec (2013). *Instrumented Treadmill User Manual, Version 2.0*. Bertec Corporation, Columbus, Ohio.

Bezodis, N.E., Salo, A.I. and Trewartha, G. (2013). Excessive fluctuations in knee joint moments during early stance in sprinting are caused by digital filtering procedures. *Gait & posture*, vol. 38, no. 4, pp. 653–657.

Bigoutte, J., Simon, J., Liu, K. and Docherty, C.L. (2016). Altered vertical ground reaction forces in participants with chronic ankle instability while running. *Journal of Athletic Training*, vol. 51, no. 9, pp. 682–687.

Stellenbosch University https://scholar.sun.ac.za

Bisseling, R.W. and Hof, A.L. (2006). Handling of impact forces in inverse dynamics. *Journal of Biomechanics*, vol. 39, no. 13, pp. 2438–2444.

Blettner, M., Hommel, G. and Schneider, A. (2010). Linear regression analysis: part 14 of a series on evaluation of scientific publications. *Deutsches Arzteblatt International*, vol. 107, no. 44, pp. 776–782.

Bramble, D.M. and Lieberman, D.E. (2004). Endurance running and the evolution of homo. *Nature*, vol. 432, pp. 345–352.

Britannica (2019 April). Tendon [Online]. Avaliable at: `https://www.britannica.com/science/tendon`, [2020, January 10].

Buchanan, T.S. (1995). Evidence that maximum muscle stress is not a constant: differences in specific tension in elbow flexors and extensors. *Med. Eng. Phys*, vol. 17, pp. 529–536.

Burdett, R.G. (1982). Forces predicted at the ankle during running. *Medicine and Science in Sports and Exercise*, vol. 14, pp. 308–316.

Caravaggi, P., Pataky, T.C., GÃ¼nther, M., Savage, R. and Crompton, R. (2010). Dynamics of longitudinal arch support in relation to walking speed: contribution of the plantar aponeurosis. *Journal of Anatomy*, vol. 217, pp. 254–261.

Coh, M. (2012). Overuse syndrome in running. *SportLogia*, vol. 8, no. 2, pp. 151–156.

Cohen, J. (1988). Statistical power analysis for the behavioral sciences. Abingdon.

D'Amico, E. (2002). Gait analysis systems. *Physical Medicine and Rehabilitation: State of Art Reviews*, vol. 16, no. 2, pp. 231–247.

Daniels, J.T. (1985). A physiologist's view on running economy. *Medicine and science in sports science*, vol. 17, no. 3, pp. 332–338.

de Leva, P. (1996). Adjustments to zatsiorsky-seluyanov's segment inertia parameters. *Journal of Biomechanics*, vol. 29, no. 9, pp. 1223–1230.

de Pina Filho, A.C. and Dultra, M. (2013). Modelling of the human ankle by means of a nonlinear oscillators system. IV International Symposium on Solid Mechanics, MecSol 2013. Porto Alegre, Brazil.

Del Buonu, A., Chan, O. and Maffulli, N. (2013). Achilles tendon: functional anatomy and novel emerging models of imaging classification. *International Orthopaedics*, vol. 37, no. 4, pp. 715–721.

Delp, S.L. (1990). *Surgery Simulation: A Computer Graphics System to Analyse and Design Musculoskeletal Reconstructions of the Lower Limb*. Ph.D. thesis, Standford University, Standford, CA.

Delp, S.L., Anderson, F.C., Arnold, A.S., Loan, P., Habib, A., John, C.T., Guendelman, E. and Thelen, D.G. (2007). Opensim: Open-source software to create and analyze dynamic simulations of movement. Available at: `https://simtk.org/api_docs/opensim/api_docs/index.html`.

Delp, S.L., Loan, J.P., Hoy, M.G., Zajac, F.E., Topp, E.L. and Rosen, J.M. (1999). An interactive graphics-based model of the lower extremity to study orthopaedic surgical procedures. *IEEE Transactions on Biomedical Engineering*, vol. 37, no. 8, pp. 757–767.

Stellenbosch University https://scholar.sun.ac.za

Doral, M.N., Alam, M., Bozkurt, M., Turhan, E., Atay, O.A., Donmez, G. and Maffulli, N. (2010). Functional anatomy of the achilles tendon. *Knee Surgery, Sports Traumatology, Arthroscopy*, vol. 18, no. 5, pp. 638–643.

Duarte, M. (2020). psd2: A python module for estimation of power spectral density characteristics using welch's method. `https://github.com/demotu/psd2`.

Dugan, S.A. and Bhat, K.P. (2005). Biomechanics and analysis of running gait. *Physical Medicine and Rehabilitation Clinics*, vol. 16, no. 3, pp. 603–621.

Esquenazi, A. (2002). Clinical application of joint kinetic analysis in gait. *Physical Medicine and Rehabilitation: State of Art Reviews*, vol. 16, no. 2, pp. 201–213.

Evans, A.C., Frackowiak, R.S.J., Friston, K.J., Mazziotta, J.C. and Worsley, K.J. (1994). Assessing the significance of focal activations using their spatial extent. *Human Brain Mapping*, vol. 1, pp. 210–220.

Faber, H., Van Soest, A.J. and Kistemaker, D.A. (2018). Inverse dynamics of mechanical multibody systems: An improved algorithm that ensures consistency between kinematics and external forces. *PloS ONE*, vol. 13, p. e0204575.

Farley, C.T. and Gonzalez, O. (1996). Leg stiffness and stride frequency in human running. *Journal of Biomechanics*, vol. 29, no. 2, pp. 181–186.

Feng, C., Fralick, D., Tu, X.M., B., W., Xu, M. and Zheng, J.Z. (2017). The differences and similarities between two-sample t-test and paired t-test. *Shanghai Arch Psychiatry*, vol. 29, no. 3, pp. 184–188.

French, T., Klein, B. and Lee, Y. (2018). *Patellofemoral Joint Stress during Uphill and Downhill Running in Healthy Runners*. Ph.D. thesis, Department of Physical Therapy, University of Nevada, Las Vegas, USA.

Friederich, J.A. and Brand, R.A. (1990). Muscle fiber architectuie in the human lower limb. *J. Biomech.*, vol. 23, pp. 91–95.

Galloy, A., Frish, K. and Schmitz, D. (2018). Asb 2018: Pipeline shared by dordt college and uw madison. OpenSim Workshop Presentation Notes.
Available at: `https://simtk-confluence.stanford.edu:8443/display/OpenSim/ASB+2018%3A+Pipeline+Shared+by+Dordt+College+and+UW+Madison`

Gottschall, J.S. and Kram, R. (2005). Ground reaction forces during downhill and uphill running. *Journal of Biomechanics*, vol. 38, pp. 445–452.

Groeneveld, L. (2020 March). *In-vivo measurement of Patella and Achilles tendon forces during treadmill running*. Master's thesis.

Grumbine, N.A. and Santoro, J.P. (1990). The tendo achillis as it relates to rearfoot position. a new classification for evaluation of calcaneal stance position. *Clinics in Podiatric Medicine and Surgery*, vol. 7, no. 2, pp. 203–216.

Hamner, S.R., Seth, A. and Delp, S.L. (2010). Muscle contributions to propulsion and support during running. *Journal of Biomechanics*, vol. 43, pp. 2709–2716.

Handsfield, G.G., Meyer, C.H., Hart, J.M. and Sbel, M.F. (2014). Relationships of 35 lower limb muscles to height and body mass quantified using mri. *Journal of Biomechanics*, vol. 47, pp. 631–638.

Stellenbosch University https://scholar.sun.ac.za

Healthwise (2018). Achilles tendon. Avaliable at: https://www.healthlinkbc.ca/health-topics/ug3002.

Heiderscheit, B.C., Chumanov, E.S. and Michalski, M.P. (2011). Effects of step rate manipulation on joint mechanics during running. *Med Sci Sports Exerc*, vol. 43, pp. 296–302.

Heinemeier, K.M. and Kjaer, M. (2011). In vivo investigation of tendon responses to mechanical loading. *J Musculoskelet Neuronal Interact*, vol. 11, no. 2, pp. 115–123.

Hicks, J.L., Uchida, T.K., Seth, A., Rajagopal, A. and Delp, S.L. (2015). Is my model good enough? best practices for verification and validation of musculoskeletal models and simulations of movement. *Journal of Biomechanical Engineering*, vol. 137, pp. 0209051–02090524.

Ho, K.Y., French, T., Klein, B. and Lee, Y. (2018). Patellofemoral joint stress during incline and decline running. *Physical Therapy in Sport*, vol. 34, pp. 136–140.

Holzbaur, K.R., Murray, W.M. and Delp, S.L. (2005). A model of the upper extremity for simulating musculoskeletal surgery and analyzing neuromuscular control. *Annals of Biomedical Engineering*, vol. 33, no. 6, pp. 829–840.

Islam, M.R. (2018). Knee joint : Anatomy, movement & muscle involvement [Online]. Available at: https://https://www.howtorelief.com/knee-joint-anatomy-muscle\-involvement/, [2019, May 10].

Kainz, H., Hoang, H., Stockton, C., Boyd, R.R., Lloyd, D.G. and Carty, C.P. (2017). Accuracy and reliability of marker based approaches to scale the pelvis, thigh and shank segments in musculoskeletal models. *Journal of Applied Biomechanics*, vol. 33, no. 5, pp. 354–360.

Kapandji, I.A. (1985). *Funktionelle Anatomie der Gelenke*. 2nd edn. Ferdinand Enke Verlag Stuttgart.

KenHub (2019). The patella tendon [Online]. Available at: https://www.kenhub.com/en/library/anatomy/patellar-tendon, [2019, May 10].

Kintec (2016*a*). The run center: Running gait cycle [Image]. Available at: https://www.kintec.net/blog/the-run-centre-4-point-run-analysis/, [2018, May 6].

Kintec (2016 March*b*). The run centre: 4-point run analysis [Online]. Available at: https://www.kintec.net/blog/the-run-centre-4-point-run-analysis/, [2019, May 7].

Lai, A.K.M., Arnold, A.S. and Wakeling, J.M. (2017). Why are antagonist muscles co-activated in my simulation? a musculoskeletal model for analysing human locomotor task. *Annals of Biomedical Engineering*, vol. 45, no. 12, pp. 2762–2774.

Lembeck, B., Mueller, O., Reize, P. and Wuelker, N. (2005). Pelvic tilt makes acetabular cup navigation inaccurate. *Acta orthopaedica*, vol. 76, no. 4, pp. 517–523.

Lenhart, R., Thelen, D. and Heiderscheit, B. (2014). Hip muscle loads during running at various step rates. *Journal of Orthopaedic & Sports Physical Therapy*, vol. 44, pp. 766–A4.

Lichtwark, G.A. and Wilson, A.M. (2006). Interactions between the human gastrocnemius muscle and the achilles tendon during incline, level and decline locomotion. *Journal of Experimental Biology*, vol. 209, no. 21, pp. 4379–4388.

Maganaris, C.N., Baltzopoulos, V., Ball, D. and Sargeant, A.J. (2001). In-vivo specific tension of human skeletal muscle. *J. Appl. Physiol.*, vol. 90, no. 3, pp. 865–872.

Stellenbosch University https://scholar.sun.ac.za

Malliaras, P., Cook, J., Purdam, C. and Rio, E. (2015). Patellar tendinopathy: clinical diagnosis, load management, and advice for challenging case presentations. *Journal of Orthopaedic & Sports Physical Therapy*, vol. 45, pp. 887–898.

Mann, R.A. and Hagy, J. (1980). Biomechanics of walking, running, and sprinting. *The American journal of sports medicine*, vol. 8, no. 5, pp. 345–350.

Mantoan, A., Pizzolato, C., Sartori, M., Sawacha, Z., Cobelli, C. and Reggiani, M. (2015). Motonms: A matlab toolbox to process motion data for neuromusculoskeletal modeling and simulation. *Source Code for Biology and Medicine*, vol. 10, no. 12.

Marieb, E.N. and Keller, S.M. (2018). *Essentials of human anatomy and physiology*. 12th edn. Pearson.

Mathworks.com (2019). What is inverse kinematics? [Online]. Available at: `https://www.mathworks.com/discovery/inverse-kinematics.html`, [2019, May 5].

Matijevich, E.S., Branscombe, L.M., Scott, L.R. and Zelik, K.E. (2019). Ground reaction force metrics are not strongly correlated with tibial bone load when running across speeds and slopes: Implications for science, sport and wearable tech. *PLOS ONE*, vol. 14, no. 1, pp. 5–13.

McMahon, T.A. (1990). Spring-like properties of muscles and reflexes in running: multiple muscle systems. *Journal of Biomechanics of Movement*, vol. 37, pp. 578–590.

Merletti, R. (2015). Standards for reporting emg data. These standards are endorsed by the International Society for Electrophysiology and Kinesiology (ISEK).
Available at: `https://isek.org/wp-content/uploads/2015/05/Standards-for-Reporting-EMG-Data.pdf`

Monte, L. (1976). A cinematographic analysis of overground and treadmill running by males and females. *Medicine and science in sports*, vol. 8, no. 2, pp. 84–87.

Moore, I.S. (2012). Mechanisms for improved running economy in beginner runners. *Medicine and Science in Sports and Exercise*, vol. 44, no. 9, pp. 1756–1763.

Moore, I.S. (2016). Is there an economical running technique? a review of modifiable biomechanical factors affecting running economy. *Sports Medicine*, vol. 46, pp. 793–807.

Moore, I.S., Jones, A. and Dixon, S. (2014). The pursuit of improved running performance: Can changes in cushioning and somatosensory feedback influence running economy and injury risk? *Footwear Science*, vol. 6, no. 1, pp. 1–11.

Moore, K.L., Agur, A.M.R. and Dalley, A.F. (2011). *Essential Clinical Anatomy*. 4th edn. Lippincott Williams & Wilkins, Baltimore.

Morris, J.M. (1977 Januray-February). Biomechanics of the foot and ankle. *Clinical Orthopaedics and Related Research*, , no. 122, pp. 10–17.

Muller, C., Dillon, E., Baynes, H., Cockcroft, J. and Moore, I. (2018 August). Patella and achilles tendon forces during treadmill running: Project rationale and objectives. Tech. Rep., Department of Mechanical and Mechatronic Engineering, University of Stellenbosch.

Munro, C.F., Miller, D.I. and Fuglevand, A.J. (1987). Ground reaction forces in running: A reexamination. *Journal of Biomechanics*, vol. 20, pp. 147–155.

Stellenbosch University https://scholar.sun.ac.za

Nelson, R.C., Dillman, C.J., Lagasse, P. and Bickett, P. (1972). Biomechanics of overground versus treadmill running. *Medicine and science in sports*, vol. 4, no. 4, p. 233.

Neves, K.A. (2014 March). *Achilles Tendon Changes in Downhill, Level, and Uphill Running*. Master's thesis.

Novacheck, T.F. (1998 August). The biomechanics of running. *Gait and Posture*, vol. 7, pp. 77–95.

Novo, C.D. (2011 January). Error modeling [Online]. Available at: `https://www.researchgate.net/publication/278667047_ERROR_MODELING`, [2020, January 10].

Noyes, F.R., Butler, D.L., Grood, E.S., Zernicke, R.F. and Hefzy, M.S. (1984). Biomechanical analysis of human ligament grafts used in knee-ligament. *Journal of Bone and Joint Surgery America*, vol. 66, pp. 344–352.

Oikawa, R., Tajima, G., Yan, J., Maruyama, M., Sugawara, A., Oikawa, S., Saigo, T., Takahashi, H. and Doita, M. (2018). Morphology of the patellar tendon and its insertion sites using three-dimensional computed tomography: A cadaveric study. *The Knee*, vol. 26, no. 2, pp. 302–309.

OpenSim (2017*a*). About opensim [Online]. Available at: `https://simtk-confluence.stanford.edu:8443/display/OpenSim/About+OpenSim`, [2019, May 2].

OpenSim (2017*b*). Getting started with inverse dynamics [Online]. Available at: `https://simtk-confluence.stanford.edu:8443/display/OpenSim/Getting+Started\+with+Inverse+Dynamics`, [2019, May 5].

OpenSim (2017*c*). How cmc works[Online]. Available at: `https://simtk-confluence.stanford.edu:8443/display/OpenSim/How+CMC\+Works`, [2019, May 6].

OpenSim (2017*d*). How inverse dynamics works [Online]. Available at: `https://simtk-confluence.stanford.edu:8443/display/OpenSim/How+Inverse\+Dynamics+Works`, [2019, May 5].

OpenSim (2017*e*). How inverse kinematics works [Online]. Available at: `https://simtk-confluence.stanford.edu:8443/display/OpenSim/How+Inverse\+Kinematics+Works`, [2019, May 5].

OpenSim (2017*f*). How rra works[Online]. Available at: `https://simtk-confluence.stanford.edu:8443/display/OpenSim/How+RRA\+Works`, [2019, May 6].

OpenSim (2017*g*). Overview of the opensim workflow[Online]. Available at: `https://simtk-confluence.stanford.edu:8443/display/OpenSim/Overview+of+the\+OpenSim+Workflow`, [2019, May 3].

OpenStax (2013 March). Anatomy and physiology [Online]. Available at: `https://opentextbc.ca/anatomyandphysiology/chapter/6-1-the-functions-of-the-skeletal-system/`, [2020, January 10].

Palmitier, R.A., An, K.N., Scott, S.G. and Chao, E.Y. (1991). Kinetic chain exercise in knee rehabilitation. *Journal of Sports Medicine*, vol. 11, no. 6, pp. 402–413.

Pataky, T.C. (2010). Generalized n-dimensional biomechanical field analysis using statistical parametric mapping. *Journal of Biomechanics*, vol. 43, pp. 1976–1982.

Stellenbosch University https://scholar.sun.ac.za

Pataky, T.C. (2012). One-dimensional statistical parametric mapping in python. *Computer Methods in Biomechanical and Biomedical Engineering*, vol. 15, pp. 295–301.

Pataky, T.C. (2019). Available at: `https://spm1d.org/Documentation.html` [2020, July 28]. Spm1d Documentation.

Phillips, M. (2013 April). Introduction to running biomechanics [Online]. Available at: `https://runnersconnect.net/running-biomechanics/`, [2019, May 7].

Pizzolato, C., Lloyd, D.G., Sartori, M., Ceseracciu, E., Besier, T.F., Fregly, B.J. and Reggiani, M. (2015). Ceinms: A toolbox to investigate the influence of different neural control solutions on the prediction of muscle excitation and joint moments during dynamic motor tasks. *Journal of Biomechanics*, vol. 48, no. 14, pp. 3929–3936.

Pope, D. (2018). Anatomy, causes and treatment of jumpers knee (patella tendinopathy) [Online]. Available at: `https://fitnesspainfree.com/anatomy-causes-treatment-jumpers\-knee-patellar-tendinopathy-part-1/`, [2019, May 10].

Rajagopal, A., Dembia, C.L., DeMers, M.S., Delp, D.D., Hicks, J.L. and Delp, S.L. (2016). Full body musculoskeletal model for muscledriven simulation of human gait. *IEEE Transactions on Biomedical Engineering*, vol. 63, no. 10, pp. 2068–2079.

Riley, P.O., Paolini, G., Della Croce, U., Paylo, K.W. and Kerrigan, D.C. (2007). A kinematic and kinetic comparison of overground and treadmill walking in healthy subjects. *Gait & posture*, vol. 26, no. 1, pp. 17–24.

Roberts, T.J. and Belliveau, R.A. (2005). Sources of mechanical power for uphill running in humans. *Sports Medicine*, vol. 208, pp. 1963–1970.

Roberts, T.J., Marsh, R.L., Weyand, P.G. and Taylor, C.R. (1997). Muscular force in running turkeys: the economy of minimizing work. *Science Magazine*, vol. 275, pp. 1113–1115.

Robi, K., Jakob, N., Matevz, K. and Matjaz, V. (2013). The physiology of sports injuries and repair processes. In: Hamlin, M., Draper, N. and Kathiravel, Y. (eds.), *Current Issues in Sports and Exercise Medicine*, chap. 2. IntechOpen, Rijeka.
Available at: `https://doi.org/10.5772/54234`

Roewer, B.D., Ford, K.R., Myer, G.D. and Hewett, T.E. (2014). The 'impact' of force filtering cut-off frequency on the peak knee abduction moment during landing: artefact or 'artifiction'? *Br J Sports Med*, vol. 48, no. 6, pp. 464–468.

Rose, W.C. (2019). Electromyogram (emg) analysis. Notes for EMG Signal Processing. Presented as part of a Mathematics and Signal Processing for Biomechanics course.
Available at: `https://www1.udel.edu/biology/rosewc/kaap686/notes/EMG%20analysis.pdf`

Samaan, M.A., Weinhandl, J.T., Bawab, S.Y. and Ringled, S.I. (2016). Determining residual reduction algorithm kinematic tracking weights for a sidestep cut via numerical optimization. *Computer Methods in Biomechanics and Biomedical Engineering*, vol. 19, no. 16, pp. 1721–1729.

Saunders, P.U., Pyne, D.B., Telford, R.D. and Hawley, J.A. (2004). Factors affecting running economy in trained distance runners. *Journal Sports Medicine*, vol. 34, no. 7, pp. 465–485.

Schmitz, A. and Piovesan, D. (2016). Development of an open-source, discrete element knee model. *IEEE Transactions on Biomedical Engineering*, vol. 63, no. 10, pp. 2056–2067.

Stellenbosch University https://scholar.sun.ac.za

Scott, S.H. and Winter, D.A. (1990). Internal forces of chronic running injury sites. *Medicine and science in sports and exercise*, vol. 22, no. 3, pp. 357–369.

Seth, A., Sherman, M., Eastman, P. and Delp, S. (2010). Minimal formulation of joint motion for biomechanisms. *Nonlinear Dynamics*, vol. 62, no. 1, pp. 291–303.

Seth, A., Sherman, M., Reinbolt, J.A. and Delp, S.L. (2011). Opensim: a musculoskeletal modeling and simulation framework for *in-silico* investigations and exchange. *Procedia IUTAM*, vol. 2, pp. 212–232.

Shaerf, D.A., Pastides, P.S., Sarraf, K.M. and Willis-Owen, C.A. (2014). Anterior cruciate ligament reconstruction best practice: A review of graft choice. *World Journal of Orthopedics*, vol. 5, no. 1, pp. 23–29.

Shahib, S. and Zehra, U. (2020). Patella [Online]. Available at: `https://www.kenhub.com/en/library/anatomy/patella`, [2020, August 5].

Sheehan, F. and Drace, J.E. (2000). Human patellar tendon strain. a noninvasive, in vivo study. *Clinical Orthopaedics and Related Research*, , no. 370, pp. 201–207.

Sheila, A., Dugan, M.D., Krishna, P. and Bhat, M.D. (2005). Biomechanics and analysis of running gait. *Physical Medicine and Rehabilitation Clinics of North America*, vol. 16, no. 3, pp. 603–621.

Simtk-confluence.stanford.edu (2020). Opensim documentation [online]. Available at: `https://simtk-confluence.stanford.edu/display/OpenSim/Documentation` [2020, August 15].

Sinclair, J., Taylor, P.J. and Hobbs, S.J. (2013). Digital filtering of three-dimensional lower extremity kinematics: an assessment. *Journal of Human Kinematics*, vol. 39, pp. 5–13.

Svensson, R.B., Hanssen, P., Hassenkam, T., Haraldsson, B.T., Aagaad, P., Kovanen, V., Krogsgaard, M., Kjaer, M. and Magnusson, S.P. (2012). Mechanical properties of human patellar tendon at the hierarchical levels of tendon and fibril. *J Appl Physiol*, vol. 112, pp. 419–426.

Taunton, J.E., Ryan, M.B. and Clement, D.B. (2002). A retrospective case-control analysis of 2002 running injuries. *Br J Sports Med*, vol. 36, pp. 95–101.

Telhan, G., Franz, J.R., Dicharry, J., Wilder, R.P., Riley, P.O. and Kerrigan, D.C. (2010). Lower limb joint kinetics during moderately sloped running. *Journal of Athletic Training*, vol. 45, no. 1, pp. 16–21.

Thabane, L., Mbuagbaw, L., Zhang, S., Samaan, Z., Marcucci, M., Ye, C., Thabane, M., Giangregorio, L., Dennis, B., Kosa, D., Debono, V.B., Dillenburg, R., Fruci, V., Bawor, M., Lee, J., Wells, G. and Goldsmith, C.H. (2013). A tutorial on sensitivity analyses in clinical trials: the what, why, when and how. *BMC Med Res Methodol*, vol. 13.

Thelen, D.G. (2003). Adjustment of muscle mechanics model parameters to simulate dynamic contractions in older adults. *ASME Journal of Biomechanical Engineering*, vol. 125, no. 1, pp. 70–77.

Thelen, D.G. and Anderson, F.C. (2006). Using computed muscle control to generate forward dynamic simulations of human walking from experimental data. *Journal of Biomechanics*, vol. 39, no. 6, pp. 1107–1115.

Trinler, U.K. (2016). *Muscle force estimation in clinical gait analysis*. Ph.D. thesis, University of Salford, Salford, UK.

Stellenbosch University https://scholar.sun.ac.za

van Eijden, T.M.G.J., Kouwenhoven, E., Verburg, J. and Weijs, W.A. (1986). A mathematical model of the patellofemoral joint. *Journal of Biomechanics*, vol. 19, no. 3, pp. 219–229.

Vaughan, C.L. (1984). Biomechanics of running gait. *Critical reviews in biomedical engineering*, vol. 12, no. 1, pp. 1–48.

Vernillo, G., Giandolini, M. and Edwards, W.B. (2016). Biomechanics and physiology of uphill and downhill running. *Sports Medicine*, pp. 1–15.

Vicon (2019). Full body modelling with plug-in gait [Online]. Avaliable at: `https://docs.vicon.com/display/Nexus26/Full+body+modeling+with+Plug-in+Gait`, [2020, January 12].

Villa-Forte, A. (2019 October). Introduction to the human body [Online]. Available at: `https://www.msdmanuals.com/home/fundamentals/the-human-body/introduction-to-the-human-body`, [2020, January 10].

Walker, P.S., Rovic, J.S. and Robertson, D.D. (1988). The effects of knee brace hinge design and placement on joint mechanics. *Journal Biomechanics*, vol. 21, no. 11, pp. 965–974.

Wang, J.H., Guo, Q. and Li, B. (2012). Tendon biomechanics and mechanobiology - a minireview of basic concepts and recent advancements. *Journal of hand therapy*, vol. 25, no. 2, pp. 133–141.

Ward, S.R., Carolyn, M., Smallwood, L.H. and Lieber, R.L. (2009). Are current measurements of lower extremity muscle architecture accurate? *Clin Orthop Relat Res*, vol. 467, no. 4, pp. 1074–1082.

Whittle, M.W., Levine, D. and Pharo, E.C. (2000). Sagittal plane motion of the pelvis and lumbar spine during level, uphill and downhill walking and running. *Gait and Posture*, vol. 11, p. 162.

Wickiewicz, T.L., Roy, R.R., Powell, P.L., and Edgerton, V.R. (1983). Muscle architectuie of the human lower limb. *Clin. Orthop. Rei. Res.*, vol. 179, pp. 275–283.

Wilke, H.J. and Galbusera, F. (2018). Musculoskeletal modelling. In: Bassani, T. and Galbusera, F. (eds.), *Biomechanics of the Spine: Basic Concepts, Spinal Disorders and Treatments*, 1st edn, chap. 15. Academic Press, London, United Kingdom.

Winter, D.A. (2009). *Biomechanics and motor control of human movement*. 4th edn. John Wiley & Sons, Inc., Waterloo, Ontario, Canada.

Yamaguchi, G.T. and Zajac, F.E. (1989). A planar model of the knee joint to characterize the knee extensor mechanism. *Journal of Biomechanics*, vol. 21, pp. 1–10.

Yu, T.F. and Wilson, A.J. (2014). A passive movement method for parameter estimation of a musculo-skeletal arm model incorporating a modified hill muscle model. *Computer Methods and Programs in Biomedicine*, vol. 114, pp. e46–e59.